Imperial College London

Optimal control of topological quantum systems

Said Omar Raii

Department of Physics

Imperial College London

Thesis submitted in partial fulfilment of the requirements

for the degree of Doctor of Philosophy in Physics

January 2023

Supervisors: Prof. Daniel Burgarth, Macquarie University

Prof. Florian Mintert, Imperial College London

I declare that, except where otherwise referenced, all of the work presented in this thesis is my own, and is based on research carried out under the supervision of Daniel Burgarth and Florian Mintert, while at Imperial College London.

Said Omar Raii

January 2023

Acknowledgements

I would like to begin by thanking my supervisors Florian Mintert and Daniel Burgarth. Their guidance and support throughout the last few years has been invaluable and I cannot emphasise enough how much I have appreciated their time and patience. There have been many challenges to deal with over the last few years, most notably the pandemic, and I am certain I would not have overcome these without their expertise, their kindness and their generosity.

I am also grateful to other members of the Imperial community from whom I have learnt much and who deserve thanks. Firstly I would like to thank Myungshik Kim and Mark Oxborrow for the support they provided through the Quantum Systems Engineering hub. In addition I'd like to thank my fellow QSE students in Cohort 2 for providing great friendship and camaraderie.

Other students and researchers in Florian Mintert's group also provided friendly and fruitful discussions over the years and they include Jake Lishman, Rick Muckherjee, Frederic Sauvage, Honzheng Zhao, Selwyn Simsek, Sean Greenaway, and many others. I would also like to thank Ryan Barnett and Kiran Khosla for their helpful advice on the topics in the thesis.

Particular thanks go to Mahdi Sameti for useful discussions and guidance with work on the toric code and Alex Pitchford for his great help and support with numerics and optimisation. I also want to acknowledge the helpful advice given by Benjamin Brown during my visit to Sydney.

I'd like to thank my family, including my sister Gazal, my brother Sid, my grandparents and in particular my parents. Their support has been much appreciated and I will always be grateful for how much they have loved and encouraged me throughout the years.

Finally, I would like to thank the most important person in my life Katie Kruger. Without her love, selflessness and generosity I certainly would not have been able to complete this project. I could not be more grateful to have her in my life.

Funding

I am grateful for the funding provided for this PhD by UKRI EPSRC Grant No. EP/P510257/1 via the Imperial College London Quantum Systems Engineering Skills and Training Hub.

Abstract

Topological quantum computation provides an architecture for encoding quantum information in such a way as to be theoretically robust to local noise. Logical qubits are encoded in topological degrees of freedom typically in spin-lattice models. Excitations in the spin-lattice models manifest as anyons, generalisations of bosons and fermions that exist in two dimensions. Proposals for experimental realisation of these topological systems have previously relied on perfect anyon creation in a time-independent manner or in the case of time-dependent proposals have primarily relied on adiabatic, therefore slow, dynamics. The aim of this thesis is to use quantum control to create anyons and encode logical qubits in topological systems without the requirement for adiabaticity and long timescales.

First, we demonstrate the creation of abelian anyons using time-dependent controls in the toric code model, a system that is useful as a quantum memory. We show that this may be done within arbitrarily short timescales at the expense of larger magnitude control pulses. Additionally, we investigate the robustness of our protocol in the face of theoretical errors in anyon creation.

Secondly, we investigate the creation of non-abelian anyons in the Kitaev honeycomb model. By fermionising a time-dependent version of the model we demonstrate how optimal control theory can allow for anyon creation in faster-than-adiabatic time. Moreover, we show that the particular method we develop to achieve this scales only linearly in the number of spins in the lattice.

Thirdly, we investigate defect creation in the surface code, a generalisation of the toric code that does not require periodic boundary conditions. Optimal quantum control is used to show how defects may be created faster than with the typical adiabatic procedures. Additionally, a method using mapping of dynamical Lie algebras is used to demonstrate that optimal control techniques may be extended to operations whose dynamics require solving in a large Hilbert space.

Contents

List of Figures

List of Tables

Chapter 1

Background

1.1 Introduction

In recent decades we have seen great progress in the understanding of the theoretical benefits provided by the storage of quantum information, as well of the possible implementation of fault-tolerant quantum computation. Ever since it was shown that there exist quantum algorithms that perform with an exponential speed-up when confronting problems that are not efficiently solvable in the classical regime, well-known examples of which include integer factorisation [1] and database searching [2], the pursuit of a quantum computer with fully programmable individual qubits has been broad with many different candidates for viable qubits being investigated. Moreover, while these algorithms require qubits to be stored temporarily, the long-term storage of quantum states is a useful part of protocols such as quantum key distribution and state teleportation [3, 4].

The candidates for the physical realisation of logical qubits include photons, trapped ions, optical lattices, quantum dots [5, 6, 7, 8] amongst others [9, 10, 11]. Though many of these qubits have been demonstrated as workable, there are nevertheless major obstacles for moving towards large-scale quantum computers due to the problems of decoherence and error corrections. Decoherence leads to loss of quantum superposition states, one of the key characteristics of quantum states that are exploited by many quantum algorithms. In addition, though fault-tolerant quantum computation is possible if a reliable enough

error-correction protocol is in place [12], most valid error-correcting protocols rely on the probability of error occurrence being small; typically on the scale of 10^{-4} to 10^{-6} [13].

It is in order to avoid these limitations right down at the hardware level that topological quantum systems have been a favoured proposal for the implementation of quantum computation [4, 12, 13]. In a topological quantum computer, the logical qubits are encoded in global topological degrees of freedom meaning that in principle they should be robust in the face of local noise [14]. The basic building blocks of topological quantum computation are anyons, generalisations of bosons and fermions which arise in two-dimensional systems. Our goal in this thesis is to use quantum control, a field that is comprised of numerous theoretical methods designed to realise desired quantum dynamics [15, 16, 17, 18, 19], to implement creation and manipulation of anyons and anyon-like entities. We start with a brief description of anyons and their applicability to quantum computation, followed by an overview of the field of quantum control.

1.2 Anyons and topological quantum computation

While in three spatial dimensions all particles are known to be bosonic or fermionic, such that particle exchange leads to a gain of $+1$ and -1 phase respectively to the physical system's wave function, in two dimensions more exotic behaviour is permissible [20, 21, 22]. One can consider particle exchange from a purely topological perspective. In three spatial dimensions, two particles being exchanged twice is topologically equivalent to one particle winding completely around another [23]. In three dimensions any winding path can be deformed continuously - i.e. is topologically equivalent - to the path of no movement at all. This shows that no nontrivial statistics are present and only a phase factor of 1 or -1 is possible after particle exchange.

The two-dimensional case demonstrates more exotic behaviour however. Here not only is the notion of a clockwise and anticlockwise winding well-defined, but the winding of one particle around another is no longer topologically equivalent to the particles not moving at all, as it is impossible to deform one path continuously into the other without

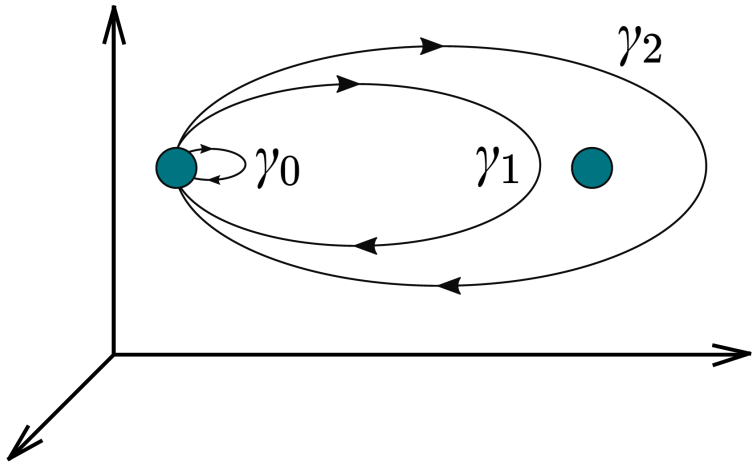

Figure 1.1: Winding path of identical particles around another. It is clear that while paths γ_0, γ_1 and γ_2 are equivalent topologically in three dimensions, this is not the case when restricted to only two dimensions.

an intersection. This is illustrated in Fig. 1.1.

The exchange of two particles leads to the wave function gaining an extra phase factor $e^{i\theta}$. When looking at a more general system of N particles, phase factors are introduced when n particles are exchanged in a certain direction. When this direction is positive a factor of $e^{in\theta}$ is gained whereas in the anticlockwise direction it is a factor of $e^{-in\theta}$. This value of θ can be understood in a clear way when one investigates the Aharonov-Bohm effect [24] which shows how a particle in a solenoidal magnetic field can gain a phase factor in the wave function independently of the path that it takes, therefore in a topological manner. The phase that is gained through this effect is known as a Berry phase [25].

The only transformation that takes place in the case of such abelian anyons is gaining of a phase. Another variety of anyonic quasiparticles, known as non-abelian anyons, are particularly useful for quantum computation. Here rather than a phase being gained, the wave function is acted on by a non-trivial unitary gate.

In the case of non-abelian anyons, we can consider their paths to be worldlines that start and finish at certain times. Particle exchanges can then be thought of as braids in those lines and so we can immediately see how the non-abelian property arises [23]. As an example, with three anyons, the braiding of the the first two followed by the latter two is not homotopically equivalent to carrying those operations out in the reverse order

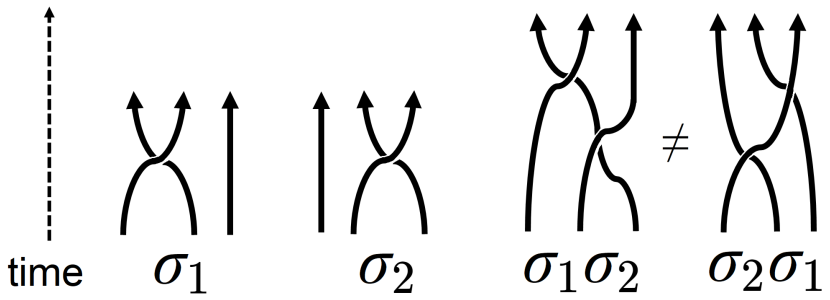

Figure 1.2: Schematic of particle exchange as braiding of worldlines. We can see that the operations σ_1, which exchanges the first two particles, and σ_2, which exchanges the latter two, do not commute with each other.

(see Fig. 1.2). It is these braiding operations that allow unitary gates to be performed on anyons and therefore computation to be possible. A degenerate ground space in a system with a gapped Hamiltonian therefore is a *sine qua non* of using non-abelian anyons for quantum computation as one would require no change in the energy of the system after particle braiding [26].

In addition to braiding, it is also useful to consider systems with anyons in terms of the number of particles present, in such a way that allows us to consider two anyons together as another anyon. This is known as *fusion* and for a given system there will be a set of fusion rules that govern such behaviour. The general formulation of fusion rules is given by

$$a \times b = \sum_c N_{ab}^c c \tag{1.1}$$

where N_{ab}^c is an integer that is generally 0 or 1 and a, b and c are the possible anyons in a system [14]. A simple example of a fusion rule would be $a \times b = 1 + c$ meaning that the fusion of anyons a and b results in either the trivial particle 1 (no anyon) or the anyon c. If we have that $\alpha \times \beta = 1$ then this means that α and β are antiparticles that annihilate.

There exist numerous anyonic models with different fusion rules such as the Ising model [27] as well as the Fibonnaci anyon model [28]. While Fibonnaci anyons allow for universal gate implementation, Ising anyons have been found to be more experimentally accessible as there have been experimental proposals for their realisation as Majorana zero modes [14, 29, 30, 31]. Moreover, it is possible in certain systems to integrate the topological

robustness offered by Ising anyons with non-topological mechanisms in order to achieve universality, therefore making the experimental realisation of such anyons desirable [32].

Implementing quantum computation with non-abelian anyons generally involves creating anyons, braiding them and fusing them in order to realise state initialisation, gate implementation and measurement respectively [26, 33].

1.3 Quantum control theory

It is well known that the dynamics of a closed quantum system, that is, a system where energy is not considered to dissipate into an environment, are characterised by unitary dynamics which arise out of the Schrödinger equation

$$i\dot{U}(t) = H(t)U(t) \tag{1.2}$$

where H is the, possibly time-dependent, Hamiltonian of the system and $U(t)$ is the time-evolution operator such that a general time-evolving state is $|\psi(t)\rangle = U(t)\,|\psi(0)\rangle$ [34]. Here, as in the rest of this work, natural units are used such that $\hbar = 1$.

The field of quantum control theory is principally focused on working to achieve certain desired dynamics within the framework of a physical system whose natural dynamics arise out of a defining Hamiltonian [15, 18]. Typically this system's internal Hamiltonian is considered the *drift* H_d, while controllable interactions are considered *control* Hamiltonians $H_{c,j}$ and these latter terms are coupled with time-dependent control functions $f_j(t)$ which determine differing dynamics depending on how they are designed. Thus a typically considered time-dependent Hamiltonian is

$$H(t) = H_d + \sum_j f_j(t) H_{c,j}. \tag{1.3}$$

Such control functions $f_j(t)$ are often known as *control pulses* or simply the *controls*. At times, particularly when intended for implementation of adiabatic dynamics, the control function is often a linear function known as a *ramp*.

In short, the aims of quantum control are: to assess the dynamics of a quantum system and to engineer these dynamics in such a way as to achieve a desired goal, the simplest of which is to transform one state into another non-identical state and the most challenging of which is to implement exactly the required unitary dynamics [15]. Optimal control seeks to realise the desired dynamics in such a way as to optimise a certain figure of merit, typically the fidelity for state transfer

$$\mathcal{F} := |\langle\psi_{\text{target}}|\psi\rangle|^2 \tag{1.4}$$

or, for the case of full unitary dynamics, the gate fidelity

$$\mathcal{F} = \frac{1}{d}\left|\text{Tr}\left(U_{\text{target}}^{\dagger}U\right)\right|. \tag{1.5}$$

Among the many known techniques of quantum control, examples that we utilise in our work include the well-tested gradient ascent pulse engineering method, or GRAPE algorithm [35, 36], more information on which is presented in Appendix A, and determining the space of all possible implementable unitary dynamics of a given Hamiltonian system using dynamical Lie algebras [15, 37, 38].

1.4 Scope of the thesis

Thus far in the literature, the investigation of topological quantum systems in the time-dependent regime has primarily been limited to adiabatic protocols. In our work we hope to use the methods of quantum control to implement protocols in topological quantum systems and see if our methods can provide certain benefits to anyon creation and similar operations, such as improving on the long timescales required by adiabaticity.

Quantum control has a proven track record of successfully speeding up adiabatic evolution in a wide range of scenarios [31, 39, 40, 41, 42] suggesting its potential suitability for creating anyons in topological systems. A common challenge for implementation of quantum control techniques is that they are often complex and resource-intensive, which

can limit their scalability.

We seek to use techniques that allow not only for an improvement on adiabatic timescales, but also robustness in the face of errors that inevitably become possible when time-dependence is introduced into a system's Hamiltonian. Additionally, there is an aim to ensure scalability of quantum control methods as, in topological systems, we routinely aim to control the dynamics of a system comprising of many-body interactions between qubits in a lattice.

Our principal goal is to successfully overcome what seems initially to be an inherent paradox at the heart of using quantum control for encoding and manipulating quantum information in topological systems. This is that if the encoding is robust to errors, how challenging must it be to enforce desired transformations? Conversely, if it possible to enforce desired transformations through engineering particular dynamics, how robustly encoded is the logical information?

The work of this thesis is divided into three main sections, each concerned with a different spin-lattice system which is capable of exhibiting non-trivial topological order. The second chapter looks at the toric code, a lattice system consisting of four-body interactions whose four-fold degenerate ground state allows for the encoding of logical qubits and can be used as a quantum memory. In this system abelian anyons can be made manifest as excitations in the Hamiltonian and we present a method of creating and annihilating anyons in finite time using control functions and discuss the method's advantages and limitations. We then proceed to reliably test how robust the encoded logical information would be, looking at various potential error models.

In the third chapter we are concerned with creating non-abelian anyons in the Kitaev honeycomb model [43], a lattice system comprised primarily of two-body interactions. We seek to extend the well-known fermionisation of the model to the time-dependent case and use this method to allow for anyon creation in faster than adiabatic times. The scalability of this method for large lattices is also discussed in detail.

In the fourth chapter we look at a generalisation of the toric code known as the surface code, a system which no longer relies on periodic boundary conditions and in which logical

gates can be performed on encoded quantum information. Anyon-like defects in the model which have previously been created and manipulated using adiabatic protocols are created using quantum control and we present a utilisation of dynamical Lie algebras to allow for the implementation of such techniques on a large number of qubits within a lattice. This newly developed method is generalisable to certain other types of control problems where it would be unfeasible to solve the full system dynamics without great computational resources.

We conclude with a summary of our results as well as a reflection on their significance for experimental implementation of topological qubits. We call attention to certain proposals that could take advantage of the methods presented in this thesis.

The work in Chapter 3 is primarily based on, and uses assets and text from, the following published article:

Omar Raii, Florian Mintert, and Daniel Burgarth 'Scalable quantum control and non-Abelian anyon creation in the Kitaev honeycomb model' *Physical Review A*, 106(6):062401, 12 (2022) [44]

Chapter 2

Creating abelian anyons in the toric code

Various examples of topological models have been put forward that display both abelian and non-abelian anyonic behaviour [43, 45] and the Kitaev toric code is a tremendously elegant example of a model wherein abelian anyons are made manifest and which allows for the encoding of 2^g logical qubits, depending on the genus g of the torus in question [45].

Anyon creation in topological systems such as these is generally assumed to be an idealised procedure [12, 23, 43] in the sense that anyons which are created, either as errors or otherwise, are done so in the infinitely quick regime. In this chapter, we use quantum control methods to steer toric code dynamics in such a way that desired anyon creation/annihilation is achieved in a finite, time-dependent and thus more experimentally realistic fashion. Given the nature of topological systems, this is not necessarily a straightforward endeavour; it cannot be taken for granted that many of the attractive topological properties of a system that exist for certain configurations of the Hamiltonian will remain when time-dependent changes are taken into account. Ground state degeneracy for instance, a determining property of topologically protected systems, is typically lifted when Hamiltonians are varied in finite systems [46], as the toric code lattices we investigate will be. The key question is if a topological state is robust against local errors,

how can we create anyons and go further in creating anyon-strings and performing logical gates in a time-dependent manner without causing global errors? While local errors are not supposed to affect the overall stability of logical qubits in topological systems, the use of quantum control in anyon creation means there is time for errors to spread. We seek to investigate the effects of local errors spreading in the toric code and the possibility of these leading to logical errors.

Thus far in the literature, the effect of small perturbations to the toric code Hamiltonian is well-known in terms of its effects on logical qubit stability [43, 47]. In addition, the creation of anyons in the toric code due to thermalisation has been analysed [48, 49] and the effects of unwanted anyons, with various modifications of the toric code suggested as systems that can for example increase quantum memory lifetime, have been studied in depth [47, 50]. However, though architecture for experimental realisation of the toric code has been proposed [51], anyon *creation* (or, analogously, annihilation) in a finite time setting has yet to be closely looked at, still less while in the presence of errors that are intrinsic to the Hamiltonian, which will be necessary for experimental implementations of this quantum memory.

In this chapter we begin by briefly reviewing the toric code, also known as the double quantum model, in Section 1. We proceed in Section 2 to present a mechanism for anyon creation in a finite time manner using pulses of arbitrarily bounded magnitude and in Section 3 we investigate this mechanism's resilience to errors. We discuss how to create anyons in this system in a time-dependent way and see how robust the anyonic states are in the presence of errors. Section 4 briefly discusses the possibility of generalising to multiple anyon creation and Section 5 presents results about the resilience of time-dependent anyon creation in the presence of intrinsic Hamiltonian errors, which are then compared with numerical results in Section 6. The final two sections discuss how intrinsic errors in the model affect correctability of unwanted anyonic eigenstates.

2.1 Description of the toric code

The toric code is comprised out of spin-1/2 particles on the edges of a quadrilateral lattice with periodic boundary conditions. Each lattice is defined by $m \times n$ plaquettes, and the number of plaquettes is equivalent to the number of vertices, with mn of each. The number of spins that comprise this lattice N is equal to the sum of the total number of plaquettes and vertices, and thus $N = 2mn$.

2.1.1 Hamiltonian and ground states

The Hamiltonian is constructed using four-body interacting operators acting on spins residing either on a given vertex or plaquette. Vertex operators acting on a vertex v are defined with Pauli X interactions as $A_v = X_{v_1} X_{v_2} X_{v_3} X_{v_4}$ while plaquette operators on a plaquette p are defined as $B_p = Z_{p_1} Z_{p_2} Z_{p_3} Z_{p_4}$ using Pauli Z interactions.

The Hamiltonian of the toric code system is then

$$H_{\mathrm{TC}} = -J_A \sum_v A_v - J_B \sum_p B_p. \tag{2.1}$$

where the J_A and J_B correspond to interaction strengths and and energy gap which will be taken to be unity in the chosen units. As it is comprised of the sum of commuting operators, it is straightforwardly diagonalisable. Where plaquette and vertex operators overlap they do so on exactly two spins and, as a result of the double anticommutation, they overall commute. As the Pauli matrices square to the identity the eigenvalues of each operator in the summand are ± 1, hence the ground state energy of the toric code E_g is the negative of the total number of vertices and plaquettes and thus $E_g = -N$.

The state, defined up to normalisation as

$$|g_1\rangle = \prod_v (\mathbf{1} + A_v) \, |0\rangle^{\otimes N}, \tag{2.2}$$

where $\mathbf{1}$ is the identity, is a ground state as it is stabilised by every vertex operator, which is to say that $A_v |g_1\rangle = |g_1\rangle$ for all vertices v. This is due to the property $A_v^2 = \mathbf{1}$.

Moreover, it is also stabilised by every plaquette operator, so that $B_p |g_1\rangle = |g_1\rangle$ for all plaquettes p. This is due to the fact that each B_p commutes with every A_v, as well as the fact that

$$B_p |0\rangle^{\otimes N} = \left(\prod_j Z_j \right) |0\rangle^{\otimes N} = |0\rangle^{\otimes N} . \tag{2.3}$$

2.1.2 Anyons in the toric code

Anyons emerge in the code as excitations above the ground state. For example, if a Pauli X were to act on a certain spin on the lattice, the new state would correspond to another energy eigenstate but with sign-flipped eigenvalues for the overlapping plaquette operators. The same applies for Z operations and vertex operators. It is exactly these excitations which are anyons either on plaquettes (m-anyons) or on vertices (e-anyons) as shown in Fig. 2.1. The energy penalty for excitation and anyon pair creation is 4 in the units of the interaction factor J.

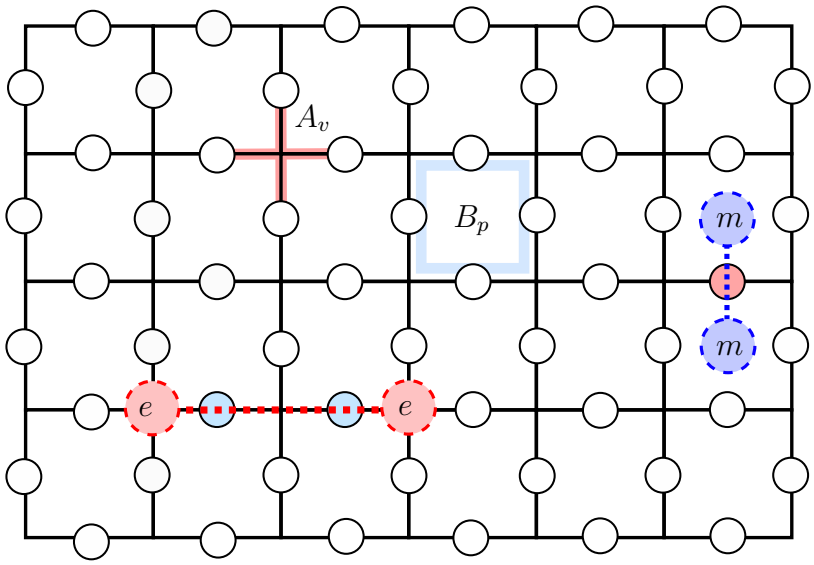

Figure 2.1: A toric code lattice showing an example of a vertex operator A_v and a plaquette operator B_p. An m-anyon pair (bottom right) is created by a Z operation on a spin (light red). An extended string of a pair of e-anyons (bottom left) are created by X rotations acting on two adjacent spins. Periodic boundary conditions mean that the top edges of the lattice are identical to the bottom edges while the leftmost edges are identical to the rightmost edges.

These anyons can be created and annihilated using the same process and anyon strings

may be extended by repeating the appropriate Pauli operation on successive adjacent spins. As Pauli operators square to the identity this leaves two anyons at the end of a string. Loops may be created by anyon strings and by extension, anyons may also be wound around one another. The geometry of the anyon strings is not directly measurable and therefore only the positions of the anyons are physically meaningful. When anyons of the same type overlap on the same local vertex or plaquette they annihilate and so the fusion rule describing this

$$e \times e = 1 \tag{2.4}$$

$$m \times m = 1 \tag{2.5}$$

shows that the e and m-type anyons are their own antiparticles. While the winding of two identical anyons of the same type around one another leads to no extra phase factor being gained by a state's wave function, thus making both anyon describes bosonic in terms of their statistics, fusing one of each type of anyon

$$e \times m = \varepsilon \tag{2.6}$$

gives a new type of anyon which is fermionic in terms of exchange statistics. From these three fusion rules all other possible fusion rules may be obtained for the three types of abelian anyons.

The topology of the anyon strings is crucial in distinguishing between states that are not locally distinguishable. If an m-anyon pair is created, after initialising in the ground state (2.2), and is extended until the pair of anyons overlap and annihilate on a string that forms a closed loop on the torus, another eigenstate is reached that also has vacuum anyon charge and is orthogonal to the ground state (2.2).

The total degeneracy of the ground state is fourfold, matching the four different topological configurations of closed loops on a torus (see Fig. 2.2). These four states allow the encoding of quantum information as logical qubits, with a closed loop of Pauli X

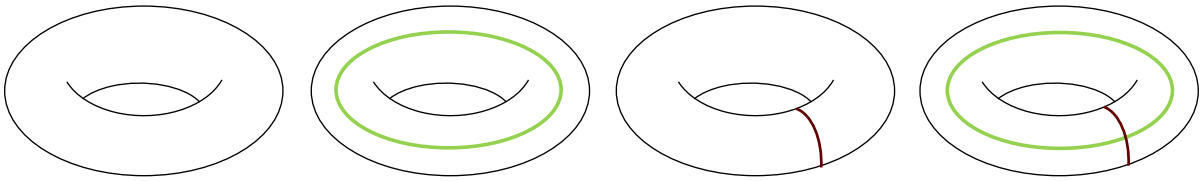

Figure 2.2: Schematic of the four different possible ground states. The topologically closed loops on the tori show paths for an m-anyon pair creation, transport and annihilation operation that reaches a different state in the degenerate ground space. Two logical qubits can be encoded using these states and they are $|00\rangle, |01\rangle, |10\rangle$ and $|11\rangle$ from left to right.

operations making up a logical gate $\bar{X}$ and similarly a closed loop of Pauli Z operations making up a logical gate $\bar{Z}$. The toric code is therefore useful as a quantum memory where anyon creation and annihilation may be necessary as part of active error correction or the performing of logical X and Z gates.

2.2 Anyon creation with bounded pulses

While it is clear that creating anyons in an ideal manner, infinitely quickly, highlights how simple anyon creation in the toric code model is and how the stability of the states which exhibit anyonic behaviour is guaranteed under the Hamiltonian, it is not yet clear whether this is the case if instead anyons were to be created in a more realistic time-dependent fashion. The whole process of anyon creation is henceforth reconsidered as a control problem.

The initial aim is to create an m-anyon pair via an X operation that is coupled to a time-dependent control $f(t)$. We wish to evolve from the ground state $|g_1\rangle$ to the anyonic eigenstate $|m\rangle = X_j |g_1\rangle$ which would correspond to two anyons on the plaquettes that act on the j-th spin. The Hamiltonian is now

$$H(t) = H_{\mathrm{TC}} + f(t)X_j. \tag{2.7}$$

This problem effectively reduces the Hilbert space of interest to two dimensions spanned

by the initial state and the target state. The reduced Hamiltonian is

$$H_{\text{reduced}}(t) = \begin{pmatrix} \langle g_1| H(t) |g_1\rangle & \langle g_1| H(t) |m\rangle \\ \langle m| H(t) |g_1\rangle & \langle m| H(t) |m\rangle \end{pmatrix} = \begin{pmatrix} -N & f(t) \\ f(t) & -N+4 \end{pmatrix}. \tag{2.8}$$

The equivalent simpler Hamiltonian $\tilde{H}(t) = -2Z + f(t)X$, differing from (2.8) only by $(-N+2)\mathbf{1}$, is now the object of interest, where the time-dependent control function $f(t)$ in (2.8) is identical to the control in (2.7). The desired evolution is from the ground state of $-2Z$ to its excited eigenstate ($|0\rangle \to |1\rangle$).

2.2.1 Constant and piecewise-constant control

Let us begin by initially assuming a constant control such that $f(t) = f$. The unitary time evolution at some time t would then be

$$U(t) = \cos\left(\sqrt{4+f^2}t\right)\mathbf{1} + \frac{2i\sin\left(\sqrt{4+f^2}t\right)}{\sqrt{4+f^2}}Z - \frac{if\sin\left(\sqrt{4+f^2}t\right)}{\sqrt{4+f^2}}X. \tag{2.9}$$

Thus the fidelity between the evolved state at time t and the target state would be

$$\mathcal{F}(t) = |\langle 1| U(t) |0\rangle|^2 = \frac{f^2\sin^2\left(\sqrt{4+f^2}t\right)}{4+f^2}. \tag{2.10}$$

While this can get arbitrarily close to unity with larger and larger magnitudes of f, in principle perfect fidelity cannot be achieved. If the control were instead *piecewise* constant however, perfect fidelity could be achieved with as few as two different constant values. For each value of f_j in the Hamiltonian, evolution would correspond to a unitary

$$U_j = \exp(-i(-2Z + f_jX)t_j) \tag{2.11}$$

where t_j is the time of evolution for which the Hamiltonian is constant. If we insist that evolution is such that the initial state is evolved to a state that is in a certain sense 'as orthogonal as possible', that is, the earliest time $t = t_j$ such that the fidelity

(2.10) is maximised, then this time interval is half the period of the dynamics induced by the Hamiltonian; thus $t_j = \frac{\pi}{2\sqrt{4+f_j^2}}$. For this general form of evolution, using two such unitaries gives the following general form for fidelity:

$$\mathcal{F} = |\langle 1| U_2 U_1 |0\rangle|^2 = \frac{4(f_1 - f_2)^2}{(4 + f_1^2)(4 + f_2^2)}. \tag{2.12}$$

This evaluates to unity if and only if $f_1 = -\frac{4}{f_2}$. It is therefore shown that a time-dependent control defined as

$$f(t) = \begin{cases} f_1 & 0 \leq t \leq t_1 \\ -4f_1^{-1} & t_1 < t \leq T \end{cases} \tag{2.13}$$

gives the required state evolution at time T where

$$T = t_1 + t_2 = \frac{\pi}{2\sqrt{4 + f_1^2}} + \frac{\pi}{2\sqrt{4 + (-\frac{4}{f_1})^2}}. \tag{2.14}$$

The simplest example of such a time-dependent control is where $f_1 = 2$ meaning that $f_2 = -2$ and $T = 2t_1 = \frac{\pi}{2\sqrt{2}}$.

2.2.2 Pulses of arbitrarily bounded magnitude

A piecewise constant control comprised of a two values where one pulse size is required to be four times the negative reciprocal of the other immediately sets a lower bound on pulse magnitude for any given upper bound. In other words if $|f_j| \leq M$ for a real M then

$$\frac{4}{M} \leq |f_j| \leq M \tag{2.15}$$

which is only valid so long as $M \geq 2$. The total time taken for the required evolution $T = t_1 + t_2$ is also bounded from below by $\frac{\pi}{4}$ as

$$\lim_{|f_1|\to 0}\left(\frac{\pi}{2\sqrt{4+f_1^2}}+\frac{\pi}{2\sqrt{4+(-\frac{4}{f_1})^2}}\right) = \lim_{|f_1|\to\infty}\left(\frac{\pi}{2\sqrt{4+f_1^2}}+\frac{\pi}{2\sqrt{4+(-\frac{4}{f_1})^2}}\right) = \frac{\pi}{4}. \tag{2.16}$$

In order to achieve the required evolution for pulses of *any* magnitude M, including those with $M < 2$, we outline a procedure that may be followed to produce a pulse that achieves this.

A constant pulse unitary evolution on the initial state $|0\rangle$ is equivalent in the Bloch sphere picture of rotation around an axis of eigenstates of $H = -2Z + fX$. This axis may be parametrised by the state vector $\cos\left(\frac{\theta}{2}\right)|0\rangle + \sin\left(\frac{\theta}{2}\right)|1\rangle$, along with its orthogonal complement $\sin\left(\frac{\theta}{2}\right)|0\rangle - \cos\left(\frac{\theta}{2}\right)|1\rangle$, as it lies on the x-z plane where $\tan(\theta) = -\frac{f}{2}$. If θ divides $\frac{\pi}{2}$ exactly then a repeated procedure of using pulses of amplitude f and $-f$, switching signs every multiple of time interval $t = \frac{\pi}{2\sqrt{4+f^2}}$, will achieve the required evolution. Geometrically this is equivalent to rotating the 'north pole' of the Bloch sphere around two axes, one at θ to the north pole and the other at $-\theta$ repeatedly until the 'south pole' is reached (see Fig. 2.3).

The following procedure therefore gives an algorithm that implements anyon creation in the toric code using a square wave pulse $f(t)$ whose magnitude can be arbitrarily bounded and still achieve the evolution in finite time: a) For a given bound M, pick an amplitude f such that $\tan^{-1}(-\frac{f}{2})$ divides $\frac{\pi}{2}$. There are infinitely many such f for any bound. b) Let the time-dependent control in the Hamiltonian be set to a square-wave pulse that alternates between f and $-f$ at every time interval $t_1 = \frac{\pi}{2\sqrt{4+f^2}}$. c) After a total of $n = \frac{\pi}{2|\theta|}$ intervals and a total time of $T = \frac{\pi^2}{8|\theta|}\cos\theta$ the required evolution is achieved.

It is reasonable to compare the total time taken using this method with the time that would be taken if there were no time-independent Z part in the Hamiltonian. Were this

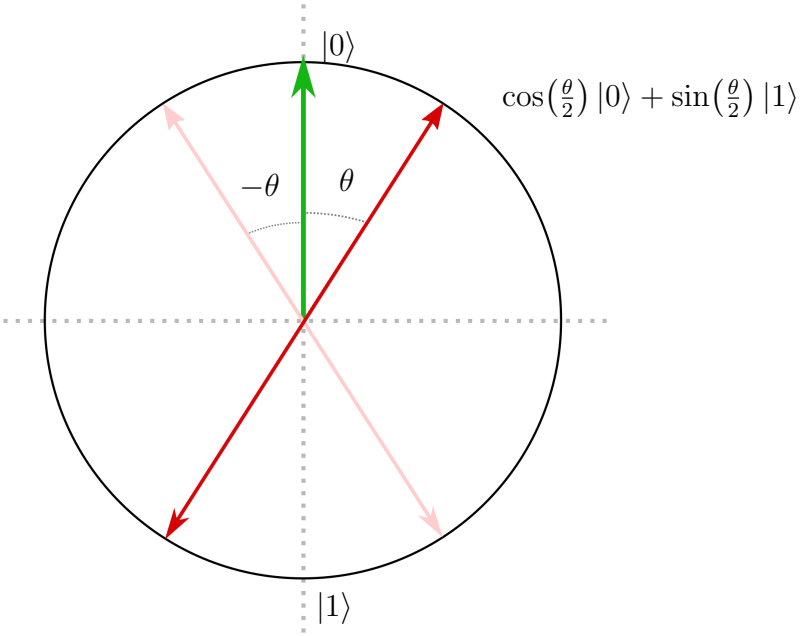

Figure 2.3: Evolution from the state $|0\rangle$ (green) to $|1\rangle$ is geometrically equivalent to rotation of the unit vector pointing due north around the axis determined by the state vector $\cos\left(\frac{\theta}{2}\right)|0\rangle + \sin\left(\frac{\theta}{2}\right)|1\rangle$ and the axis determined by $\cos\left(\frac{\theta}{2}\right)|0\rangle - \sin\left(\frac{\theta}{2}\right)|1\rangle$ in alternate fashion. If θ divides $\frac{\pi}{2}$ exactly, then $|1\rangle$ is always reachable with a finite number of rotations.

to be the case, achieving the required evolution would simply be a matter of waiting half the time period of the natural evolution of the Hamiltonian fX. This time period, t_X, is $\frac{\pi}{2|f|}$ and the ratio between t_T and t_X is given by

$$\begin{aligned} \frac{t_T}{t_X} &= \frac{\pi^2}{8|\theta|}\cos(\theta)\cdot\frac{2|f|}{\pi} \\ &= \frac{\pi|\sin\theta|}{2|\theta|} \end{aligned} \tag{2.17}$$

which approaches $\frac{\pi}{2}$ (approximately 1.5) as θ vanishes. This means that in the worst case scenario, with a smaller and smaller f bound, this method takes only about one and a half times as long to achieve the required state evolution as the ideal optimal method, given that bound f, as shown in Fig. 2.4.

2.2.3 Multiple anyon creation

In general performing error correction on logical qubits would require a process of creating (annihilating) many anyons or creating (annihilating) strings of nontrivial length. The

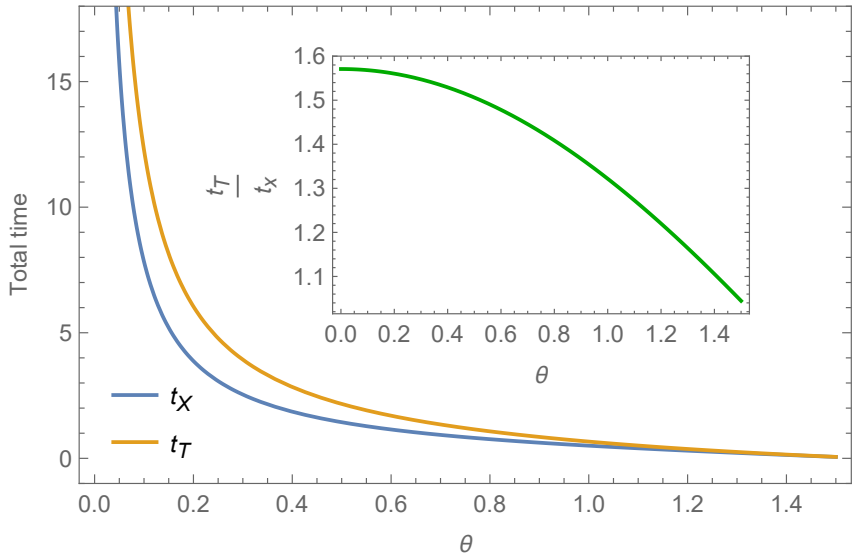

Figure 2.4: Comparison between the theoretically optimal time for state evolution t_X in blue for given values of the parameter $\theta = \tan^{-1}(-\frac{f}{2})$ and the real time t_T in yellow, which includes the drift from $-2Z$ in the Hamiltonian. **Inset:** Ratio between times t_X and t_T for increasing θ. For the worst case scenario where $\theta \to 0$ the theoretically optimum time is only approximately 1.5 times faster.

natural preference would be for this to be either one single process or otherwise a quick and efficient protocol. The problem however does not simplify as easily as the creation of one anyon pair in that the Hilbert space of interest only reduces to the size of 2^L where L is the length of an anyon string by number of qubits acted on.

The procedure developed for single anyon creation can however be used as part of a step-by-step process for creating an anyon string of arbitrary length. These steps only require two types of pulses: a square-wave pulse as previously described for creating the single anyon-pair and a constant pulse for extending an anyon pair by one plaquette (or vertex) length. The extension of an anyon string is a simpler process due to the lack of energy penalty, so that the reduced Hamiltonian is simply

$$H_{\text{reduced}} = \begin{pmatrix} -N+4 & f(t) \\ f(t) & -N+4 \end{pmatrix}. \tag{2.18}$$

The time taken to move from one anyonic state to an anyonic string state of identical energy lengthened by one spin qubit operation would simply be $t_1 = \frac{\pi}{2|f|}$.

In general, for any particular bounded pulse, the total time taken for creating a string

of length L where L is the 'qubit distance' of the anyon string would therefore be

$$T = n\frac{\pi}{2\sqrt{4+f^2}} + (L-1)\frac{\pi}{2|f|} \tag{2.19}$$

where $n = \lceil \frac{\pi}{2\theta} \rceil$ and $f = -2\tan\theta$.

2.2.4 Logical operations

The toric code allows for the encoding of two logical qubits as well as the possibility of performing the logical gates $\bar{X}$ and $\bar{Z}$. These correspond to a series of X or Z operations on the spins of the lattice carried out in the string that corresponds to a non-contractible loop. Though the problem of performing an $\bar{X}$ gate on a logical qubit as a single operation scales exponentially with the length of the lattice, using the described step-by-step method, the problem becomes tractable in that the same pulses may be used for anyon creation and annihilation, in combination with the simpler procedure with a constant pulse for anyon extension. Hence if a pulse is bounded in magnitude by F the procedure may be followed to create an anyon-pair with $n = \lceil \frac{\pi}{2\tan^{-1}\frac{F}{2}} \rceil$ unitaries, followed by a single unitary for anyon extension by one qubit (total number would therefore be $L-1$ where L is the lattice length), and the same n unitaries for anyon annihilation.

The total time taken for this would be

$$T = 2 \times \lceil \frac{\pi}{2\tan^{-1}\frac{F}{2}} \rceil \times \frac{\pi}{2\sqrt{4+F^2}} + (L-1)\frac{\pi}{2F}. \tag{2.20}$$

Hence the time increases only linearly with lattice size and decreases on the order of $\frac{1}{F}$ with pulse size.

2.3 Extrinsic errors

The use of square wave pulses as a control for anyon creation is not without its possible difficulties due to the necessity of finitely many points of discontinuity. With square-

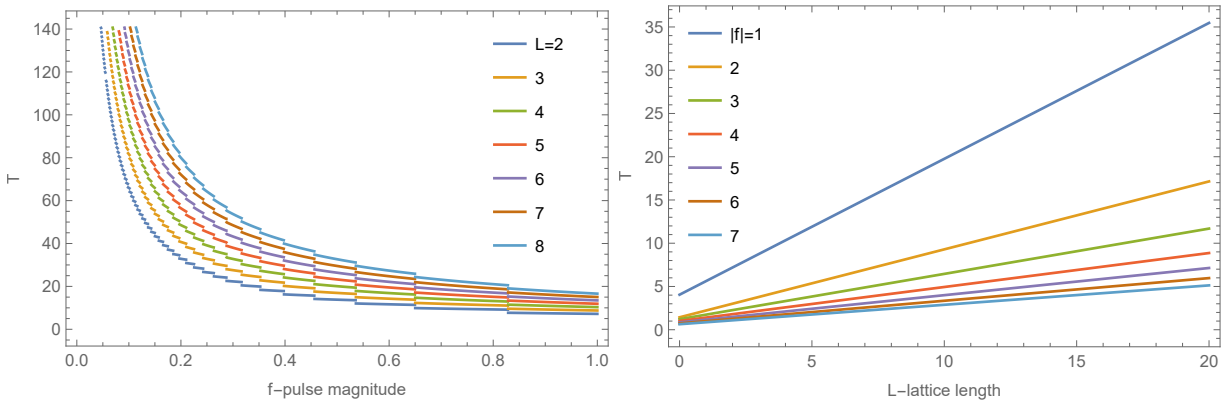

(a) **(b)**

Figure 2.5: Graphs showing **(a)** how for different lattice lengths L the pulse magnitude affects total time for performing an $\bar{X}$ gate and **(b)** how for pulses of different magnitude $|f|$ the lattice length affects total time for the same operation.

wave pulses that abruptly change value, errors in exact timing could be present when implemented experimentally and so it is necessary to investigate the effect of errors on the overall fidelities. We consider such errors to be *extrinsic* as they are not due to intrinsic errors in the Hamiltonian.

2.3.1 Gaussian errors

We investigate a Gaussian error model wherein all values of pulse amplitude and timing are normally distributed around the mean of the ideal values.

Given that in the ideal, error-free regime a number of unitaries are required for desired evolution, a generalised state fidelity function can be defined in terms of errors $\boldsymbol{\epsilon} = (\epsilon_1, \ldots, \epsilon_n)$ as

$$\mathcal{F}(\boldsymbol{\epsilon}) = |\langle 1| \left(\prod_j U_j(\epsilon_j) \right) |0\rangle|^2 \tag{2.21}$$

where the unitaries are either

$$U_j = \exp(-i(-2Z + (f_j + \epsilon_j)X)t_j) \tag{2.22}$$

for control pulse amplitude errors, or

$$U_j = \exp(-i(-2Z + f_j X)(t_j + \epsilon_j)) \tag{2.23}$$

for timing errors. In Equation (2.21) the product is understood to mean repeated *left* multiplication of unitaries.

The expected fall in state fidelities can then be compared with increased standard deviation of error by

$$\tilde{\mathcal{F}}(\sigma) = \int_{-\infty}^{\infty} \mathcal{F}(\boldsymbol{\epsilon}) \left(\prod_{j}^{n} \mathcal{N}(0, (\sigma\alpha_j)^2; \epsilon_j \right) \, d\boldsymbol{\epsilon} \tag{2.24}$$

where $\tilde{\mathcal{F}}$ is the state fidelity in the presence of errors and $\mathcal{N}(0, (\sigma\alpha_j)^2; \epsilon_j)$ is a normalised Gaussian distribution with standard deviation $\sigma\alpha_j$ proportional to the magnitude of the ideal value α_j of either the amplitude f_j or the timing t_j

$$\mathcal{N}(0, (\sigma\alpha_j)^2; \epsilon_j) = \frac{\exp\left(-\frac{\epsilon_j^2}{2\alpha^2\sigma_j^2}\right)}{\sqrt{2\pi}\alpha\sigma_j}. \tag{2.25}$$

In general, this integral is not always analytically solvable, however a series solution may be given. On the assumption of errors being small in size, only lowest order terms will be of interest. In the most general case the fidelity is

$$\mathcal{F}(\epsilon_1, \epsilon_2, ..., \epsilon_n) = |\langle 1| \Upsilon(\epsilon_1, \epsilon_2, ..., \epsilon_n) |0\rangle|^2 \tag{2.26}$$

where Υ is a product of unitaries defined as $\prod_j^n U_j(\epsilon_j)$ with n being the number of constant pulse steps. We consider this unitary product in Taylor series form

$$\Upsilon(\boldsymbol{\epsilon}) = \Upsilon_0 + \sum_j \epsilon_j \left(\frac{\partial \Upsilon}{\partial \epsilon_j}\bigg|_{\boldsymbol{\epsilon}=0} \right) + \sum_{j,k} \frac{\epsilon_j \epsilon_k}{2} \left(\frac{\partial^2 \Upsilon}{\partial \epsilon_j \epsilon_k}\bigg|_{\boldsymbol{\epsilon}=0} \right) + \sum_j \frac{\epsilon_j^2}{2} \left(\frac{\partial^2 \Upsilon}{\partial \epsilon_j^2}\bigg|_{\boldsymbol{\epsilon}=0} \right) + O(\epsilon^3) \tag{2.27}$$

where $\Upsilon_0 = \Upsilon(0, \ldots)$ is the unitary evolution operator with no errors.

As a series in $\boldsymbol{\epsilon}$ the fidelity may be expanded to arbitrary order. A simplification occurs however when integrating over a series of Gaussians in that any term of odd order, or even a term that includes any odd order of ϵ_j, vanishes when integrated over an even function such as a Gaussian centred at 0. The general rule for the integral of the product of Gaussians and *even* powers is given by

$$\int_{-\infty}^{\infty} \epsilon^n \, \mathcal{N}(0, (\sigma\alpha)^2; \epsilon) \, d\epsilon = \frac{\left(\sqrt{2}\sigma\alpha\right)^n \Gamma\left(\frac{n+1}{2}\right)}{\sqrt{\pi}} \quad \text{for } n \text{ even} \tag{2.28}$$

where $\sigma\alpha$ is the standard deviation and Γ is the standard Gamma function. For $n = 2$ this evaluates to $\alpha^2\sigma^2$ and therefore to second order the function describing fidelity as a function of the error sizes $\boldsymbol{\sigma} = (\sigma_1, \ldots, \sigma_n)$ can be written as

$$\begin{aligned}\tilde{\mathcal{F}}(\boldsymbol{\sigma}) = \; & 1 + \sum_j^n \alpha^2\sigma_j^2 \; |\, \langle 1| \, \partial_j \Upsilon \, |0\rangle \, |^2 + \left(\frac{1}{2} \sum_j^n \alpha^2\sigma_j^2 \, \langle 1| \, \Upsilon_0 \, |0\rangle\langle 0| \, \partial_j^2 \Upsilon^\dagger \, |1\rangle + \text{h.c.} \right) \\ & + \text{higher order terms}\end{aligned} \tag{2.29}$$

where $\alpha = |f_{\text{ideal}}|$ or $|t_{\text{ideal}}|$ and $\partial_j^n \Upsilon = \frac{\partial^n \Upsilon}{\partial \epsilon_j^n}$ evaluated where $\boldsymbol{\epsilon}$ vanishes.

This formula shows that for anyon creation, the errors effectively *add up* in lowest (second) order. For the simplest piecewise constant pulse which comprises of two constant pulses of opposite sign $\alpha = |f_j| = 2$, if only amplitude errors are considered, and the same standard deviation in error throughout the pulse is assumed, the following series expansion is arrived at

$$\tilde{\mathcal{F}}(\sigma) = 1 - \left(\frac{1}{2} + \frac{\pi^2}{16} \right) \sigma^2 - \left(\frac{3}{4} - \frac{3\pi^2}{32} - \frac{\pi^4}{256} \right) \sigma^4 + O(\sigma^6) \tag{2.30}$$

to lowest orders. Numerically this is approximately $\tilde{\mathcal{F}} = 1 - 1.11685\sigma^2 + 0.55578\sigma^4$. By symmetry it can be deduced that if both pulse amplitudes f_1 and f_2 had independent errors σ_1 and σ_2 respectively, then half the second order coefficient in (2.30) would multiply $\sigma_1^2 + \sigma_2^2$; numerically this is $1 - 0.558425(\sigma_1^2 + \sigma_2^2)$.

For the case of timing errors the necessary integral can be computed exactly; the same

2-valued pulse where $\alpha = t_j = \frac{\pi}{4\sqrt{2}}$ gives

$$\tilde{\mathcal{F}}(\tau) = \frac{1}{2} + \frac{1}{2}e^{-\frac{\pi^2\tau^2}{2}} = 1 - \frac{\pi^2\tau^2}{4} + \frac{\pi^4\tau^4}{16} + O(\tau^6) \tag{2.31}$$

or, if the two parts of the piecewise-constant function are independent and possibly differ, this becomes $\frac{1}{2} + \frac{1}{4}\left(e^{-\frac{\pi^2\tau_1^2}{2}} + e^{-\frac{\pi^2\tau_2^2}{2}}\right)$. The Gaussian form of the fidelity can be seen for general errors, showing that fidelities will always be given in terms of even orders. In Fig. 2.6 we see such a Gaussian form in the fidelity drop, as well as the fact that stability is very high for pulse amplitudes, as a standard deviation of $0.1 f_{\text{ideal}}$ for amplitude error would only lead to a fidelity drop of approximately 1%. Relatively good stability is also present for timing errors as a high standard deviation of error $0.15 t_{\text{ideal}}$ would mean approximately 3% drop in fidelity.

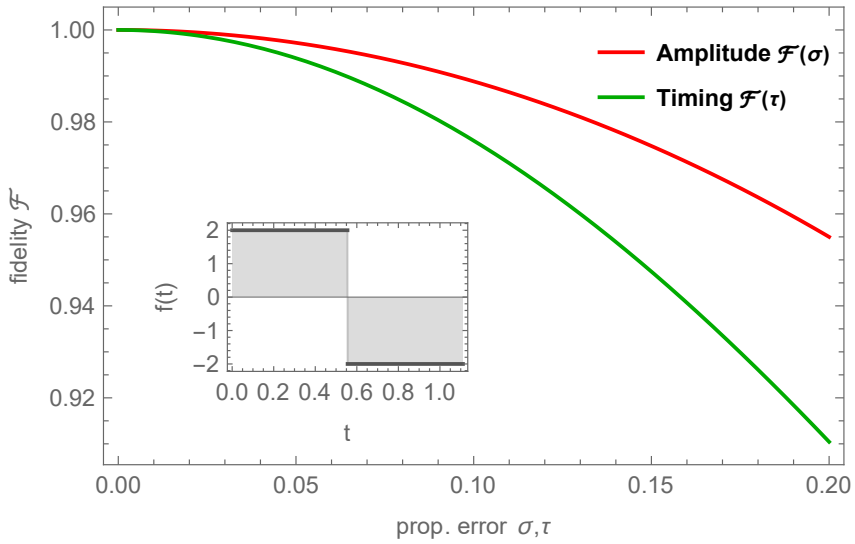

Figure 2.6: Graph showing how, for the simplest control pulse (**inset**), fidelities are affected by increasing proportional error, σ or τ; the exact standard deviations being σf_{ideal} and σt_{ideal}. The error is assumed to be uniform for each piecewise constant part of the pulse. Shown explicitly is the exact drop in fidelity with timing error (green) and the drop in fidelity with amplitude error (red) plotted to fourth order.

2.3.2 Extrinsic errors in multiple anyon creation

It is to be expect that if there are errors either with the amplitudes or the timings in the control pulses, fidelities will then naturally decrease. Due to the method of carrying out

logical operations with pulses on one spin at a time, the adverse effects of errors will be compounded. A natural question to ask therefore is, given the compounding of error in the step-by-step process of carrying out a logical operation, or indeed creating any anyon string of non-trivial length, how large can a lattice be before the drop in fidelity becomes too large. Or conversely, given a lattice of a certain size, what's the highest allowable size of error before the fidelities drop to intolerable levels.

Given the multi-step nature of the procedure, implying multiple unitaries, the full analysis can only be given by calculation of large multi-volume integrals. However given that each process, when done perfectly, is only a two-dimensional problem, every imperfect process therefore only creates a superposition state between the target state and the initial state. One can therefore focus solely on the reduced fidelity of the target state in each process. This indicates that to lowest order, errors may simply be added up and, as the lowest order in errors is second order, the same procedure as previously presented may be used to see how fidelities drop to second order.

An illustrative concrete example may be given by looking at the simplest anyon creation, extension and annihilation scenario on a 3-by-3 lattice comprised of 18 qubits. This scenario amounts to performing an $\bar{X}$-gate using pulses acting on three adjacent qubits labelled 1,2 and 3. With the most efficient pulse, which is the two-valued piecewise-constant pulse

$$f(t) = \begin{cases} 2 & 0 \leq t \leq \dfrac{\pi}{4\sqrt{2}} \\ -2 & \dfrac{\pi}{4\sqrt{2}} < t \leq \dfrac{\pi}{2\sqrt{2}} \end{cases}, \tag{2.32}$$

perfect fidelity is reached when using the following unitaries

$$U_1(t) = \exp\left(-i\frac{\pi}{2\sqrt{2}}(H_{\mathrm{TC}} + f(t)X_1)\right) \tag{2.33}$$

$$U_2(t) = \exp\left(-i\frac{\pi}{4}(H_{\mathrm{TC}} + 2X_2)\right) \tag{2.34}$$

$$U_3(t) = \exp\left(-i\frac{\pi}{2\sqrt{2}}(H_{\mathrm{TC}} + f(t)X_3)\right) \tag{2.35}$$

For amplitude errors the fidelity is

$$\begin{aligned}\tilde{\mathcal{F}} &= 1 - \sum_{j=1}^{4}(\frac{1}{4} - \frac{\pi^2}{32})\sigma_j^2 - \frac{\pi^2}{4}\tilde{\sigma}^2 + \text{h.o.t} \\ &\approx 1 - \sum_{j=1}^{4} 0.5584\sigma_j^2 - 2.4674\tilde{\sigma}^2 \end{aligned} \tag{2.36}$$

where $\tilde{\sigma}$ is the error for the constant pulse used in $U_2(t)$ which is used for extending the anyon string and σ_j are the errors for creation and annihilation pulses used in $U_1(t)$ and $U_3(t)$.

If all errors are of equal proportion then it can be shown what errors are tolerable (to lowest order) for a fidelity above 90%. For example, in the aforementioned 3-by-3 lattice example, with respect to timing errors, a maximum error of up to approximately 7% is tolerable before fidelities drop too low. These would be errors as proportions of the ideal values.

Due to the simplicity of adding coefficients in second order, one can easily extend the equation for the fidelity to lattices of arbitrary length L

$$\tilde{F} = 1 - \left(\frac{1}{4} - \frac{\pi^2}{32}\right)\sigma_j^2 - (L-2)\frac{\pi^2}{4}\tilde{\sigma}^2 \tag{2.37}$$

This shows that while large lattices for the toric code can be good for quantum error correction purposes, with our method, this will come at a cost to tolerable error in creating many anyons and performing simple logical operations such as $\bar{X}$. In Fig. 2.7 is illustrated how there is an inverse proportional relationship between increased lattice length L and the tolerable error for a fidelity of 1%.

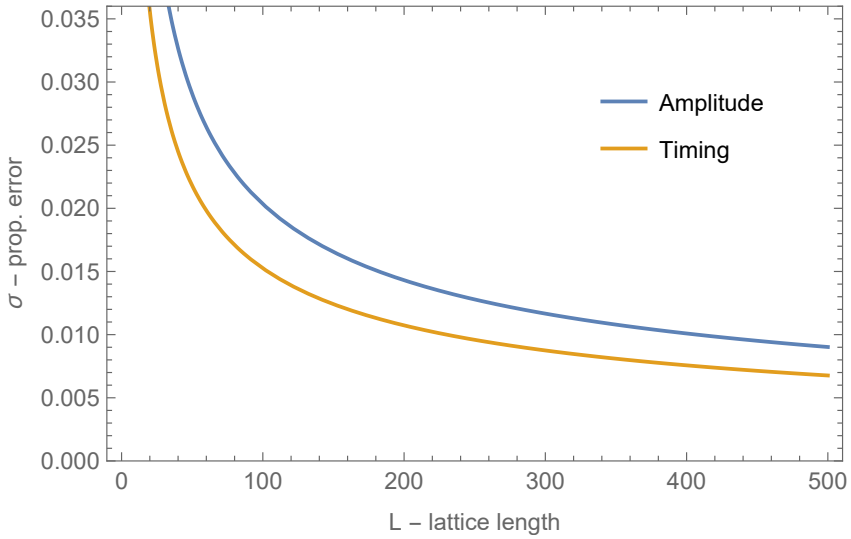

Figure 2.7: Graph showing the proportional errors σ that lead to an overall fidelity of 90% for increasing lattice lengths L. There a decrease of the order of inverse root of length of the lattice L. For example for a lattice 500 qubits in length, around 1% error in timing is tolerable.

2.4 Background noise and intrinsic errors in the Hamiltonian

While time-dependent anyon creation in the toric code seems to be robust to possible extrinsic errors in timing and magnitude of pulses, were errors to be *intrinsic* to the Hamiltonian, the situation would become more complex. This corresponds to investigating the original time-independent toric code Hamiltonian (2.1) with added error terms

$$H = H_{\mathrm{TC}} + \sum_j h_j X_j \tag{2.38}$$

where the error factors h_j could possibly be the same on all qubits or independent, but in either case would have to be small so as not to disrupt the topological properties of the code too significantly. Given that the Hamiltonian is no longer trivially diagonalisable, perturbative methods will be used to see how these intrinsic errors affect topologically protected states. Free evolution of toric code eigenstates under this perturbed Hamiltonian will be investigated in order to compare its effects with that of anyon creation in the presence of perturbations. This will then be used to demonstrate why larger toric code lattices, while not showing marked improvement in fidelity *do* nevertheless provide

a topological level of protection against logical qubit error.

2.4.1 Free evolution with intrinsic noise

The evolution of a general eigenstate of the toric code $|g\rangle$ can be examined in terms of its fidelity with the original state, that is

$$\mathcal{F}_g = |\langle g| e^{-i\left(H_{\mathrm{TC}}+\sum_j h_j X_j\right)t} |g\rangle|^2 = |\langle g| U(h_1, h_2, ...) |g\rangle|^2. \tag{2.39}$$

Once again it is convenient to expand the unitary propagator as an expansion in terms of small errors h_j so that

$$U(h_1, h_2, ...) = U_{\mathbf{0}} + \sum_j h_j \frac{\partial U}{\partial h_j} + \sum_{i,j} \frac{h_j h_k}{2!} \frac{\partial^2 U}{\partial h_j \partial h_k} + ... \tag{2.40}$$

When the propagator is given as an expansion the fidelity $\mathcal{F}_g$ can be described up to arbitrary order. We will investigate the fidelity only up to the lowest orders as we assume the magnitude of error fields are small.

There is only a single term in zeroth order which is clearly $\langle g| U |g\rangle\langle g| U^\dagger |g\rangle = 1$. The first order terms are all of the form:

$$h_j \langle g| \partial_{h_j} U |g\rangle\langle g| U^\dagger |g\rangle + \text{hermitian conjugate} \tag{2.41}$$

These in fact all disappear due to the vanishing of $\langle g| \partial_{h_j} U |g\rangle$. This may be seen explicitly from the identity [52]

$$\langle g| \partial_{h_j} U |g\rangle = \langle g| \left(-i \int_0^t e^{-i(t-u)H_{\mathrm{TC}}} X_j e^{-iuH_{\mathrm{TC}}} \, du \right) |g\rangle \tag{2.42}$$

where H_{TC} is the unperturbed toric code Hamiltonian and $iX_j = \frac{\partial H}{\partial h_j}$. As $|g\rangle$ is an eigenstate of H_{TC} and $X_j |g\rangle$ is both another eigenstate and orthogonal to $|g\rangle$, the term (2.42) ultimately vanishes. Indeed this also means that any term in the series expansion of $\mathcal{F}_g$ that is a product of first order terms also disappears. The second order terms in

the fidelity come in two forms, the first in the form

$$h_j h_k^* \langle g| \partial_{h_j} U |g\rangle\langle g| \partial_{h_j} U^\dagger |g\rangle + \text{h.c.} \tag{2.43}$$

and the second in the form

$$\frac{h_j h_k}{2!} \langle g| \frac{\partial^2 U}{\partial h_j \partial h_k} |g\rangle\langle g| U^\dagger |g\rangle + \text{h.c.} \tag{2.44}$$

Though h_j is always real and hence is equal to h_j^*, it is useful to state terms in this form in order to more easily keep track of multiplicands.

Those second order terms in the first form must vanish from the fidelity for the same reason that the first order terms in the fidelity disappear. Moreover it turns out that of those terms in the second form, those which are cross terms (i.e. where $j \neq k$) *also* vanish. This can be seen from the fact that

$$\langle g| \frac{\partial^2 U}{\partial h_j \partial h_k} |g\rangle = -2 \quad \langle g| \int_0^t \int_0^u du\ dv\ e^{-i(t-u)H_{\text{TC}}} X_j e^{-i(u-v)H_{\text{TC}}} X_k e^{-ivH_{\text{TC}}} |g\rangle . \tag{2.45}$$

For similar reasons as with the first order case this vanishes if $j \neq k$ as $X_j X_k |g\rangle$ is a higher anyonic energy eigenstate of H_{TC} and so is orthogonal to $|g\rangle$. This immediately shows that to second order, the total fidelity error in the system can simply be the sum of the individual errors on each qubit in the lattice.

For completeness, we can see that for the case of $j = k$ we get

$$\begin{aligned} \langle g| \frac{\partial^2 U}{\partial {h_j}^2} |g\rangle &= -2 \int_0^t du \int_0^u dv\ e^{-i(t-u)E_g} e^{-i(u-v)E_X} e^{-ivE_g} \\ &= \frac{-2ite^{-iE_g t}}{(E_g - E_X)} + \frac{2(e^{-iE_X t} - e^{-iE_g t})}{(E_g - E_X)^2} \end{aligned} \tag{2.46}$$

where E_g and E_X are the energy eigenvalues of the states $|g\rangle$ and $X_j |g\rangle$ respectively.

Together with the phase factor from the $\langle g| U |g\rangle$ parts of the expression, this gives

the following evaluation for all of the non-vanishing second order terms:

$$\frac{h_j^2}{2!}\langle g|\,\partial_{h_j}^2 U\,|g\rangle\langle g|\,U^\dagger\,|g\rangle + \text{h.c.} = h_j^2\,\frac{2(\cos((E_g-E_X)t)-1)}{(E_g-E_X)^2} \tag{2.47}$$

Indeed there are times t when even these second order terms vanish. Whether there is an error present only on one qubit or on every qubit in the lattice, the first non-zero time for which this is the case, assuming $E_X > E_g$, is $t = \frac{2\pi}{E_X - E_g} = \frac{\pi}{2}$.

2.4.2 Time-dependent anyon creation with noise

It can also be shown that in the more novel scenario where time-dependent anyon creation is attempted in the presence of these unwanted X-fields, fidelities to lowest order can still be summed up from instances where errors act on each qubit separately.

To see how the presence of errors affects the creation of an anyon pair, i.e. the evolution from $|g\rangle$ to $|X_k g\rangle$, the fidelity is defined as

$$\mathcal{F} = |\,\langle X_k g|\,U_2(h_1,h_2,...)U_1(h_1,h_2,...)\,|g\rangle\,|^2 \tag{2.48}$$

where $U_1(\boldsymbol{h}) = e^{-i(H_{\text{TC}}-2X_k+\sum_j h_j X_j)\tau}$ and $U_2(\boldsymbol{h}) = e^{-i(H_{\text{TC}}+2X_k+\sum_j h_j X_j)\tau}$ are the two unitary matrices that without errors would give perfect fidelity with $\tau = \frac{\pi}{4\sqrt{2}}$.

Once again propagators will be expanded in terms of small h_j errors, as in (2.39), remembering that this time however we have two expansions to bear in mind. This would lead to the zeroth order term in the fidelity again being unity. The first order terms would then be

$$\begin{aligned}&\sum_j h_j\,\langle X_k g|\,\frac{\partial U_2}{\partial h_j}\,U_1\,|g\rangle\langle g|\,U_1^\dagger U_2^\dagger\,|X_k g\rangle \;+\; \text{h.c.}\\ +\;&\sum_j h_j\,\langle X_k g|\,U_2\,\frac{\partial U_1}{\partial h_j}\,|g\rangle\langle g|\,U_1^\dagger U_2^\dagger\,|X_k g\rangle \;+\; \text{h.c.}\end{aligned} \tag{2.49}$$

Given that one of the error-free unitaries acting on a state leads to an equal superposition

of the original state and the anyonic state, up to a global phase, i.e.

$$U_1 |g\rangle = e^{-i(H_{\mathrm{TC}}-2X_k)\tau} |g\rangle = e^{i\lambda} \left(\frac{|g\rangle + |X_k g\rangle}{\sqrt{2}} \right) \tag{2.50}$$

then it should be immediately clear that all first order terms where $j \neq k$ vanish for similar reasons as those given in the example of free evolution. It remains therefore only to look at the examples where $j = k$. These comprise of two terms plus their respective complex conjugates so for these terms to vanish it need only be shown that they are ultimately the sum of purely imaginary terms.

Firstly it can be shown, using the reduced Hamiltonian described in Section 2,

$$H(t) = \begin{pmatrix} -N & f(t) \\ f(t) & -N+4 \end{pmatrix}, \tag{2.51}$$

that the phase gained from creating the anyon-pair perfectly is

$$\langle X_k g| U_2 U_1 |g\rangle = e^{\frac{i\pi(N-2)}{2\sqrt{2}}} \tag{2.52}$$

where N (an even number) is the number of spin qubits in the toric code lattice. Secondly, the first order terms that get multiplied by the phase are in fact equivalent and are

$$\langle X_k g| \ \frac{\partial U_2}{\partial h_k} \ U_1 |g\rangle = \langle X_k g| \ U_2 \ \frac{\partial U_1}{\partial h_k} |g\rangle = -\frac{i\pi e^{\frac{i\pi(N-2)}{2\sqrt{2}}}}{8\sqrt{2}}. \tag{2.53}$$

The first order terms which are left are therefore now

$$\frac{-i\pi}{8\sqrt{2}} + \text{h.c.} + \frac{-i\pi}{8\sqrt{2}} + \text{h.c.} = -i\pi\tau + \text{h.c.} = 0. \tag{2.54}$$

For the same reason as in the first order case, all second order cross terms that include an error acting on a qubit other than k can be neglected. Therefore the conclusion is that to lowest (second) order one can once again add up the drop in fidelities that are caused by errors on individual qubits.

A nontrivial toric code example

As an illustrative example we may use what has been described thus far on the simplest non-trivial toric code lattice where all vertex and plaquette operators are well defined, namely an 8-qubit square lattice with four vertices and plaquettes (see Fig. 2.8).

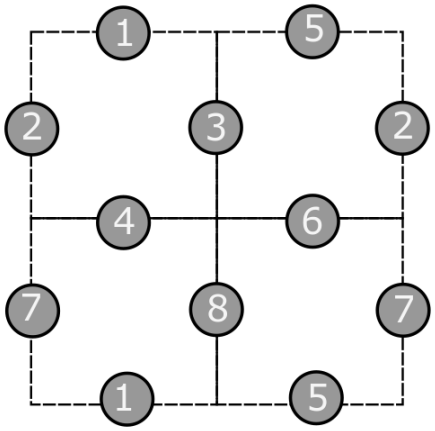

Figure 2.8: The simplest non-trivial toric code which consists of 4 plaquettes and 4 vertices with number of qubits $N = 8$

If the system starts with the ground state $|g_1\rangle = \prod_v (\mathbb{1} + A_v) |0\rangle^{\otimes 8}$ and the target is to create an anyon pair on plaquettes $p_{1,2,3,4}$ and $p_{2,3,5,6}$, a Pauli X-pulse on qubit 3 can be implemented. Given that to second order we may simply add up the contributions to the drop in fidelity for an error on each qubit individually, the simpler reduced Hamiltonian

$$H_{\mathrm{TC}} + f(t)X_3 + h_j X_j \longleftrightarrow \begin{pmatrix} E_g & f(t) & h_j & 0 \\ f(t) & E_{X_3 g} & 0 & h_j \\ h_j & 0 & E_{X_j g} & f(t) \\ 0 & h_j & f(t) & E_{X_j X_3 g} \end{pmatrix} \tag{2.55}$$

may be used, where E_g is the ground state energy -8 and $E_{X_j g}$ is the energy of the state $|X_j g_1\rangle$ which is -4 for all j. A little more care has to be taken for $E_{X_j X_3 g}$ as depending on where j is the energy eigenvalues differ. Errors on qubits adjacent to the target qubit will contribute to the extension of the anyon string and will have energy -4 and qubits elsewhere will create new anyon pairs and so will give have an energy 0. If qubit j is

itself 3, corresponding to an error on the target qubit and effectively an amplitude error in the pulse, then the energy will be the ground state energy. This would also require considering an even simpler reduced matrix as the Hilbert space would be reduced to just two dimensions. A little extra care must be taken on examples such as this one where an anyon string of length 2 will lead to a logical gate, that is, $|X_2X_3g_0\rangle$ is not simply an anyon string but a non-contractible loop around the torus and therefore $|X_2X_3g_0\rangle$ is another ground state $|g_2\rangle$.

At time $\tau = \frac{\pi}{4\sqrt{2}}$ the fidelity of the evolved state $|\psi\rangle$ with the ideal state $|X_3g_1\rangle$ will be of the form

$$\mathcal{F}(h_1, h_2, ...) = |\langle X_3g_1|\psi\rangle|^2 = 1 + \sum_j^8 \alpha_j h_j^2 + \text{h.o.t.} \tag{2.56}$$

The relevant numerical calculations show that where $j = 1, 4, 5, 6$, i.e. errors on qubits adjacent to the target qubit,

$$\alpha_j = \beta_1 = \frac{1}{4}\left(-5 + 3\sqrt{2}\sin\left(\frac{\pi}{\sqrt{2}}\right) + 2\cos\left(\frac{\pi}{\sqrt{2}}\right)\right) \approx -0.70889. \tag{2.57}$$

When $j = 7, 8$ and errors are away from the target qubit then

$$\alpha_j = \beta_2 = \frac{1}{8}\left(\cos\left(\sqrt{2}\pi\right) - 1\right) \approx -0.158282. \tag{2.58}$$

On qubit $j = 2$ the factor is $-\frac{\pi^2}{32} \approx -0.308425$. When the error is on the same qubit as the target qubit, here the target qubit is 3, the second order terms in fact cancel out and the lowest order fidelity drop is to fourth order.

This can be generalised exactly for a lattice of any size. For larger lattices where the lattice width is 3 qubits or more, there are four adjacent qubits plus two on either side that will contribute to the 'anyon-extension' fidelity drop, while all others which are more distant from the target qubit, will contribute to anyon-creation fidelity drops. The

general formula

$$\mathcal{F}(\boldsymbol{h}) = 1 + \sum_{j}^{6} \beta_1 h_i^2 + \sum_{j}^{N-6} \beta_2 h_j^2 + \text{h.o.t} \tag{2.59}$$

can be used as a good approximation to see what magnitude of errors h are tolerable for larger and larger lattices. For example, with a 500-spin lattice, if a fidelity of 90% is tolerable then the maximum error on each qubit must have a magnitude no greater than approximately 0.0348272 which as a proportion of the energy level splitting is roughly 0.87%. Conversely if an error of 1% of the energy gap 4 is accepted then a maximal lattice size of approximately 390 spins is required.

2.4.3 Logical X-gate operation

The simplest logical gates that may be performed on logical qubits encoded in the toric code lattice arise out of many successive steps that include anyon creation, string extension and finally anyon annihilation. In order to see how intrinsic error in the Hamiltonian affects this process one can first list the three steps to performing a logical gate: i) Create an anyon pair using (at least) two unitaries of the form $U = e^{-i(H_{\text{TC}} \pm f X_j)\tau}$. In the simplest and quickest example $f = \pm 2$ and $\tau = \frac{\pi}{4\sqrt{2}}$. ii) Extend an anyon string using only one unitary at a time of the form $U = e^{-i(H_{\text{TC}} + f X_j)t}$ where if $f = 2$ then $t = \frac{\pi}{4}$. ii) Annihilate an anyon string in effectively the same process as anyon creation.

Considering the simplest non-trivial example where this three step process can take place - on a lattice which is three qubits in width - this would then take at least five unitaries. Here we illustrate how to perform a logical $\bar{X}$-operation on ground state $|g_1\rangle$ so that we get $\bar{X}\,|g_1\rangle = |g_2\rangle$. In an error free regime, the product of many unitaries would be required to get $|\,\langle g_2| \prod_i^k U_j\,|g_1\rangle\,|^2 = 1$ where k is $4 + L - 2$ and L is the width of the lattice in terms of plaquettes. In the erroneous regime, a generalised fidelity is defined as

$$\mathcal{F}(\boldsymbol{h}) = |\,\langle g_2| \left(\prod_{j}^{k} U_j(\mathbf{h}) \right) |g_1\rangle\,|^2. \tag{2.60}$$

This generalised behaviour behaves somewhat similarly to the single anyon-pair example in that the zeroth order term is clearly unity. Other orders can be more complicated however. To get an idea of what the fidelity would look like we use simplified two qubit problems to work out the phase gained by the operations of creating, extending and annihilating anyon strings. These results can be summarised as follows:

- Anyon creation[1]: $|g\rangle \to \varphi_c |X_j g\rangle$ where $\varphi_c = e^{i\tau(N-2)}$
- Anyon annihilation: $|\prod_k X_k g_1\rangle \to \varphi_a |g_2\rangle$ where $\varphi_a = -\varphi_c$
- Anyon extension: $|\prod_k X_k g\rangle \to \varphi_e |X_j \prod X_k g\rangle$ where $\varphi_e = -ie^{i\tau_2 N}$
- 'Half-anyon' creation: $|g\rangle \to \frac{\varphi_{hc}}{\sqrt{2}} (|g\rangle + |X_j g\rangle)$ where $\varphi_{hc} = ie^{i\tau(N-2)}$
- 'Half-anyon' annihilation: $|\prod_k X_k g_1\rangle \to \frac{\varphi_{ha}}{\sqrt{2}} (|\prod_k X_k g\rangle - |g_2\rangle)$ where $\varphi_{ha} = -\varphi_{hc}$.

These results can be used to show that first order terms in the fidelity disappear, however further terms will in general *not* disappear.

2.4.4 Topological improvement

In the examples thus far observed, both in free evolution or anyon creation, the compounding nature of the effect of errors with number of qubits in the system seems to imply no advantage in qubit protection for larger toric code lattices, or even in any lattice at all. We now discuss why the topological protection, stemming from the degeneracies in the toric code do in fact help give extra protection.

Infidelities and non-correctable states

Once an error field such as $\sum_j h_j X_i$ is turned on in the toric code, an initialised ground state will immediately evolve into a superposition of every possible eigenstate of the unperturbed system. While this superposition is heavily biased towards the outcome of measurement being the desired eigenstate, assuming that the error is small, there is

[1]Recall that $\tau = \frac{\pi}{4\sqrt{2}}$ is half the duration of anyon creation/annihilation. $\tau_2 = \frac{\pi}{4}$ is the duration of anyon string extension.

nevertheless immediately a finite possibility of collapsing the superposition state into any erroneous, undesired eigenstate. Most of these however can be corrected if infinitely quick and perfect anyon creation is assumed. Those that can be corrected easily are states which have a different anyon configuration to the desired eigenstate, as anyon number and location can be locally measured. No local distinguishment can be made however between states of the same anyon configuration as there is a fourfold degeneracy in any anyon-configuration in the toric code.

For any generic toric code eigenstate $|\psi\rangle$, there are three other orthogonal states with the same anyon configuration, namely $\bar{X}_1|\psi\rangle$, $\bar{X}_2|\psi\rangle$ and $\bar{X}_1\bar{X}_2|\psi\rangle$ where $\bar{X}_j$ refers to one of two possible logical X-gates that may be performed corresponding to non-contractible loops of single-spin X operations around the torus. As these are the only states that correspond to logical error it is sensible to investigate *infidelities* corresponding to the probabilities of ending up in any of these logical error states and aiming to suppress them. In other words, if initialised in a ground state $|g_j\rangle$ then the appropriate measure of logical infidelity, is

$$\mathcal{I} = \sum_{k\neq j} |\langle g_k| e^{-i(H_{\mathrm{TC}}+\sum h_j X_j)t} |g_j\rangle|^2 \tag{2.61}$$

where $|g_2\rangle$ is defined as $\bar{X}_1|g_1\rangle$, $|g_3\rangle = \bar{X}_2|g_1\rangle$ and $|g_4\rangle = \bar{X}_1\bar{X}_2|g_1\rangle$.

Immediately it becomes apparent that the order of this infidelity is contingent on the lattice size. If a lattice consists of $m \times n$ plaquettes (where $m \leq n$) then the lowest order in the infidelity will be at least $2m$. This can be seen explicitly through the 8-qubit toric code example. From Fig. 2.8 if the system is initialised in ground state $|g_1\rangle$ then $|g_2\rangle = X_2X_3|g_1\rangle = X_7X_8|g_1\rangle$, $|g_3\rangle = X_1X_4|g_1\rangle = X_5X_6|g_1\rangle$, and $|g_4\rangle = X_2X_3X_1X_4|g_1\rangle = X_7X_8X_5X_6|g_1\rangle$.

If the perturbed Hamiltonian of the system is $H_{\mathrm{TC}} + \sum_i^8 h_j X_j$ then the lowest order nonzero term in the expansion of the infidelity is of the form

$$\frac{1}{2!}h_\mu h_\nu \langle g_j| \frac{\partial^2 U}{\partial h_\mu \partial h_\nu} |g_1\rangle\langle g_1| \frac{\partial^2 U}{\partial h_\alpha \partial h_\beta}^\dagger |g_j\rangle \frac{1}{2!}h_\alpha h_\beta \quad + \text{ h.c} \tag{2.62}$$

where $|g_j\rangle = |X_\mu X_\nu g_1\rangle$. This term is only nonzero if *both* overlaps are nonzero. Therefore the only allowable combinations for $h_\mu h_\nu h_\alpha h_\beta$ are $h_1^2h_4^2, h_2^2h_3^2, h_5^2h_6^2, h_7^2h_8^2, h_1h_4h_5h_6$ and $h_2h_3h_7h_8$. Clearly the lowest non-zero order is indeed of order $2m = 4$. For completeness we shall note that the full expression for the lowest nonzero order in the infidelity is

$$\mathcal{I} = \frac{1}{32}(1 + 8t^2 - \cos 4t - 4t \sin 4t)(h_2^2h_3^2 + h_1^2h_4^2 + h_5^2h_6^2 + h_7^2h_8^2 + 2h_1h_4h_5h_6 + 2h_2h_7h_8h_3) \tag{2.63}$$

$$= 2 \times (2!)^2 \times \frac{1}{(2!)^2}|k|^2 \times (h_2^2h_3^2 + h_1^2h_4^2 + ...) \tag{2.64}$$

$$= \kappa(h_2^2h_3^2 + h_1^2h_4^2 + ...) \tag{2.65}$$

$$= \kappa((h_2h_3 + h_7h_8)^2 + (h_1h_4 + h_5h_6)^2) \tag{2.66}$$

where $\kappa = 2|k|^2$. The most general definition of the factor k, for any $m \times n$ size lattice, again assuming that $m \leq n$, is

$$k = i^m \times m! \times \int_0^t \int_0^{u_1} ... \int_0^{u_{m-2}} \int_0^{u_{m-1}} d^m u \, e^{-i(t-u_1)E_g} e^{-i(u_1-u_2)E_{X_{m-1}}} ... e^{-i(u_{m-1}-u_m)E_{X_1}} e^{-iu_mE_g} \tag{2.67}$$

where E_g is the energy eigenvalue of the desired state $|g_1\rangle$ and E_{X_1} the eigenvalue of $|X_jg_1\rangle$ and so on. Once again the advantage of having a larger lattice size given in terms of logical qubit protection becomes clear; as the factor k is of the order of t, the factor of κ is therefore of the order t^2 and so, roughly speaking, with larger and larger lattices there will be less and less time for the errors to build up to become a logical X gate which causes a logical error. Less crudely we have

$$\mathcal{I} \sim h^{2m}t^2 \tag{2.68}$$

so that $t \sim \frac{\sqrt{\mathcal{I}}}{h^m}$ meaning that with larger lattice sizes the time taken for infidelity to grow gets extremely long.

A corollary of this is the lack of advantage in using non-square lattices, a rectangular lattice could even be a liability in that, for example, a 3-by-2 lattice would have a

marginally higher infidelity than a 2-by-2 lattice, due to the extra possible path for a logical X-error to build up. In an m-by-m plaquette lattice $2m^2$ is the factor that multiplies h^{2m} whereas on a lattice of size m-by-n with $m < n$ then this factor is n^2 which may be larger than m^2 for $n > \sqrt{2}m$. As $3 > 2$ one would expect the lowest order infidelity in a 3-by-2 plaquette lattice to be $\frac{9}{8}$ times that of a 2-by-2 lattice and hence offering worse protection.

Infidelities during anyon creation

The results obtained so far indicate that the toric code's robustness will be maintained for anyon-creation in a time-dependent manner, as earlier it was shown that anyon creation time is independent of lattice size, $T = 2\tau = \frac{\pi}{2\sqrt{2}}$.

For an $m \times m$ lattice [2] with spin j the target qubit for anyon creation, the appropriate measure of infidelity would be between state $|X_j g_1\rangle$ and $\bar{X}_1 |X_j g_1\rangle, \bar{X}_2 |X_j g_1\rangle$ and $\bar{X}_1\bar{X}_2 |X_j g_1\rangle$ where $\bar{X}_j$ are the two possible logical X-gates.

Much of the results for infidelities under free evolution apply to the case of anyon creation. One essential difference comes from the fact that a target qubit j may itself be used as part of a logical X gate. For a given m-by-n lattice with $m < n$, the 'simplest' logical gate will consist of m Pauli X operations on a string of qubits, $\bar{X}_1 = X_1 X_2 ... X_m$. For the general lattice there are n topologically equivalent ways of performing X_1 with m qubits, one of which includes qubit j, the target qubit on which the anyon-pair is to be created. Thus without loss of generality, one may define $\bar{X}_1 = X_1 X_2 ... X_j ... X_m$. As the Pauli matrices square to the identity, then

$$\bar{X}_1 |X_j g_1\rangle = X_1 X_2 ... X_{j-1} X_{j+1} ... X_m. \tag{2.69}$$

This is therefore equivalent to only $m - 1$ X operations on the initial state $|g_1\rangle$. Hence

[2] At this point it is no longer necessary to look at lattices that are not square as the crucial length is the shortest side.

the lowest order infidelity, defined by

$$\mathcal{I} = \sum_{k=1}^{3} \left\langle \bar{X}_k X_j g_1 \right| e^{-i\tau(H_+ + h\sum X_k)} e^{-i\tau(H_- + h\sum X_k)} \left| g_1 \right\rangle \tag{2.70}$$

where $\bar{X}_k$ are the three topological $\bar{X}$-gate operations that can be performed, is of the order $2(m-1)$, rather than $2m$ as in the example of free evolution. In this equation $H_\pm = H_{\mathrm{TC}} \pm 2X_j$. An example of the implementation of this general statement is seen in Fig. 2.9.

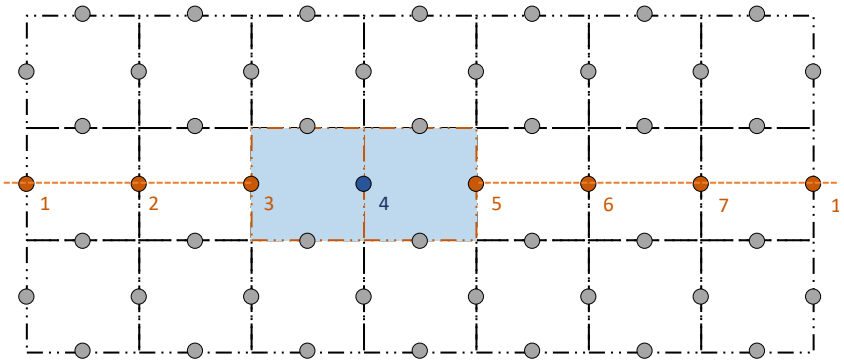

Figure 2.9: An example of a lattice of 7 columns by n rows where $n > 7$ and only 3 rows are shown. Clearly the anyon configuration above can be achieved by X_4 acting on $|g_1\rangle$ or $X_1X_2X_3X_5X_6X_7 |g_1\rangle$ suggesting that the lowest order infidelity will be h^{12}. For the free evolution case it would instead be h^{14}.

2.5 Numerical results

The analytical results thus far may be compared with numerical results carried out for toric code lattices of small size in order to present an idea of the scale of the robustness of the code in the face of errors of small magnitude. For the sake of comparison numerical results have also been obtained for intrinsic errors of large magnitude.

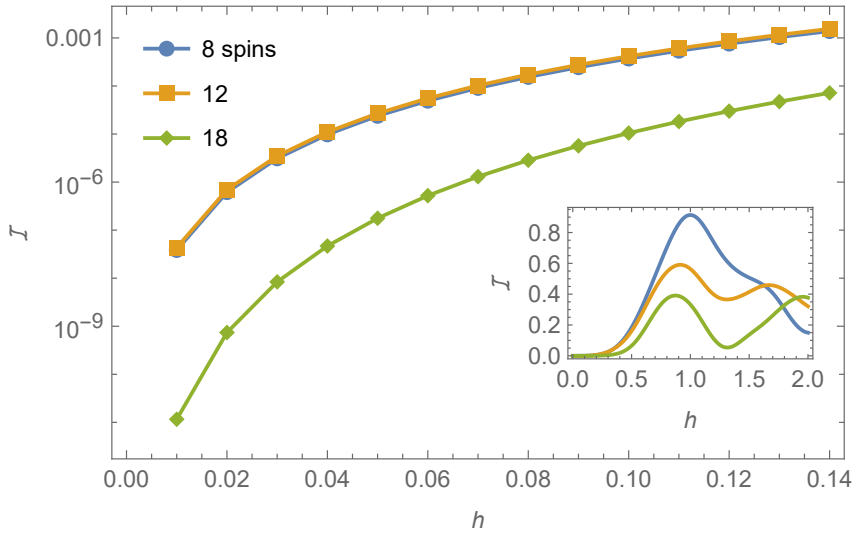

Figure 2.10: Infidelity between the the ground state of the toric code with all three orthogonal ground states after free evolution under the perturbed Hamiltonian $H_{\mathrm{TC}} + h\sum_j X_j$ for a time $2 \times \frac{\pi}{4\sqrt{2}}$ which is the time taken for anyon creation with the simplest control pulse. Free evolution infidelity for small magnitude h for the three lattice examples. A 3-by-2 lattice consisting of 12 spins gives demonstrably no advantage in terms of logical qubit protection compared to a 2-by-2 lattice of 8 spins.

2.5.1 8-qubit toric code

For the case of the smallest non-trivial lattice, the 2-by-2 plaquette case consisting of 8 spins, numerical results for free evolution of the ground state of the unperturbed Hamiltonian, assuming the same magnitude in error on every qubit, are shown in Fig. 2.10. A best fit curve for the numerical data assuming a small error gives an infidelity of $3.85469h^4$. This is an accurate numerical approximation given that the analytical form for the lowest order infidelity is $\frac{1}{4}h^4\left(1+\pi^2-\sqrt{2}\pi\sin\left(\sqrt{2}\pi\right)-\cos\left(\sqrt{2}\pi\right)\right) \approx 3.85469h^4$.

For the case of anyon-creation, infidelity after time 2τ in the presence of an unwanted error on every qubit, a numerical fit of $0.308425h^2$ is achieved. This is once again close to the exact figure for the lowest order infidelity $\frac{\pi^2}{32}h^2$.

2.5.2 12-qubit toric code

The next largest non-trivial toric code, the 3-by-2 lattice gives a best fit curve for the numerical data assuming a small error of $4.33636h^4$ infidelity. This is in concordance with the analytical result of $\frac{9}{32}h^4\left(1+\pi^2-\sqrt{2}\pi\sin\left(\sqrt{2}\pi\right)-\cos\left(\sqrt{2}\pi\right)\right) \approx 4.33642h^4$.

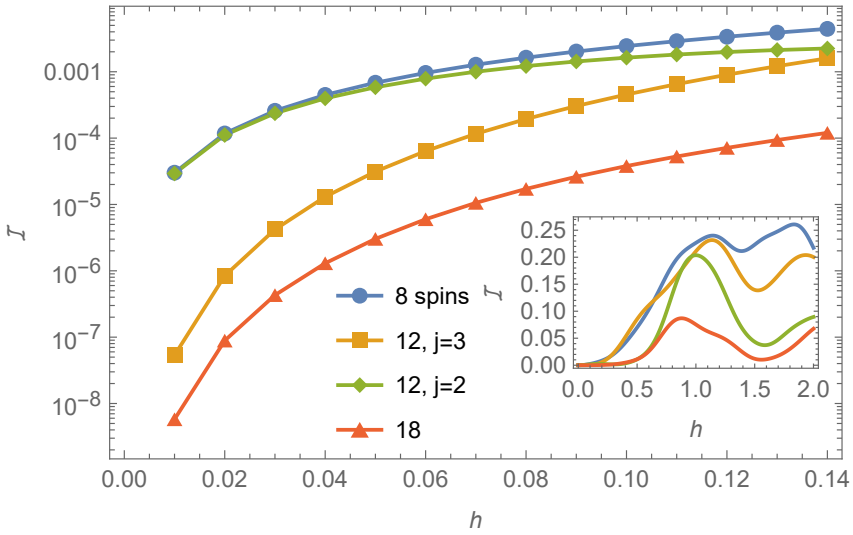

Figure 2.11: Graph showing the infidelity between the state $X_3 |g\rangle$ and orthogonal states of identical anyon configuration after evolution under the perturbed anyon-creation Hamiltonian $H_{\mathrm{TC}} + f(t)X_i + h\sum_j X_j$.

As expected this is $\frac{9}{8}$ times the same value for the 8-qubit lattice.

The numerical analysis for anyon-creation in the 12-qubit lattice requires further analysis than for the previous examples. For this lattice it matters greatly where the target qubit lies on the lattice. An anyon pair created by an operation on a spin qubit which can form a chain of 3 qubits for a possible logical X-gate will lead to infidelities which will be taken with states which require larger order errors to create them. As a result, the lowest order infidelity when creating an anyon pair on half of the qubits will be of the order h^4 while for the other half it will be of order h^2. In the particular example of the 3-by-2 lattice, the shorter side of the lattice is exactly 1 less than the longer side and so this additionally needs to be considered. Both examples are shown graphically in the numerical results. The respective lowest orders for the analytic results would be $\frac{\pi^2}{32}h^2$ and $(\Omega_1 + \Omega_2)h^4$ where

$$\Omega_1 = \frac{1}{128}\left(3\pi(8+3\pi) + 96 - 8\sqrt{2}(8+3\pi)\sin\left(\frac{\pi}{\sqrt{2}}\right) + 8(3\pi-4)\cos\left(\frac{\pi}{\sqrt{2}}\right)\right) \quad (2.71)$$

is the infidelity between the evolved state and the state equivalent to a logical gate on the

desired state where the logical gate is parallel to the desired anyon-pair. Moreover

$$\Omega_2 = \frac{1}{32}(25\pi^2 + 40\pi + 413 - \sqrt{2}(4+5\pi)\sin\left(\sqrt{2}\pi\right) \\ - 8\sqrt{2}(37+5\pi)\sin\left(\frac{\pi}{\sqrt{2}}\right) - 21\cos\left(\sqrt{2}\pi\right) + 8(15\pi - 8)\cos\left(\frac{\pi}{\sqrt{2}}\right)) \tag{2.72}$$

and this is the infidelity between the evolved state and the orthogonal states created using logical gates perpendicular to the desired anyon pair.

2.5.3 18-qubit toric code

The first substantial improvement in the infidelities over the simplest nontrivial toric code will be the 3-by-3 plaquette lattice consisting of 18 spin qubits. This is validated by the numerical results shown in Fig. 2.10. The infidelities are of a higher order (order h^6 for free evolution and h^4 for anyon creation). These are

$$\frac{81}{128}h^6\left(\pi^2 + 2 - 2\sqrt{2}\pi\sin\left(\sqrt{2}\pi\right) + \left(\pi^2 - 2\right)\cos\left(\sqrt{2}\pi\right)\right) \tag{2.73}$$

and an identical Ω_1 as for in the case of the 12-qubit lattice respectively.

2.6 Correctability of anyonic states

The toric code is forced to rely on an algorithm for error correction when it comes to anyon-pair annihilation that requires annihilating an anyon pair in the shortest path between them. As mentioned previously, this is not a optimal as it is impossible to locally distinguish between states of the same anyon configuration and so there is a reliance on the fact that it is marginally more difficult for an anyon-pair of a long string to materialise than for one of a shorter string. This then indicates that there will always be a nonzero probability of logical error during error correction/anyon-pair annihilation.

Considering the simplest possible desired eigenstate that is possible, namely a ground state of the toric code, and then examining error-correcting one single anyon-pair, it is

then possible to quantitatively classify which states will be corrected accurately using the shortest-path algorithm. A concrete example of an 8-by-8 lattice (128 qubits) is described below from which a generalisation is sought.

In the 128-qubit lattice example (see Fig. 2.12), any anyon-pair that is up to 3 qubit lengths long, that is, an anyon-pair that would be created through operations on three successive qubits, will always be corrected accurately, for there are no alternative paths between two anyons that could be shorter.

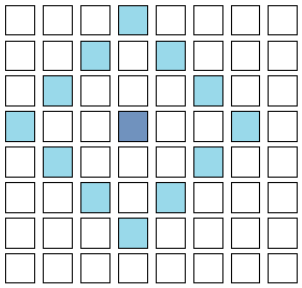

Figure 2.12: An 8-by-8 lattice showing all the possible locations of an anyon corresponding to a being in a pair with the central (darker blue) anyon. There are no alternate paths for any anyon which are shorter than 3 qubits and so all 12 states are completely correctable. There are 8^2 different possible positions for the central anyon, a number which must be halved to take into account the double counting of anyon pairs.

In general for a lattice of size n-by-n an anyon pair of qubit length all paths of length up to $\lceil \frac{n}{2} - 1 \rceil$ are completely correctable. The total number of anyon pairs possible then equals this number multiplied by half the total number of plaquettes, to account for counting each pair twice. In the concrete example this amounts to 32 multiplied by 4 (for pairs of length 1) plus 8 (pairs of length 2) plus 12 (pairs of length 3) which is 768. The general formula for a lattice of n plaquettes by n plaquettes then is

$$N_{\min} = \frac{n^2}{2} \sum_{k=1}^{\lceil \frac{n}{2} - 1 \rceil} 4k \tag{2.74}$$

where $N_{\min}$ is the minimum number of completely correctable states.

Anyon-pairs of even longer length still include some configurations that are completely correctable and some which are half-correctable. The latter describes states that have two shortest possible paths of annihilation that are topologically distinct. For even lattices,

that is lattices of size $2k$-by-$2k$ there are still 4 states which are completely correctable in pairs of length $2k-2$. At pairs of length $n-1$ we have 4 which are half-correctable. This is graphically illustrated in Fig. 2.13. In these scenarios, the total addition of completely correctable states amounts to a doubling of the formula, making $N_{\max} = 2N_{\min}$.

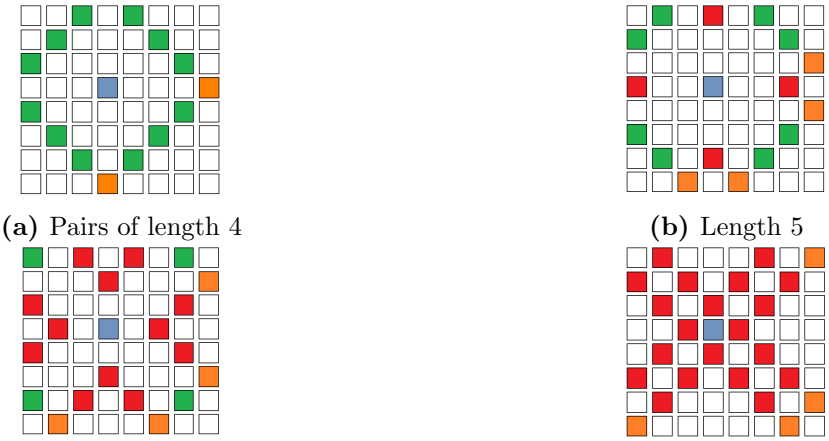

(a) Pairs of length 4 **(b)** Length 5

(c) Length 6 **(d)** Length 7

Figure 2.13: Illustration of correctable and uncorrectable states with varying lattice size. Key: Green - **accurate** correction, Orange - 50% accurate, Red - **inaccurate**. We can see that the anyon pairs of length $n-2$ have 4 each of 50% accuracy and 0% accuracy. For the pairs of length $n-1$ there are 4 at 50%.

This is true in general for all even lattices. For odd lattices (see Fig. 2.14) the only difference is that the remaining 50% accurate pairs of length $n-2$ and $n-1$ become completely correctable, as illustrated below. It turns out that all states are either completely correctable or completely uncorrectable (that is, there will be a logical error induced via the annihilation algorithm), meaning that the formula for $N_{\max}$ is the same.

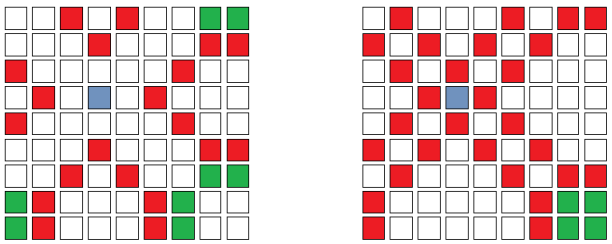

Figure 2.14: A 9-by-9 lattice where on the left are shown anyon-pairs that are 7-qubit lengths away and on the right 8-qubits. They each have 8 and 4 wholly correctable states respectively. Somewhat remarkably there are still some anyon configurations that are completely correctable using the shortest-path algorithm.

2.7 Imperfect state correction

All results described in previous sections of this chapter may thus be incorporated into a protocol for correcting errors, that is turning unwanted states into desired ones, in a way that is itself not necessarily done perfectly. A concrete example will be given for illustrative purposes, which may be readily generalised, of beginning with a ground state of the toric code and creating one anyon pair.

2.7.1 Protocol for anyon creation and error correction

1. Initialise the ground state of the toric code i.e. the anyonic vacuum state $|g_1\rangle$

2. Turn on time-dependent piecewise constant X-field pulse $f(t)$ acting on spin qubit j, with value of the pulse ϕ changing signs at times $\tau = \frac{\pi}{4\sqrt{1+(\frac{\phi}{2})^2}}$. The most efficient possible pulse to achieve this is with $\phi = \pm 2$ and $\tau = \frac{\pi}{4\sqrt{2}}$ with total time $T = 2\tau$.

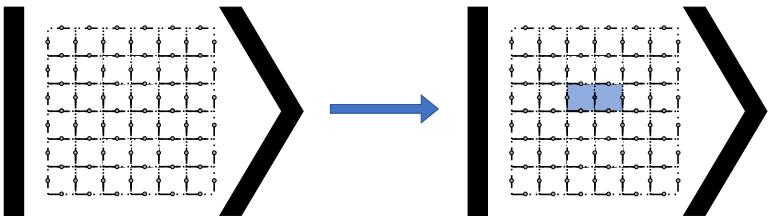

Figure 2.15: Desired evolution from $|g_1\rangle$ to $|X_j g_1\rangle$

3. The anyonic configuration should now be measured by measuring the required plaquette operators. If a measurement yields a -1 eigenvalue, this indicates the presence of an anyon on the corresponding plaquette. If anyon creation is carried out with some error ϵ in the pulse, either in pulse amplitude or in timing, then measuring the anyonic configuration after turning the pulse off will result in a collapse either to the desired state $|X_j g_1\rangle$ with high probability or back to the initial state with a probability of $O(\epsilon^2)$. If the state hasn't changed the process may be repeated.

4. With the presence of unwanted intrinsic errors present in the Hamiltonian, in the form of X-fields of magnitude h on every qubit, the state will have evolved to a superposition of every possible eigenstate of the lattice toric code. The probability of measuring the state to contain one extra anyon pair is $O(h^2)$, the probability of either two extra unwanted pairs or an unwanted anyon-pair of extended length is of the order $O(h^4)$ and so on.

   Of the unwanted states with one extra anyon pair, as the number of possible simple anyon-pairs on a lattice of plaquette size n-by-n and total qubit number $N = 2n^2$ is N itself, the number of unwanted states of the order h^2 is $N - 1$, ignoring the state where the error is also on the target qubit, whose infidelity is of the order h^4, corresponding to two Pauli operations. The six possible states that extend the desired anyon pair in an unwanted way will have a different coefficient of infidelity than that of the other $N - 7$.

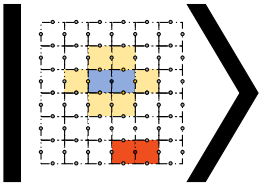

Figure 2.16: One out of a possible $N - 7$ possible unwanted anyon pairs shown in red, with the six possible states that could lengthen the target anyon pair shown in yellow.

5. If an unwanted anyonic configuration is measured, the error correction procedure is implemented which is identical to anyon creation. If there is an unwanted anyon pair on qubit k and a desired one on qubit j we evolve from $|X_k X_j g_1\rangle$ to $|X_j g_1\rangle$. The fidelity here will be $\mathcal{F} = 1 - \alpha h^2 + ...$ The overall total probability of arriving, after error correction to the final desired state is the probability of arriving at the correct state initially multiplied with the probability of the error correcting procedure being accurate.

To illustrate this protocol more clearly we may apply it to the concrete example of the 18-qubit toric code. If the ground state $|g_1\rangle$ is initialised and a pulse of magnitude

$|\phi| = 2$ is chosen with target spin is qubit 3 for the anyon-pair creation, two unitaries are required:

$$U_{\pm}(\boldsymbol{h}) = e^{-i\tau(H_{\mathrm{TC}} \pm 2X_3 + h\sum_k X_k)} \tag{2.75}$$

so that if $U_1 = U_-(0)$ and $U_2 = U_+(0)$ then the fidelity $|\langle X_3 g_1| U_2 U_1 |g_1\rangle|^2$ would be unity.

There are $N - 7 = 11$ states that could me arrived at through measuring the anyonic configuration after time 2τ in the presence of the error fields which correspond to an anyonic energy of $-N + 8 = -10$ rather than the desired $-N + 4 = -14$. An example of such a state is $|X_{18}X_3 g_1\rangle$ and the probability of measuring this state will be $h^2(\alpha\beta^* + \beta\alpha^* + |\alpha|^2 + |\beta|^2)$ to lowest order, where

$$\alpha = \langle X_{18}X_3 g_1| \frac{\partial U_+}{\partial h} U_- |g_1\rangle \tag{2.76}$$

$$\beta = \langle X_{18}X_3 g_1| U_+ \frac{\partial U_-}{\partial h} |g_1\rangle . \tag{2.77}$$

This evaluates overall to $\Omega_1 h^2 = \frac{1}{8}h^2\left(\cos\left(\sqrt{2}\pi\right) - 1\right)$.

There are a further six possible states such as $|X_2 X_3 g_1\rangle$ that there is a $O(h^2)$ probability of measuring that is equivalent to a state with unwanted lengthened anyon-string. Here the coefficient of h^2 evaluates to $\Omega_2 = \frac{1}{4}\left(2 - \sqrt{2}\sin\left(\frac{\pi}{\sqrt{2}}\right) - \cos\left(\frac{\pi}{\sqrt{2}}\right)\right)$. These states, which are the most likely of all the possible erroneous states to be measured, are all completely correctable, for after measurement, the shortest-path-annihilation algorithm will not lead to logical error.

The correction procedure is then implemented which, if we are evolving from $|X_{18}X_3 g_1\rangle$ then the lowest order probability of doing so correctly is approximately $1 - 11.3715h^2$. The second order coefficient is a sum of all the errors caused on individual qubits, some of which change the anyonic charge and some of which lengthen strings in an unwanted way. Similarly, if we evolve from $|X_2 X_3 g_1\rangle$ then the probability of correcting accurately is $\approx 1 - 6.78345h^2 + ...$ The total probability of arriving at the desired state after correction

is

$$\begin{aligned} & P\left(|g_1\rangle \to |X_3 g_1\rangle\right) \\ +11P\left(|g_1\rangle \to |X_{18}X_3 g_1\rangle\right) & P(|X_{18}X_3 g_1\rangle \to |X_3 g_1\rangle \,\big|\, |g_1\rangle \to |X_{18}X_3 g_1\rangle) \\ +6P\left(|g_1\rangle \to |X_2 X_3 g_1\rangle\right) & P(|X_2 X_3 g_1\rangle \to |X_3 g_1\rangle \,\big|\, |g_1\rangle \to |X_2 X_3 g_1\rangle) \end{aligned} \tag{2.78}$$

where $P(a\big|b)$ is the probability of a given b.

2.8 Summary

We have studied how to create and annihilate anyons in the toric code using time-dependent lattices of arbitrary magnitude as well as with a lower bound $\tau = \frac{\pi}{4}$ for time evolution. We have seen how timing and amplitude errors in the pulse alter the degree to which the desired anyonic state is achieved by an amount $O(\epsilon^2)$ in the error and if this is unsuccessful the original state is maintained. Using a step-by-step method of anyon-creation and string-extension, as well as possible annihilation, we can create strings of arbitrary length with repeated application of these pulses and culminate in a logical X-gate, while we see that errors will be compounded due to no interference terms appearing when pulse timing and/or amplitude errors are present. This compounding, to lowest order, can be considered as the sum of the individual errors.

We also studied the effects of intrinsic error terms in the Hamiltonian acting on all spins in the toric code lattice and we showed the effect this has on fidelities. We know that while larger lattices do not improve fidelity if a larger lattice means more qubits for errors to crop up on, we see that the probability of achieving 'uncorrectable' states that are equivalent to a logical error falls linearly with lattice width, and this was confirmed with numerical comparisons. Finally, we were able to quantify how often one would expect to find an anyon configuration that can be corrected properly while following the shortest-path annihilation algorithm for state correction.

Chapter 3

Non-abelian anyons in a honeycomb lattice

In this chapter we present our work regarding the use of quantum control to create non-abelian anyons in a spin lattice system, in such a way that is scalable for larger lattice sizes. The Kitaev honeycomb model is a notable example of a relatively simply defined system with non-trivial topological order [12, 45, 53]. The simplicity of the model's definition has led to multiple proposals in recent years for its experimental realisation [54, 55]. In this system, anyons manifest themselves as vortices introduced into the model which may be fused to create fermionic excitations corresponding to anyonic fusion rules known as Ising anyons [32, 56]. The exact fusion rules are given as

$$\sigma \times \sigma = 1 + \epsilon \tag{3.1}$$

$$\sigma \times \epsilon = \sigma \tag{3.2}$$

$$\epsilon \times \epsilon = 1 \tag{3.3}$$

where σ represents an anyon and ϵ represents a fermion so that Equation (3.1) is interpreted to mean that when two anyons are fused they may give rise to either a fermion or the anyonic vacuum.

Anyonic braiding itself and indeed any form of particles being interchanged is generally

assumed to be an adiabatic process [33, 57, 58] so that unwanted excitations may be safely suppressed. In practice, however, the restriction to adiabatic dynamics typically conflicts with the requirement to realise all operations on a time-scale that is short compared to the system's coherence time [59]. Quantum control has proven successful in speeding up adiabatic evolution in a wide range of scenarios [39, 40, 31, 41, 42] suggesting its suitability for anyon creation in topological systems. Common optimal control techniques, however, are limited in their applicability to the Kitaev honeycomb model. Due to the exponential scaling of composite quantum systems, numerical simulations of the time-dependent Kitaev honeycomb model are only possible for very small system sizes. Fermionisation of the Kitaev honeycomb model allows for improved scaling and solving larger systems but thus far this has generally been restricted to systems with time-independent Hamiltonians. The scope of this chapter is to use quantum control in applying fermionisation within the context of a time-dependent version of the model. This will demonstrate that optimal control does indeed provide access to faster-than-adiabatic anyon creation.

Section 1 of this chapter provides a brief overview of anyons in the Kitaev honeycomb model to setup the operators and terminology required for the control problem. Section 2 describes quantum control and pulse optimisation for anyon creation and sets up the key result on fermionisation, which is proven separately in Sections 3 and 4. Section 5 presents explicit numerical results of the optimal control problem defined. An overall summary of results and conclusions are presented in the final section.

3.1 Diagonalising the static Kitaev honeycomb model

We begin by reviewing one of the numerous methods of solving the static Kitaev honeycomb model [43, 60, 61, 62, 63]. This is followed by a demonstration of how vortex creation is implemented within the model [12, 14] and how this corresponds to creation of non-abelian anyons.

Although diagonalisation of the honeycomb model is not required for solving the time-dependent control problem we define later, we still outline its strategy, as the operators

and terminology introduced will also play a role in the time-dependent version. The honeycomb system takes its name from its hexagonal lattice geometry consisting of spin-1/2 particles located at the vertices of hexagonal plaquettes, as shown in Fig. 3.1. It is defined by the Hamiltonian

$$H = -\sum_{\{j,k\}\in N_2} J_s \sigma_j^s \sigma_k^s - K \sum_{\{j,k,l\}\in N_3} \sigma_j^x \sigma_k^y \sigma_l^z, \tag{3.4}$$

where N_2 correspond to honeycomb edges and N_3 are certain triplets of spins defined in a particular way. There are three types of two-body nearest neighbour Pauli interactions $s = x, y, z$ determined by the position of the edge in the lattice, highlighted in three colours in Fig. 3.1. The three-body terms act within each hexagonal plaquette in the following way: three adjacent spins contribute to a three-body interaction term with the middle spin interacting through the Pauli operator corresponding to the link pointing outwards from the plaquette, while each of the two remaining spins interact through the Pauli operator corresponding to their link to the middle spin. For example in the plaquette highlighted in Fig. 3.1, one of the three-body interaction terms would be $\sigma_1^y \sigma_2^x \sigma_3^z$, with 5 similar terms following clockwise along the hexagonal plaquette. While the two-body part of the Hamiltonian allows for the model to be solved by a process of Majorana fermionisation, the three-body part preserves the solvability of the model while also breaking time-reversal symmetry and it consequently gives the system non-trivial topological order [12].

For every hexagonal plaquette, a corresponding plaquette operator W_p may be defined which acts on every spin with the Pauli operator of the outward pointing interaction, so that for example on the numbered grey plaquette in Fig. 3.1 we have $W_p = \sigma_1^z \sigma_2^x \sigma_3^y \sigma_4^z \sigma_5^x \sigma_6^y$. Each plaquette operator squares to the identity so that its eigenvalues adopt the values ± 1 only. Since the plaquette operators all commute with the Hamiltonian and with one another, the system Hilbert space is naturally partitioned into simultaneous eigenspaces of all plaquette operators. Negative plaquette eigenstates are known as vortices and by a well known theorem [64] it is known that the ground state eigenspace is in the no-vortex sector [12]. Different vortex sectors relate to the presence of anyons localised at

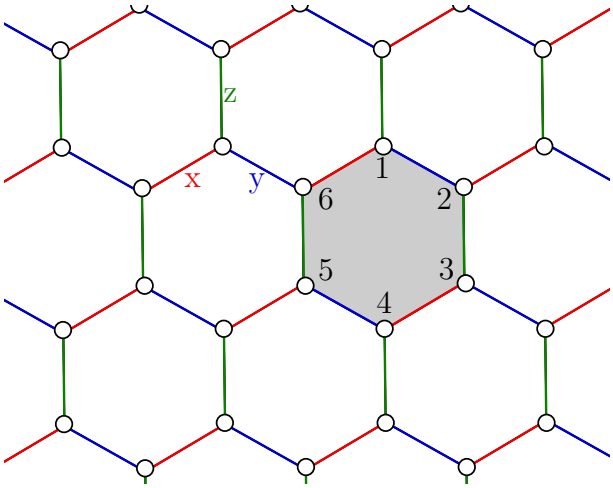

Figure 3.1: A honeycomb lattice showing the three kinds of interactions between neighbouring spins which are on the vertices of hexagonal plaquettes. Red, blue and green links indicate $\sigma^x\sigma^x$, $\sigma^y\sigma^y$ and $\sigma^z\sigma^z$ interactions respectively. The hexagonal plaquette operators correspond to many conserved quantities in the system. A generic plaquette whose spin sites have been numbered 1 to 6 is highlighted in grey.

the respective vortex plaquettes.

While solving the system remains an intractable exponential problem even after restriction to one vortex sector, a mapping of the problem into a Majorana fermionic Hamiltonian provides a pathway towards diagonalisation. The mapped Majorana fermionic Hamiltonian is defined by replacing spin qubit sites j with two fermionic sites and their corresponding creation operators $a^\dagger_{j,1}$ and $a^\dagger_{j,2}$. For each site j, the real and imaginary parts of the two fermionic modes constitute a total of four Majorana modes per site. The Majorana creation/annihilation operators are defined

$$\begin{aligned} b^x_j &= a_{j,1} + a^\dagger_{j,1}, \quad b^y_j = \frac{1}{i}(a_{j,1} - a^\dagger_{j,1}), \\ b^z_j &= a_{j,2} + a^\dagger_{j,2}, \quad c_j = \frac{1}{i}(a_{j,2} - a^\dagger_{j,2}). \end{aligned} \tag{3.5}$$

Since with this mapping the Hilbert space is enlarged, a projection is required to obtain vectors that correspond to states in the original Hilbert space of the honeycomb model. This requires the stabiliser projector [12, 43]

$$P_D = \prod_j^N \left(\frac{1 + D_j}{2}\right) \tag{3.6}$$

with $D_j = b_j^x b_j^y b_j^z c_j$.

The newly mapped Hamiltonian

$$H_f = \frac{iJ}{2} \sum_{\{j,k\} \in N_2} \hat{u}_{jk} c_j c_k + \frac{iK}{2} \sum_{\{j,l\},\{k,l\} \in N_2} \hat{u}_{jl} \hat{u}_{kl} c_j c_k, \tag{3.7}$$

is defined in terms of Majorana operators where we may also define link operators $\hat{u}_{jk} = ib_j^s b_k^s$ in a system of L total links and N spins.

The eigenvalues ± 1 of link operators allow for further partitioning of each vortex sector into link sectors. To this end, we can define a corresponding link sector projector

$$P_u = \prod_{\{j,k\} \in N_2}^{L} \frac{1 + u_{jk} \hat{u}_{jk}}{2}, \tag{3.8}$$

which amounts to choosing a tuple of link eigenvalues $u_{jk} \in \{\pm 1\}$.

Picking a certain link sector corresponds to fixing a gauge for a specific vortex sector and leads to a quadratic fermionic Hamiltonian $P_u H_f P_u$ that is easily diagonalised [65]. The trivial gauge would consist of setting all link eigenvalues to $u_{jk} = 1$, alongside the constraints imposed by their antisymmetry $\hat{u}_{jk} = -\hat{u}_{kj}$. This amounts to defining an orientation which for concrete purposes we define as follows: a positive orientation on an x-link is directed from the bottom-left qubit to the top-right one (j to k), for a y-link it is directed from the bottom-right to the top-left, and for a z-link it is directed from top to bottom.

The Hamiltonian becomes diagonal in a certain quasiparticle basis $H = \sum_{\omega > 0} \omega_j b_j^\dagger b_j - E_g$ and the ground state is the quasiparticle vacuum state. As previously stated, for physical states of the original Hamiltonian, the states will need to be projected; thus eigenstates of the spin Hamiltonian $|\Psi\rangle$ are related to eigenstates of the quadratic fermionic Hamiltonian $|\psi\rangle$ by

$$|\Psi\rangle = P_D P_u |\psi\rangle . \tag{3.9}$$

The energy gap in the system corresponding to the vortex energy δ is simply the difference in ground state energy E_g between differing vortex sectors. In general this is the energy gap between pairs of vortices but in exceptional examples, such as with the single plaquette lattice, this gap corresponds to a single vortex.

3.2 Anyon creation as an optimal control problem

Let us first describe the usual adiabatic approach. Vortex creation is implemented in terms of the time-dependent Hamiltonian

$$H(t) = H + \frac{t}{T} H^{j,k}_{\text{control}}, \tag{3.10}$$

comprised of the original honeycomb Hamiltonian as a drift combined with a control Hamiltonian

$$H^{j,k}_{\text{control}} = 2J_{jk}\sigma^s_j\sigma^s_k + 2K \sum_{j,k\in\{a,b,c\}} \sigma^x_a\sigma^y_b\sigma^z_c. \tag{3.11}$$

where $\{a, b, c\}$ is in N_3. This amounts to gradually reversing the sign of a specific s-link, as well as the sign of the nearby three-way interactions, using a linear time-dependence, with steepness and therefore adiabaticity determined by the duration T of the adiabatic protocol. As we will see in the numerical examples, T needs to be very large to obtain a good fidelity.

We now want to set up anyon creation as an optimal control problem in the hope that we can obtain similar fidelities in much shorter times compared to the adiabatic evolution. To this end, we generalise the time-dependence of Eq. (3.10) as

$$H(t) = H + f(t)H^{j,k}_{\text{control}}, \tag{3.12}$$

where $f(t)$ is the *ramp function* defined such that $f(0) = 0$ at the initial point in time $t = 0$ and such that $f(T) = 1$ at the final point in time $t = T$. Typically, $f(t)$ is assumed

to be piecewise smooth or piecewise constant.

A typical figure of merit to be maximised is the state fidelity $\mathcal{F}$ defined in terms of an initial state $|\Phi_0\rangle$, the propagator $U[f(t), T]$ induced by the time-dependent Hamiltonian $H(t)$ and a target state that is meant to be created. In the present case, the initial state $|\Phi_0\rangle$ would usually be the ground state of the honeycomb model whereas the target state $|\Phi_{\text{target}}\rangle$ is a state with an additional vortex-pair created.

While optimising for such a state fidelity is a generally successful approach, it has two flaws when it comes to the honeycomb model. Since topological stability only arises for large lattice size, any practical application of the honeycomb model requires a vast number of qubits. Evaluating the time-evolution operator therefore requires numerics in exponentially large spaces. Secondly, even if the ground state is solvable analytically in the free fermion picture, we would have to translate it back into the larger spin picture to evaluate $\mathcal{F}$, which is again exponentially hard. In the following, we will resolve both problems to obtain a scalable optimisation method.

3.2.1 Time-dependent fermionic picture

Let us first describe the time-independent case. In the fermionic picture, the quadratic Majorana Hamiltonian can be written in the most general form with a matrix J_{jk} that incorporates all interaction factors J as $H = \frac{i}{2}\sum_{jk} J_{jk} c_j c_k$. When written in terms of full fermionic creation and annihilation operators this is:

$$H = \frac{1}{2}\alpha^\dagger M \alpha \tag{3.13}$$

where $\alpha = (a_1, \ldots, a_N, a_1^\dagger, \ldots, a_N^\dagger)^{\mathrm{T}}$ is a vector of annihilation and creation operators (corresponding to the Majoranas defined in Eq. (3.5)) and the Hermitian matrix M

$$M = \begin{pmatrix} \mu & \nu \\ -\nu^* & -\mu^* \end{pmatrix} \tag{3.14}$$

may be defined in terms of a Hermitian matrix μ and an antisymmetric matrix ν. A canonical transformation T can then be found so that $TMT^{-1} = \mathrm{diag}\{\omega, -\omega\}$ where ω is a diagonal $2N$-by-$2N$ matrix. This allows for the Hamiltonian to be diagonalised in terms of quasiparticle modes [65].

We now consider how, in the fermionic picture, we may calculate the fidelity between a state evolved from an initialised state by a *time-dependent Hamiltonian* towards a target state. To this end, we write a ground state of H as $|\Phi_0\rangle \equiv A\,|\mathrm{vac}\rangle$, with the vacuum state $|\mathrm{vac}\rangle$ satisfying the relation $a_j\,|\mathrm{vac}\rangle = 0\ \forall j$. The operator A is some appropriately chosen function of creation and annihilation operators. In the following section, we show that the state fidelity in the fermionic picture is given by

$$\mathcal{F}(t) = |\,\langle\Phi_{\mathrm{target}}|\,kP_DP_u\;V[f(t),t]A\,|\mathrm{vac}\rangle\,|^2 \tag{3.15}$$

$$= |\,\langle\Phi_{\mathrm{target}}|\,kP_DP_uA(t)V[f(t),t]\,|\mathrm{vac}\rangle\,|^2. \tag{3.16}$$

Here the projector P_u is given by Eq. (3.8), $V[f(t),t]$ is the evolution operator corresponding to the quadratic Hamiltonian $P_uH(t)P_u$ and P_D is given by Eq. (3.6), while k is a real number which depends on the specific lattice (see the following section for specific examples). $A(t)$ is a Heisenberg picture operator $A(t) \equiv V[f(t),t]AV[f(t),t]^\dagger$.

In analogy to Eqs (3.13) and (3.14) it is useful to decompose $P_uH(t)P_u$ as

$$P_uH(t)P_u = P_u\frac{1}{2}\alpha^\dagger M(t)\alpha \tag{3.17}$$

Since A depends on annihilation and creation operators, we may write it as $A(\alpha)$. It can then be shown [65] that

$$V[f(t),t]A(\alpha)V^\dagger(t) = A(W[f(t),t]\alpha) \tag{3.18}$$

where $W(t)$ is the $2N$-by-$2N$ the time-ordered product solving the differential equation

$$\dot{W}[f(t),t] = iM[f(t)]W[f(t),t]. \tag{3.19}$$

This solves the problem of an exponentially sized evolution operator, as $W(t)$ scales linearly in the system size. We will refer to calculations in this picture as the Heisenberg picture, since it is directly obtained from the Heisenberg equations of motions of α. However, the problem of expressing the target and initial state in the spin picture remains. This will be tackled next.

3.2.2 Heisenberg fidelity as optimisation target

We have seen that the evolution is fully determined by the Heisenberg picture of the quadratic Hamiltonian. If we knew a good target evolution, rather than target state, we could therefore free ourselves from the state picture and obtain all quantities directly in the Heisenberg picture. The key idea here is to get back to the adiabatic evolution to find such good evolution. We phrase such evolution directly in the Heisenberg picture. To this end, let W_{ad} be the solution of Eq. (3.19) for the adiabatic ramp Eq. (3.10) with some suitably large duration T_{ad}. This can be computed efficiently without having to refer to states. We define a corresponding Heisenberg fidelity

$$\mathcal{F}_H = \frac{1}{2N}\left|\mathrm{Tr}\Big(W_{\mathrm{ad}}^\dagger W[f(t),T]\Big)\right| \tag{3.20}$$

This quantity obtains its maximum 1 if and only if the evolutions match up to a phase and it can be used for efficient numerical optimisation. In Section 4 of this chapter, we explicitly demonstrate that

$$1-\mathcal{F}_H \geq \frac{1}{32N^3}\left(1-\sqrt{\mathcal{F}}\right). \tag{3.21}$$

This shows that $\mathcal{F}_H$ is a good surrogate for $\mathcal{F}$ and may be optimised instead.

3.3 Dynamics of the time-dependent Hamiltonian in the fermionic picture

Previous work on the Kitaev honeycomb model has primarily been focused on time-independent Hamiltonians, yet for quantum control we require time-dependent Hamiltonians. Examples of such investigations of a time-dependent Kitaev honeycomb model have included those focused on periodic driving [66, 67] which have used Floquet theory, allowing for periodic driving to be mapped to an effectively time-independent system [68]. Other studies have used Jordan-Wigner transformations without projections to look at specific time-dependent behaviour such as the Kitaev honeycomb model with a quenched magnetic field [69]. While useful, these studies are not sufficient for our purposes of using general time-dependence in the regular honeycomb model.

In this section we show that in regular lattices with open, periodic or half-periodic boundary conditions, the fermionisation procedure with projections is still possible in the time-dependent case.

First let us recall the projections onto a link sector u

$$P_u = \prod_{\{jk\}}^{L} \frac{1 + u_{jk}\hat{u}_{jk}}{2}, \tag{3.22}$$

defined by an L-tuple of link eigenvalues $u_{jk} \in \{\pm 1\}$; the projector onto a vortex sector w

$$P_w = \prod_{j}^{P} \frac{1 + w_j \hat{w}_j}{2} \tag{3.23}$$

defined by a P-tuple of plaquette eigenvalues $w_j \in \{\pm 1\}$; and the projector onto the physical subspace of the fermionic space given by

$$P_D = \prod_{j}^{N} \frac{1 + D_j}{2} \ , \ \text{with} \ \ D_j = b_j^x b_j^y b_j^z c_j. \tag{3.24}$$

Since

$$\hat{w}_j = \prod_{\{k,l\}\in w_\beta} \hat{u}_{kl}, \tag{3.25}$$

P_u and P_w commute, and moreover w is fully determined by u. We denote this relationship as $w = \omega(u)$ and thus have $P_w P_u = \delta_{w,\omega(u)} P_u$ and

$$P_w = P_w \sum_u P_u = \sum_{u:\omega(u)=w} P_u. \tag{3.26}$$

P_w commutes with P_D, P_u and the time-dependent fermionic Hamiltonian $H_f(t)$, so it will suffice to restrict ourselves to a single plaquette sector w. While P_D is the projection that determines physicality, P_u will turn the fermionised Hamiltonian into a quadratic (and thereby easy to solve) one. A difficulty arises from the fact that P_D *does not* commute with P_u. We can however find another useful relationship between these projectors. Let N be the number of qubits of the original spin lattice and $\{\Gamma_k | k = 1, \cdots, 2^N\}$ be the set of all possible products of stabiliser operators D_i on the qubits, without repetition, where we take an arbitrary but fixed order. For our fixed w consider the corresponding pre-image $\omega^{-1}(w)$ of link sectors. We define an equivalence relationship $\sim$ on this set by $u \sim v :\Leftrightarrow \exists k : P_u = \Gamma_k P_v \Gamma_k$. Let κ be the number of equivalence classes. Let us choose an arbitrary but fixed set of representatives $u_1, \ldots, u_\kappa$, one from each equivalence class, and define $P_{\bar{u}} = \sum_{i=1}^{\kappa} P_{u_i}$.

Upon expanding P_D in terms of stabilisers, we obtain

$$P_D P_{\bar{u}} P_D = \frac{1}{2^N} P_D \sum_{i=1}^{\kappa} \sum_{k=1}^{2^N} \Gamma_k P_{u_i} \Gamma_k. \tag{3.27}$$

To understand the right hand side better, we make a counting argument. Firstly, it follows from the anticommutation relations between link operators $\hat{u}_{jk}$ and the D_j stabiliser

operators,

$$\{D_j, \hat{u}_{kl}\} = 0 \qquad j = k \text{ or } j = l \tag{3.28}$$

$$[D_j, \hat{u}_{kl}] = 0 \qquad j \neq k \text{ and } j \neq l, \tag{3.29}$$

that the $\Gamma_k P_{u_i} \Gamma_k$ are again link projectors. Since we sum over all Γ_k and by definition of the equivalence classes, we know that every $u \in \omega^{-1}(w)$ appears at least once on the right hand side, and that there are no overlaps between the classes of fixed i. Furthermore the equality $\Gamma P_u \Gamma = P_u$ holds if and only if $\Gamma = 1$ or $\Gamma = \prod_i D_i$. Therefore, there are 2^{N-1} distinct projectors for each i. It follows that

$$P_D P_{\bar{u}} P_D = \frac{1}{2^N} 2 P_D \sum_{u:\omega(u)=w} P_u = \frac{1}{2^{N-1}} P_D P_w. \tag{3.30}$$

From the commutativity relations $[H_f(t), P_D] = 0$ and $[H_f(t), P_{\bar{u}}] = 0$ it also follows that

$$V(t) P_D P_w = 2^{N-1} V P_D P_{\bar{u}} P_D = 2^{N-1} P_D P_{\bar{u}} V(t) P_{\bar{u}} P_D, \tag{3.31}$$

where $V(t)$ is the propagator corresponding to $H_f(t)$ and we have used that $P^2 = P$ for all projectors. Hence, the evolution can be computed in the subspace $P_{\bar{u}}$. To conclude the argument, we need to know the value of κ, as this determines how many link sectors we need to consider. As long as κ is not exponential, we can efficiently simulate the dynamics.

To this end, we need another counting argument. To simplify the analysis, we only consider three different regular lattice types dubbed open (o), periodic (p) and half-periodic (h), and find their corresponding values of κ. To do this, we first find relationships for the number of link operators L, the number of plaquettes P, and the number of qubits N for the various lattices. Simple but rather tedious counting of such regular lattices shows that $L - P = N - 1$ in the open case and $L - P = N$ in the other two cases. Next, compute the size of $\omega^{-1}(w)$. We show in the lemma below that $|\omega^{-1}(w)|_{o,h} = 2^{L-P}$ and $|\omega^{-1}(w)|_p = 2^{L-P+1}$. Since each equivalence class has exactly 2^{N-1} elements, we have to

have

$$|\omega^{-1}(w)| = 2^{N-1}\kappa$$

such that $\kappa_o = 1$, $\kappa_h = 2$,$\kappa_p = 4$.

Lemma 3.3.1. *For all* w, $|\omega^{-1}(w)|_{o,h} = 2^{L-P}$ *and* $|\omega^{-1}(w)|_p = 2^{L-P+1}$.

Proof. Consider first the case of a lattice with open boundary conditions. Since there are no boundary constraints, all possible configuration of plaquette eigenvalues $\{\Lambda_j\}$ are possible, and

$$|\{\Lambda_j\}|_o = 2^P. \tag{3.32}$$

From the above, for each u, we can find 2^{N-1} other v with $\omega(v) = \omega(u)$ by conjugation with Γ_k. Since in the open lattice the number of qubits N follows the relation $N - 1 = L - P$, one can conclude that for each w, the inequality $|\omega^{-1}(w)|_o \geq 2^{L-P}$ holds. Since there are by definition 2^L different link sectors, we have

$$2^L = \sum_w |\omega^{-1}(w)|_o \geq 2^{L-P}2^P = 2^L \tag{3.33}$$

so equality holds and the statement follows.

Next, consider a lattice with full periodic boundary conditions. Any link eigenvalue change leads necessarily to exactly two plaquette eigenvalues being flipped. Therefore only even numbers of vortices may ever be present, and the number of plaquette eigenvalue configurations is

$$|\{\Lambda_j\}|_p = 2^{P-1}. \tag{3.34}$$

Now, for each u, we can find 2^{N-1} other v with $\omega(v) = \omega(u)$ by conjugation with Γ_k, but for each of these we can find 4 inequivalent link sectors. Since $L - P = N$ for periodic

boundaries, we obtain

$$2^L = \sum_w |\omega^{-1}(w)|_p \geq 4 \times 2^{L-P-1} 2^{P-1} = 2^L \tag{3.35}$$

and the statement follows again.

Finally, in the half-periodic case we only have 2 inequivalent link sectors, but $|\{\Lambda_j\}|_p = 2^P$ is twice as big as in the periodic case, and the same counting argument holds.

□

3.3.1 Inequivalent sectors: Periodic boundary conditions

We now consider the case of a lattice with periodic boundary conditions in both the a and b directions (that is, both vertically and horizontally as on a torus). We consider the no-vortex sector and and any arbitrary link sector associated with it which we call P_{u_0}. We have already shown that P_{u_0} is gauge equivalent, that is, equivalent up to conjugation by Γ_k operators, with 2^{N-1} link sector projectors.

Acting on a non-zero eigenstate of P_{u_0} with any stabiliser operator D_j will change three link sector eigenvalues at a time, due to D_j overlapping with the three types of link that contain spin site j, the same is therefore also true of Γ_k operators. On the other hand acting on spin sites with a Pauli operator such as Z_j, which in the fermionic picture is

$$\tilde{Z}_j = ib_j^z c_j \tag{3.36}$$

will flip the sign of only the z-link corresponding to that site and no others. In general a Pauli operator $\tilde{\sigma}^\alpha$ will only flip the sign of the α-link containing spin site j. This is due to the fact that

$$\{\tilde{\sigma}_j, \hat{u}_{jk}\} = \{ib_j^\sigma c_j, ib_j^\sigma b_k^\sigma\} = 0 \tag{3.37}$$

$$[\tilde{\sigma}_j, \hat{u}_{kl}] = \left[ib_j^\sigma c_j, ib_k^\sigma b_l^\sigma\right] = 0, \quad j \notin \{k, l\}. \tag{3.38}$$

Thus we have that

$$\tilde{Z}_\alpha P_{u_j} = P_{u_k} \tilde{Z}_\alpha \tag{3.39}$$

and thus

$$P_{u_j} = \tilde{Z}_\alpha P_{u_k} \tilde{Z}_\alpha \tag{3.40}$$

where in general $\omega(u_j) \neq \omega(u_k)$.

Flipping a single link eigenvalue will change the vortex sector as a pair of vortices are introduced on adjacent plaquettes. Taking ζ to be an arbitrary product of $\tilde{Z}$ Pauli operators, then in order to have

$$P_{u_j} = \zeta P_{u_k} \zeta \tag{3.41}$$

such that $\omega(u_j)$ *does* equal $\omega(u_k)$, we require ζ to consist of a pair of link-flipping $\tilde{Z}$ operators for each plaquette.

In order to return to the no-vortex sector, vortices need to be annihilated and so the vortex string must form a closed loop. Algebraically speaking, while each $\tilde{\sigma}_j$ will commute with all overlapping and non-overlapping D_j operators, as

$$[\tilde{\sigma}_j, D_j] = \left[i b_j^\alpha c_j, b_j^x b_j^y b_j^z c_j \right] \tag{3.42}$$

$$= 0 \tag{3.43}$$

and

$$[\tilde{\sigma}_j, D_k] = \left[i b_j^\alpha c_j, b_k^x b_k^y b_k^z c_k \right] \tag{3.44}$$

$$= 0, \tag{3.45}$$

such Paulis will not commute with overlapping plaquette operators W_p as for a spin site

j, plaquette operators will act with Paulis $\tilde{X}$ or $\tilde{Y}$ and thus there is anticommutation.

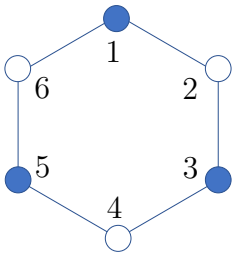

Figure 3.2: An example of lattice plaquette with six spins labelled. The plaquette operator for this is $W_p = Z_1X_2Y_3Z_4X_5Y_6$.

In order for there to be commutation with all plaquette operators, there needs to be $\tilde{Z}_j$ operators acting on two spin sites per plaquette. Following the labelling of spins in a plaquette in Fig. 3.2, clearly

$$[Z_6, W_p] = [Z_6, Z_1X_2Y_3Z_4X_5Y_6] \neq 0 \tag{3.46}$$

but

$$[Z_6Z_2, W_p] = [Z_6Z_2, Z_1X_2Y_3Z_4X_5Y_6] = 0. \tag{3.47}$$

The simplest example of a product of $\tilde{Z}_j$ operators that commutes with all link operators is shown explicitly and schematically in Fig. 3.3b and Fig. 3.4b respectively.

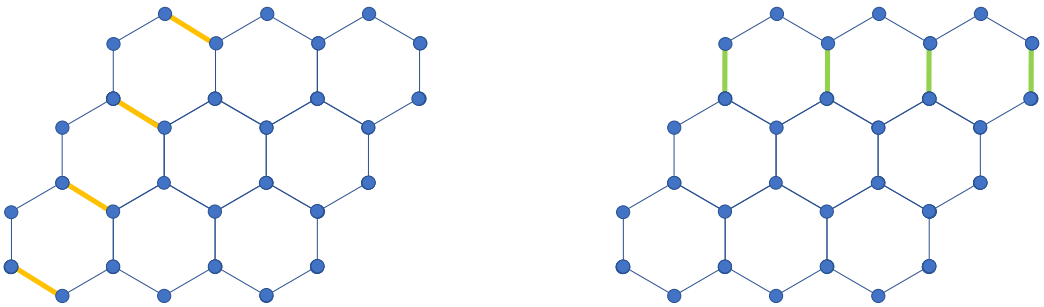

(a) **(b)**

Figure 3.3: Simple sets of y **(a)** and z **(b)** link flips that preserve the vortex sector while being gauge inequivalent to the trivial link sector.

Starting with link sector P_{u_0} and using only Γ_k operators, it is not possible to flip the sign of only a single row of z-links as in general the action of a D_j operator flips the sign

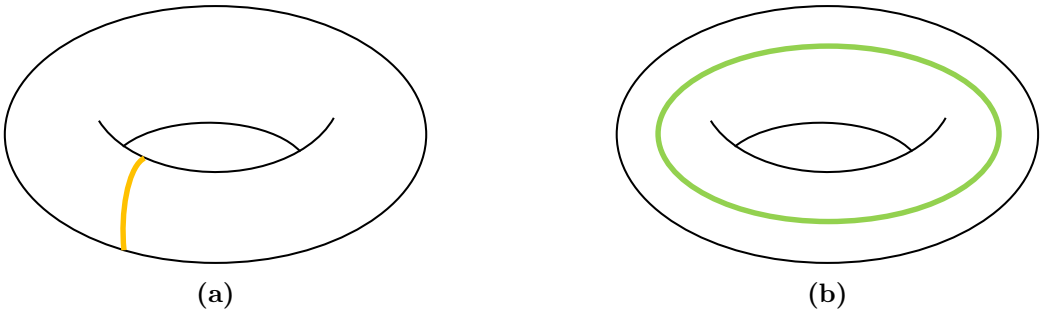

Figure 3.4: Topological interpretation of the set of y and z flips that preserve vortex sector but are gauge inequivalent to the trivial link sector which topologically amounts to no loop at all.

of all three types of link x, y and z. In order to keep all x and y links unflipped, products of D_j operators must act on the sites of all spins that correspond to those links, leaving at least a *pair* of rows with flipped eigenvalues on z-links, as demonstrated in Fig. 3.5.

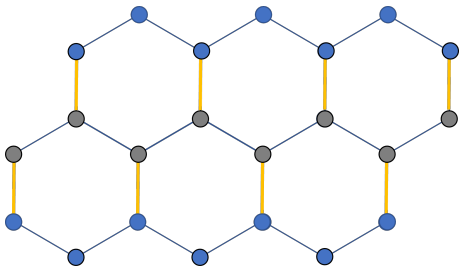

Figure 3.5: A lattice where the grey spin sites have been acted on with D_j operators and link eigenvalues on yellow links have been flipped. It is not possible to flip only a single line of z-links using Γ_k operators alone.

We therefore have found another link sector P_{u_z} whose corresponding vortex sector is the no-vortex sector which cannot be reached from P_{u_0} by conjugation with Γ_k operators. Algebraically this can be represented by

$$\nexists\, \Gamma_k \text{ such that } \Gamma_k P_{u_0} \Gamma_k = P_{u_z} \tag{3.48}$$

where

$$P_{u_z} := \zeta P_{u_0} \zeta \tag{3.49}$$

and ζ is a horizontal, topologically closed loop of Pauli $\tilde{Z}$ operators. This is because when commuting ζ through P_{u_0}, only the signs of a row of z-link eigenvalues are changed. If

we call this row of links ρ then

$$\zeta P_{u_0} = \zeta \prod_{jk} \frac{1 + u^{\alpha}_{jk} \hat{u}^{\alpha}_{jk}}{2} \tag{3.50}$$

$$= \prod_{\alpha=z, jk \in \rho} \frac{1 - u^{\alpha}_{jk} \hat{u}^{\alpha}_{jk}}{2} \prod_{\text{etc.}} \frac{1 + u^{\alpha}_{jk} \hat{u}^{\alpha}_{jk}}{2} \zeta \tag{3.51}$$

$$= P_{u_k} \zeta. \tag{3.52}$$

However with Γ_k operators, in order to commute them through P_{u_0} and have only z-link eigenvalues flipped, this requires a Γ_k consisting of D_j operators acting on a row of spin sites in the manner of Fig. 3.5 and thus a minimum of two rows of z-link eigenvalues are flipped. Thus for all Γ_k

$$\Gamma_k P_{u_0} \Gamma_k \neq \zeta P_{u_0} \zeta. \tag{3.53}$$

We can now repeat the above process, with the same reasoning, starting with the link sector P_{u_z} rather than P_{u_0}, but this time with Pauli $\tilde{Y}$ operators to flip links as shown in Fig. 3.3a and Fig. 3.4a. This would have given another link sector unreachable via actions of Γ_k operators, just as P_{u_z} was unreachable from P_{u_0}. This would have corresponded to flipping link signs vertically rather than horizontally. Pauli $\tilde{X}$ operators can be written, up to a phase, as simply products of $\tilde{Z}$ and $\tilde{Y}$ Paulis, thus no new link sectors can be found by use of the above operations with $\tilde{X}$ Paulis. Therefore for a lattice defined by a plaquettes per row and made up of b rows, if we define

$$\zeta = \tilde{Z}_{j_1} ... \tilde{Z}_{j_a} \tag{3.54}$$

$$\chi = \tilde{Y}_{j_1} ... \tilde{Y}_{j_b} \tag{3.55}$$

then the four link sector operators

$$P_{u_0}, \tag{3.56}$$

$$P_{u_z} = \zeta P_{u_0} \zeta, \tag{3.57}$$

$$P_{u_y} = \chi P_{u_0} \chi, \tag{3.58}$$

$$P_{u_x} = \zeta \chi P_{u_0} \chi \zeta \tag{3.59}$$

each define gauge-inequivalent link sectors in a particular vortex sector.

Inequivalent sectors: Half-periodic boundary conditions

For a system with half-periodic boundary conditions, depending on whether periodicity is in the horizontal or vertical direction, only a single row or 'column' of flipped signs would be required to find a link sector projector not reachable from P_{u_0} by actions of Γ_k operators. There would therefore be two sets of 2^{N-1} link sector projectors corresponding to two equivalence classes in each vortex sector. Accounting for all 2^P vortex sectors there would be a total of

$$2^P(2 \times 2^{N-1}) = 2^{N+P} = 2^L \tag{3.60}$$

and so we have accounted for all link sectors.

3.4 Proof of matrix-infidelity state-infidelity bound

This section contains the proof of Eq (3.21) which relates state infidelity and Heisenberg infidelity. State infidelity is defined between two states with differing dynamics U_j $(j = 1, 2)$ applied to an initial spin state $|\Psi_I\rangle$. These dynamics are induced by spin Hamiltonians $H_{s,j}$ whose counterparts in the quadratic Majorana fermionic picture $\tilde{H}_{\text{ferm},j} = \alpha^\dagger M_j \alpha$ (see Section. 3.1) define orthogonal matrices $\mathcal{O}_j$ generated by the Hermitian matrices M_j in a relation which satisfies the differential equation $\dot{\mathcal{O}}_j = iM_j\mathcal{O}_j$.

The relation to be proven reads

$$\mathcal{I}_H(\mathcal{O}_1, \mathcal{O}_2) \geq \frac{1}{4d^3}\left(1 - \sqrt{\mathcal{F}_s(\Psi_1, \Psi_2)}\right) \tag{3.61}$$

with the state fidelity

$$\mathcal{F}_s(\Psi_1, \Psi_2) \ = |\langle\Psi_1|\Psi_2\rangle|^2 \ = \left|\langle\Psi_I| U_2^\dagger U_1 |\Psi_I\rangle\right|^2, \tag{3.62}$$

and the Heisenberg infidelity $\mathcal{I}_H = 1 - \mathcal{F}_H$ with

$$\mathcal{F}_H(\mathcal{O}_1, \mathcal{O}_2) = \frac{1}{d}\left|\mathrm{Tr}\left(\mathcal{O}_1^\dagger \mathcal{O}_2\right)\right| \ , \tag{3.63}$$

and the matrix dimension d.

The full proof consists of Eq. (3.64) and the series of inequalities Eq. (3.65) to (3.67)

$$\begin{aligned}
\sqrt{2d}\sqrt{\mathcal{I}_H} &= \|\mathcal{O}_1 - \mathcal{O}_2\|_F && (3.64)\\
&\geq \frac{1}{2d}\|\Phi_{U_1} - \Phi_{U_2}\|_\diamond && (3.65)\\
&\geq \frac{1}{2d}\min_\varphi \|U_1 - e^{i\varphi}U_2\|_{\mathrm{op}} && (3.66)\\
&\geq \frac{1}{\sqrt{2}d}\sqrt{1 - \sqrt{\mathcal{F}_s}} && (3.67)
\end{aligned}$$

that will be discussed separately in the following subsections. Eq. (3.64) is expressed in terms of the Frobenius norm

$$\|A\|_F := \sqrt{\mathrm{Tr}(A^\dagger A)} \tag{3.68}$$

for any operator A. Eq. (3.65) is expressed in terms of the operator norm

$$\|A\|_{\mathrm{op}} := \sup\left\{\frac{\|Ax\|}{\|x\|} : x \in V^d \text{ with } x \neq 0\right\}. \tag{3.69}$$

The diamond norm for a quantum channel Φ in Eq. (3.66) is given by

$$\|\Phi\|_\diamond := \max_\rho \|(\Phi \otimes \mathbf{1})\rho\|_1 \tag{3.70}$$

where $\|\circ\|_1 = \mathrm{Tr}\sqrt{A^\dagger A}$ is the trace norm [70], and the maximisation is taken over all density matrices in a space of dimension which is larger compared to the size of the quantum channel Φ.

3.4.1 Norms and infidelity relations

Frobenius norm and infidelity relation (3.64)

The Frobenius norm of the difference between two orthogonal operators $\mathcal{O}_1$ and $\mathcal{O}_2$ reduces to

$$\|\mathcal{O}_1 - \mathcal{O}_2\|_F = \sqrt{2d - \mathrm{Tr}(\mathcal{O}_1^\mathrm{T}\mathcal{O}_2) - \mathrm{Tr}(\mathcal{O}_2^\mathrm{T}\mathcal{O}_1)} \tag{3.71}$$

$$= \sqrt{2d - 2\,\mathrm{Re}\{\mathrm{Tr}(\mathcal{O}_1^\mathrm{T}\mathcal{O}_2)\}}, \tag{3.72}$$

where d is the dimension of $\mathcal{O}_1$ and $\mathcal{O}_2$. It thus depends on the real part of $\mathrm{Tr}\big(\mathcal{O}_1^\mathrm{T}\mathcal{O}_2\big)$ and not on its absolute value, as is the case for $\mathcal{F}_H$. As we will show in the following, however, in the present case, the object $\mathrm{Tr}\big(\mathcal{O}_1^\mathrm{T}\mathcal{O}_2\big)$ is real and positive, so that Eq. (3.64) is indeed satisfied.

Proof that $\mathrm{Tr}\big(\mathcal{O}_1^\mathrm{T}\mathcal{O}_2\big)$ is real

The orthogonal matrices $\mathcal{O}_1$ and $\mathcal{O}_2$ satisfy the differential equation $\dot{\mathcal{O}}_j = iM_j\mathcal{O}_j$ with generally time-dependent generators iM_j. Since the M_j are purely imaginary, the generators iM_j are purely real. Together with the initial condition $\mathcal{O}_j(0) = \mathbf{1}$, such that $\mathcal{O}_j(0)$ is real, this implies that $\mathcal{O}_j(t)$ for $j = 1, 2$ is real for all times. Consequently the overlap $\mathrm{Tr}\big(\mathcal{O}_1^\mathrm{T}\mathcal{O}_2\big)$ is also real.

Proof that $\mathrm{Tr}\big(\mathcal{O}_1^{\mathrm{T}}\mathcal{O}_2\big)$ is non-negative

Since Majorana fermions move between only one of two pairs of fermionic sites per spin site, the full space that $\mathcal{O}_1$ and $\mathcal{O}_2$ act on, can be divided into two subspaces H_x and H_y of equal dimension $d/2$. Both $\mathcal{O}_1$ and $\mathcal{O}_2$ are given as a direct sum of the identity $\mathbf{1}$ in H_x and orthogonal operators $\tilde{\mathcal{O}}$ in H_y. The complete trace is thus given as the sum of the two traces $\mathrm{Tr}_x\,\mathbf{1}$ and $\mathrm{Tr}_y\,\tilde{\mathcal{O}}_1^{\mathrm{T}}\tilde{\mathcal{O}}_2$. The latter trace can also be expressed as the sum over the eigenvalues λ_j of $\tilde{\mathcal{O}}_1^{\mathrm{T}}\tilde{\mathcal{O}}_2$. This results in the relation

$$\mathrm{Tr}\big(\mathcal{O}_1^{\mathrm{T}}\mathcal{O}_2\big) = \mathrm{Tr}_x\,\mathbf{1} + \mathrm{Tr}_y\,\tilde{\mathcal{O}}_1^{\mathrm{T}}\tilde{\mathcal{O}}_2 = \frac{d}{2} + \sum_{j=1}^{\frac{d}{2}} \lambda_j \ . \tag{3.73}$$

Since the trace $\mathrm{Tr}\big(\mathcal{O}_1^{\mathrm{T}}\mathcal{O}_2\big)$ is purely real, the imaginary parts $\mathrm{Im}\,\lambda_j$ add up to zero. Because all the eigenvalues λ_j are phase factors, *i.e.* $\lambda_j = \exp(i\varphi_j)$ with φ_j real, the real parts of the λ_j satisfy the inequality $\mathrm{Re}\,\lambda_j \geq -1$, so that the relation

$$\mathrm{Tr}\big(\mathcal{O}_1^{\mathrm{T}}\mathcal{O}_2\big) = \frac{d}{2} + \sum_{j=1}^{\frac{d}{2}} \lambda_j \geq 0 \tag{3.74}$$

is indeed given.

First norm inequality, from (3.64) **to** (3.65)

It is well known that the Frobenius and operator matrix norms satisfy the inequality $\|A\|_F \geq \|A\|_{\mathrm{op}}$ [71]. For the present case, this implies the inequality

$$\|\mathcal{O}_1 - \mathcal{O}_2\|_F \geq \|\mathcal{O}_1 - \mathcal{O}_2\|_{\mathrm{op}} \ . \tag{3.75}$$

The following relation is also required

$$\|\mathcal{O}_1 - \mathcal{O}_2\|_{\mathrm{op}} \geq \frac{1}{2d}\|\Phi_{U_1} - \Phi_{U_2}\|_{\diamondsuit} \tag{3.76}$$

which is proven using methods of representation theory in Eq. (F1) in Ref. [72], wherein the fermionic matrices $\mathcal{O}$, which are of a size that grows linearly in the number of fermionic modes, are related to the quantum channels Φ_U of the full system dynamics using the diamond norm described previously. Combining the results in (3.75) and (3.76) yields the desired inequality.

Second norm inequality, from (3.65) **to** (3.66)

The required inequality

$$\|\Phi_{U_1} - \Phi_{U_2}\|_\diamond \geq \min_\varphi \|U_1 - e^{i\varphi} U_2\|_{\text{op}} \tag{3.77}$$

is proven in Eq. (2.1) in [73], using geometric arguments as well as Theorem 26 in [74].

Third norm inequality, from (3.66) **to** (3.67)

Following the definition of the operator norm in Eq. (3.69), the operator norm in Eq. (3.66) satisfies the inequality

$$\|U_1 - e^{i\varphi} U_2\|_{\text{op}} \geq \|(U_1 - e^{i\varphi} U_2)\,|\Psi\rangle\,\|_2 \tag{3.78}$$

for any state vector $|\Psi\rangle$ in the spin picture, and, as such, in particular for the initial state $|\Psi_I\rangle$ of the dynamics. That is, the inequality

$$\begin{aligned}
\|U_1 - e^{i\varphi} U_2\|_{\text{op}} &\geq \|\,|\Psi_1\rangle - e^{i\varphi}\,|\Psi_2\rangle\,\|_2 && (3.79)\\
&= \sqrt{(\langle\Psi_1| - e^{-i\varphi}\,\langle\Psi_2|)(|\Psi_1\rangle - e^{i\varphi}\,|\Psi_2\rangle)} && (3.80)\\
&= \sqrt{2 - e^{i\varphi}\,\langle\Psi_1|\Psi_2\rangle - e^{-i\varphi}\,\langle\Psi_2|\Psi_1\rangle} && (3.81)\\
&= \sqrt{2 - 2|\langle\Psi_1|\Psi_2\rangle|\cos(\varphi + \theta)} && (3.82)
\end{aligned}$$

holds, where the overlap of $|\Psi_1\rangle$ and $|\Psi_2\rangle$ can be defined in terms of state infidelity and a phase

$$\langle\Psi_1|\Psi_2\rangle = |\langle\Psi_1|\Psi_2\rangle|e^{i\theta} = \sqrt{\mathcal{F}_s}e^{i\theta}. \tag{3.83}$$

When Eq. (3.82) is minimised over all phases φ this gives the required result

$$\min_{\varphi} \|U_1 - e^{i\varphi}U_2\|_{\text{op}} \geq \sqrt{2}\sqrt{1 - \sqrt{\mathcal{F}_s(\Psi_1, \Psi_2)}}. \tag{3.84}$$

3.5 Numerical results

Here, we use the QuTiP implementation of GRAPE using L-BFGS as an optimiser with exact gradients. Explicit details about the mechanism of this optimisation algorithm are described in Appendix A. The optimisation takes place over piecewise-constant functions, which means that the number of time-steps becomes an additional parameter of our numerics. For all numerical results the interaction factor in the Hamiltonian is set to $J = 1$.

3.5.1 Optimised non-adiabatic pulses in a simple lattice

While the timescale of anyon creation through adiabatic evolution can be very long, if instead of using linear ramps we use non-linear time-dependence in the Hamiltonian which have been specially designed, then we can achieve high fidelities at shorter timescales. A well-tested gradient-ascent pulse engineering algorithm [35, 75] (see Appendix A) is used to develop such time-dependent control functions also known as pulses.

The results of using this procedure for a single plaquette of six spins are depicted in Fig. 3.6 showing infidelities as a function of the ramp time T. The infidelities obtained with a linear ramp are depicted in blue. There is a slight improvement with increasing ramp time, but the fidelity of approximately 90% achieved with a ramp time of $T = 1$ is only a very small improvement compared to the initial fidelity at time $T = 0$. This is

consistent with an estimate based on the spectral gap condition [76] that implies ramp times $T \gg \delta^{-2} = 3.480\ldots$ are required for high-fidelity operations. This spectral gap is calculated from the vortex gap of $\delta = |-4J - (-2\sqrt{3}J)| \approx 0.536$. This is a narrower gap than the first fermionic excitation energy penalty which is $2J$. While in general the fermionic excitation gap is a function of J, and K and so can be narrower than the vortex gap, in this special case of the single plaquette lattice this is not the case.

The behaviour with optimised ramps, depicted in orange, is fundamentally different. In the range $T < 0.2$ there is a much faster decrease of infidelity with increasing ramp time than in the case of linear ramps. This decrease is a bit less pronounced in the range $0.2 \lesssim T \lesssim 0.4$, but for ramp time $T > 0.4$ this decrease becomes increasingly pronounced with increasing ramp time. For ramp times $T \gtrsim 0.8$, there is a rapid drop in the infidelity, and for ramp times exceeding the threshold value of $T = T_d \simeq 0.85$, the deviations between the numerically obtained infidelities and the ideal value of 0 are consistent with noise due to finite numerical accuracy.

It is by no means surprising that even with an optimised ramp a finite ramp time is required to reach perfect fidelities. This is due to the constant part in the system Hamiltonian Eq. (3.12) that defines a natural time-scale of the system. This effect is also referred to as the *quantum speed limit* [77, 78] and we will refer to the threshold value T_d of ramp durations at which fidelities drop to values close to their ideal value as the *drop time*. Apart from limitations imposed by finite-dimensional parametrisation of the ramp function, the numerical optimisation routine and numerical accuracy, this drop time coincides with the minimal duration required to reach perfect fidelity.

The example of a single plaquette with six qubits is also a good test-case to compare optimisation of state-fidelity and Heisenberg fidelity. Fig. 3.7 depicts the Heisenberg fidelity obtained with various ramp functions as a function of the ramp time T.

The black triangles represent state fidelity data obtained with linear ramps. Consistently with Fig. 3.6, there is only a moderate decrease of the infidelity with increasing ramp time. The circles correspond to ramp functions optimised for Heisenberg fidelity, and the different colours correspond to different chosen adiabatic target times with $T = 100$, 200

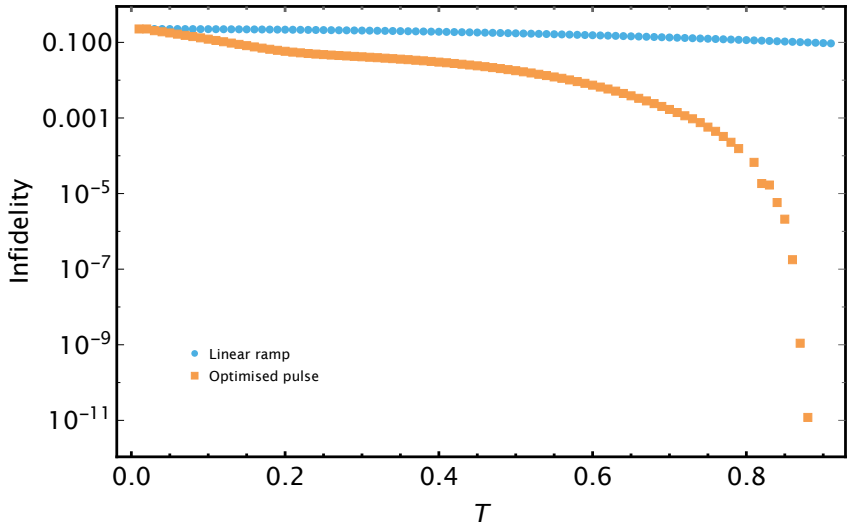

Figure 3.6: Logarithmic comparison of infidelity between initial and adiabatic target state for linear control pulses and optimised control pulses, at various timescales, for the simplest 6-qubit lattice. 100 time steps were used in both cases. We can see more clearly the dramatic improvement in fidelity at approximately $T = 0.8$. The minimum infidelity reached by optimised pulses, on the order of 10^{-9} is reached at time $T \approx 0.9$, many orders of magnitude less than the time to reach this infidelity with the linear ramp, which is at $T \approx 1350$.

and 300 for red, orange and green respectively. Similarly to the observations in Fig. 3.6 there is a clear drop of the infidelities at a drop time $T_d \simeq 3$. The fact that the numerically observed drop time is essentially the same in all three cases indicates that the drop time is not dependent on the length of the adiabatic target time that is chosen.

The squares depict the state infidelity obtained from the ramp functions that had been optimised for Heisenberg infidelity, in order to see numerical evidence that when implementing our procedure, good fidelity is achieved in the one case which ensures a good infidelity in the other.

Here also is a clear drop of the infidelities and it occurs at the same drop time as for Heisenberg infidelities. The fidelities obtained for ramps with a longer ramp time than the drop time T_d, however, are not merely limited by numerical accuracy, but they are indeed finite. Their exact value depends on the parametrisation of the ramp function, with finer parametrisations resulting in lower infidelities. Since state fidelity and Heisenberg fidelity are not strictly equivalent, it is not surprising, that a ramp that is optimised for one of these fidelities does not yield the optimally achievable value of the other fidelity. The results in Fig. 3.7, however, clearly show that ramps optimised for Heisenberg fidelity

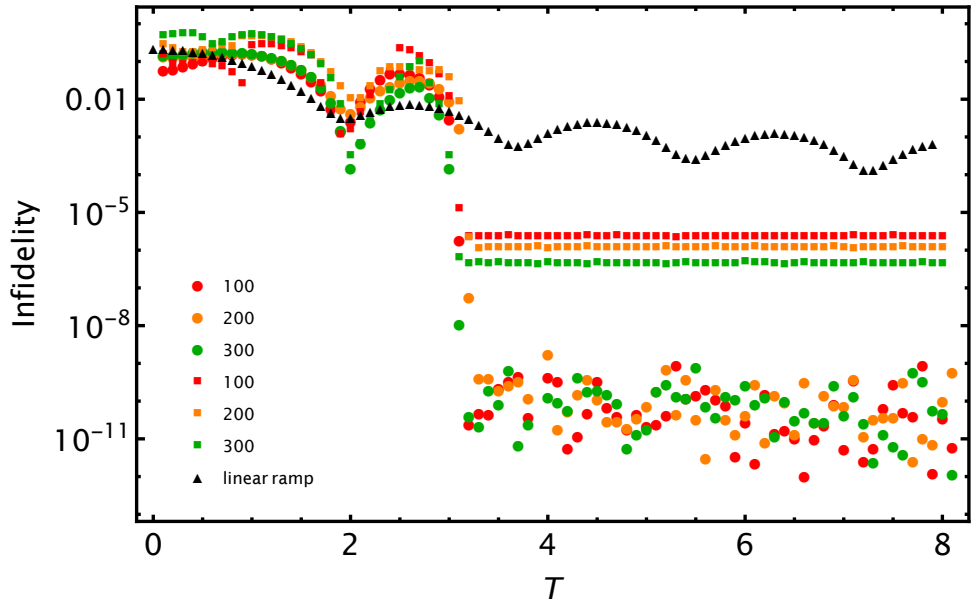

Figure 3.7: Six-qubit lattice: Heisenberg infidelities based on differing targets (circles) are compared with their corresponding state fidelities (squares). These are compared overall with state fidelities achieved from linear ramp pulses (triangles). Different colours represent different values of T_{ad}, which are the timescales of 100 (red), 200 (orange) and 300 (green) that define the target unitary W_{ad}. All optimised pulses are comprised of 200 time steps. There is a significant improvement at times between $T = 2$ and $T = 4$. Thereafter there is effectively perfect fidelity with the presence of numerical noise. It confirms that both Heisenberg and state infidelities improve markedly at the same time T and this is an improvement on the fidelities achieved with a linear ramp pulse.

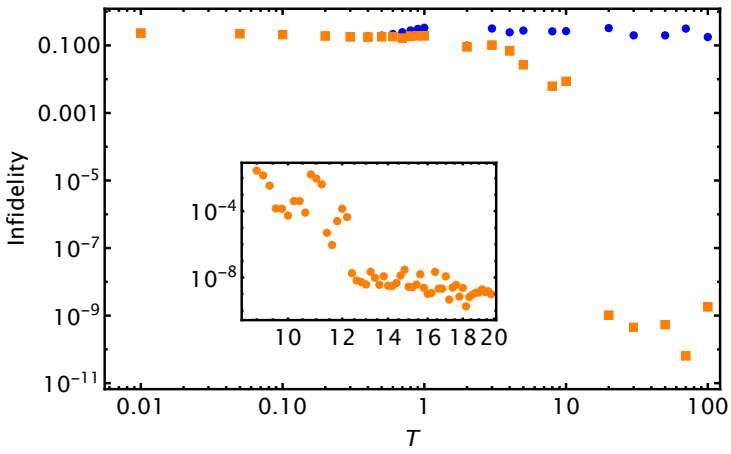

Figure 3.8: Ten qubit lattice: Heisenberg infidelities between optimised unitaries and an optimised target are shown (orange), as compared with infidelities between the target and a unitary defined by a linear ramp control (blue). Each optimised pulse consists of 200 time steps. The drop time is $T \approx 10$, later than for the 6-qubit lattice.

result in high state fidelities and, in particular, in infidelities that are between 3 and 4 orders of magnitude lower than infidelities obtained with linear ramps.

Since numerical optimisations of state fidelity become rapidly infeasible with increasing system size, the subsequent examples for larger systems feature only Heisenberg fidelities with ramps that are optimised for this Heisenberg fidelity. Fig. 3.8 shows the Heisenberg infidelity as function of ramp time for linear ramps (blue) and for optimised ramps (orange). Similarly to the cases discussed above, there is a clearly identifiable drop time T_d, but its value $T_d \simeq 10$ is larger than in the examples of smaller systems. The abscissa depicts that ramp time on the log-scale, highlighting that linear ramps with durations exceeding the drop time by many orders of magnitude are required to achieve any sizeable decrease in infidelity.

The inset depicts a zoomed-in look into the domain around the drop time. It highlights that, on top of the rapid drop of infidelity there is also a finite noise level. When we compare the optimisation results of a system made up of ten spins and one with thirty spins, whose optimised infidelities are shown in Fig. 3.9, we see again the marked increase in drop time that is achieved. Here the spectral gap condition, calculated analogously as with the six and ten-qubit systems, requires the adiabatic timescale for this system to be $T \gg \delta^{-2} \approx 30$. In the thirty-qubit lattice the vortex gap remains smaller than the

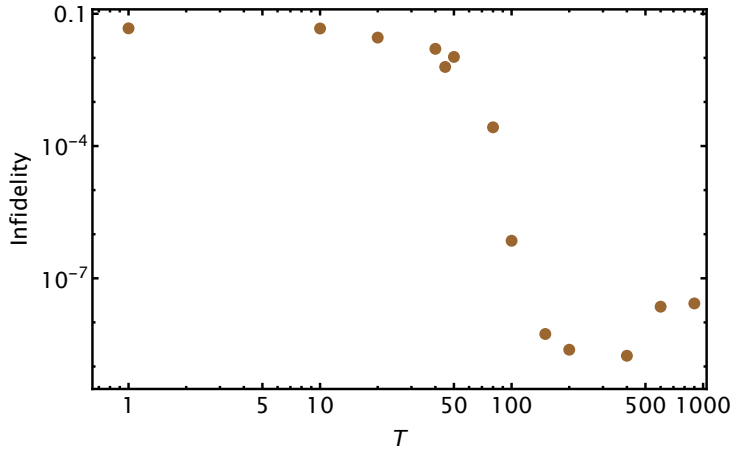

Figure 3.9: Thirty qubit lattice with open boundary conditions and pulses with 400 time steps. Heisenberg infidelities between optimised unitaries and an optimised target are shown. The spectral gap condition requires that $T_{\text{ad}} \gg 30$. The results show that T_d is within the order of magnitude of 30 rather than many orders of magnitude larger as required by adiabaticity, highlighting the improvement in timescale achieved.

lowest fermionic energy gap but for larger systems this may not necessarily be the case. Additionally the smallest gap may not be the vortex gap as compared with the fermionic gap in scenarios where vortices are created from a non-zero vortex sector.

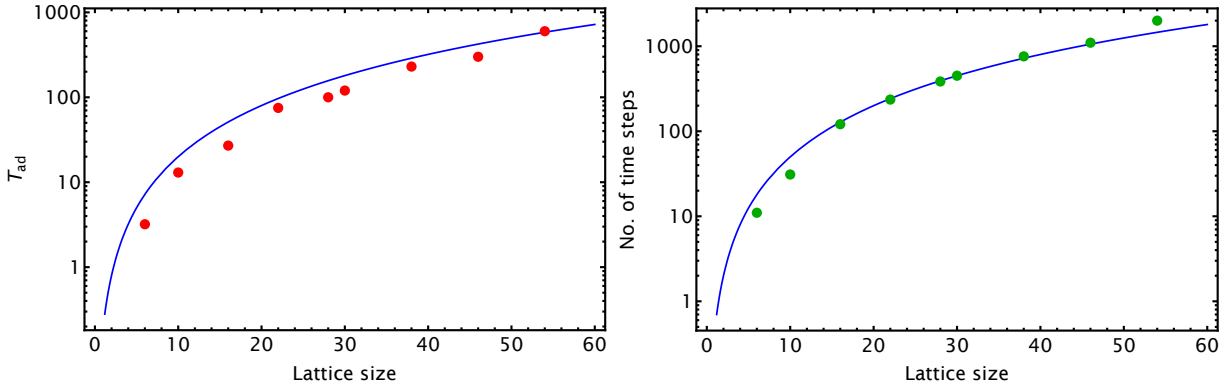

Figure 3.10: Drop time (**Above**) and minimum required time steps (**Below**) compared with lattice size by number of qubits. These quantities are defined as the earliest time T and minimum number of time steps in an optimised piecewise-constant pulse respectively where Heisenberg infidelity drops below 10^{-6}. They are compared with quadratic growth curves (blue) to show sub-exponential growth.

The observation that the drop time increases with the system size is depicted more systematically in Fig. 3.10. Generally, the practically achievable drop time depends on the parametrisation of the ramp function and the number of free parameters that can be optimised. Only for a ramp function with sufficiently many piecewise constant elements

is the drop time independent of the number of free parameters. Fig. 3.10 depicts that shortest achievable drop time together with the minimal number of piecewise constant elements in the ramp function that is required to achieve this drop time. In both sub-plots the scaling is consistent with a quadratic increase (blue line) with system size.

Within the validity of extrapolation from numerically accessible system sizes, there is thus a very moderate scaling with system size, highlighting that numerical optimisations based on the framework of fermionisation can be performed efficiently.

3.6 Summary

It is well known that the Kitaev honeycomb model is a useful system for the encoding of quantum information using non-abelian anyons. Our use of quantum control techniques has allowed us to create anyons not only in adiabatic timescales, but to overcome the necessity for such a restriction through the use of gradient ascent pulse-engineering to construct non-linear ramps whose timescales are many orders of magnitude faster than adiabatic. These ramps achieve very high fidelities at these much faster timescales, and thus are more useful for the encoding of quantum information and quantum algorithm implementation given that decoherence times entail a preference for shorter timescales.

Along with the drawback of requiring long timescales with adiabatic control, the other chief drawback we would encounter with non-adiabatic quantum control is the difficulty in completely determining the dynamics of honeycomb lattices with large numbers of spin qubits. The method we have developed allows us to overcome this obstacle by solving a matrix control problem where the matrices grow linearly in the number of lattice spins, allowing for the implementation of non-linear pulse-engineering and optimisation of a related matrix or Heisenberg fidelity. This, alongside the analytic expression directly comparing state fidelity and Heisenberg fidelity allows us to be assured of the success of these optimised ramps and allows us to have confidence in the successful implementation of our procedure for use in experimental realisation of the model. Given the various avenues suggested for experimental implementation of the Kitaev honeycomb model such

as in solid state materials [55] and with polar molecules in optical lattices [79], as well as the success in observing topological order in quantum spin liquids using the Rydberg blockade mechanism [80, 81] we believe our control methods would be useful for realisation within a setup that allows for varying spin interactions in a time-dependent manner.

Furthermore we have seen that there is indeed sub-exponential growth in the computational difficulty of our control problem with growing system size and so carrying out our methods on lattices on the order of hundreds of qubits is possible, as necessary for scalable topological robustness.

Chapter 4

Surface code defects and dynamical Lie algebras

In this chapter we present how quantum optimal control may be utilised in order to speed up the process of defect creation in a lattice system known as the surface code.

The surface code is a generalisation of the toric double quantum code [45] that does not require periodic boundary conditions. It can be defined by a Hamiltonian comprised primarily of four-body interactions known as stabilisers. When certain stabilisers are removed by a process known as 'puncturing' [82, 83], defects are created in the code wherein quantum information may be encoded. Defect deformation and braiding also allows for the possibility of logical gates to be performed on the encoded logical qubits in the code.

As with other examples of topological systems which have shown potential in terms of suitability for quantum computation, the realisation of anyons and anyon-like defects has relied on using adiabatic dynamics [56, 82] and therefore requires long timescales. Such requirements amount to a limitation on the experimental realisation of the system, given the necessity of implementing quantum algorithms quickly with respect to decoherence times. Here we seek to overcome this limitation via the use of time-optimal quantum control.

The techniques of quantum optimal control have been shown to successfully effect

desired dynamics while bypassing adiabatic, therefore slow, timescales [39, 40, 31, 41, 42, 44]. Quantum control in general relies on determining specific chosen time-dependent Hamiltonians in order to implement desired dynamics [15, 19]. We seek to use numerical quantum optimal control to successfully carry out operations required for encoding and processing logical qubits in the surface code within timescales that are much shorter than those which would be required by adiabatic protocols.

One potentially significant obstacle to numerical solving of dynamics in lattice systems is the large Hilbert space size when operating with many spins. Our work presents a method whereby the dynamical Lie algebra of a Hamiltonian system, which determines the entirety of the system's dynamics, is mapped onto a smaller equivalent system such as to allow for numerical quantum control techniques to be more efficiently implemented. This method is not yet generalisable to all possible control problems but is certainly valuable in that it allows for easier numerical optimisation for many types of quantum control problems which have useful and varied applications. The mapping of a system's dynamics into that of a smaller size so as to allow for solving in the larger system is motivated by previous work on mapping a lattice system's Hamiltonian to a free fermion model (see Chapter 3).

Section 1 of this work presents a brief overview of the surface code, followed by a description in Section 2 of how adiabatically changing Hamiltonians allows for defects in the surface code to be created and manipulated, as described in more detail in the literature [82]. In Section 3 we begin presenting our work by describing in detail the quantum control methods used as well as present our optimisation results for the four major operations required for encoding and manipulating quantum information in the surface code. For three of the four operations this consists of numerical optimisation while for the fourth operation, known as surface code detachment, a more sophisticated technique of dynamical Lie algebra mapping is developed and is described in detail in Section 4. With this method the difficulties of analysing in view of manipulating the dynamics of a system in a very large Hilbert space are bypassed by considering an equivalent dynamics described by an isomorphic dynamical Lie algebra.

Sections 1 and 2 are for review purposes only and are intended to describe the well-known attributes of the surface code and adiabatic procedures on it.

4.1 Description of the surface code

As with the toric code [45] (see Chapter 2), the surface code lattice is comprised of a large number of spin-1/2 degrees of freedom on the edges of a square lattice as shown in Fig. 4.1. Stabiliser operators are defined by four-body Pauli X interactions on vertices and Pauli Z interactions on plaquettes. The vertex and plaquette operators, A_v and B_p are respectively defined on a vertex v and plaquette p as

$$A_v := X_{v_1,v_2,v_3,v_4} \tag{4.1}$$

$$B_p := Z_{p_1,p_2,p_3,p_4} \tag{4.2}$$

where $X_{v_1,v_2,v_3,v_4} := X_{v_1}X_{v_2}X_{v_3}X_{v_4}$ and $Z_{p_1,p_2,p_3,p_4} := Z_{p_1}Z_{p_2}Z_{p_3}Z_{p_4}$.

Lattices may include 'rough sides' where plaquette operators on the edge are defined only with three-body terms, as well as 'smooth sides' where vertex operators on such edges are defined with three-body terms. Fig. 4.1 shows smooth sides on the top and right side of the lattice and rough sides on the bottom and left side. If both smooth *and* rough sides are present then for two of the four corners of the lattice (in the example shown in Fig. 4.1 these would be the top right corner and the bottom left corner) there is defined for each a corresponding *two-body* stabiliser, either a vertex or plaquette operator.

With the stabilisers defined, one can see that as a plaquette stabiliser B_p and a vertex stabiliser A_v can overlap only on an even number of qubits, all stabilisers must therefore commute with one another. Additionally each stabiliser squares to the identity. Defining the system Hamiltonian as

$$H_0 = -\frac{\Delta}{2}\left(\sum_v A_v + \sum_p B_p\right) \tag{4.3}$$

then the ground state up to normalisation is the same as with the toric code

$$|g_0\rangle = \prod_v (\mathbf{1} + A_v) \, |0\rangle^{\otimes N} \, . \tag{4.4}$$

Unlike the toric code however, the ground state space is non-degenerate due to the open boundary conditions of the lattice. This would initially seem to make it unfeasible for use as a system for topological quantum computation. However the required degeneracies are introduced through 'puncturing' of the lattice, an operation amounting to the removal of certain stabilisers from the Hamiltonian. Each puncture doubles the size of the ground state degeneracy.

4.2 Hamiltonians, stabiliser formalism and adiabaticity

Quantum information is encoded in the lattice via the stabiliser formalism [84] whereby a logical qubit is defined by a set of stabiliser operators such that the qubit corresponds to a physical state which is simultaneously in a $+1$ eigenstate of the entire stabiliser set. If we were to start with a full surface code lattice and implement a defect, that is we remove either a plaquette (Z defect) or a vertex (X defect) stabiliser, we would create a code whereby the logical gate $\bar{Z}$ corresponds to a string of Pauli Z operations on the lattice around the defect. The logical gate $\bar{X}$ would then correspond to a string of Pauli X operations from the smooth defect to a smooth edge. The aim therefore is, when beginning in the ground state of an initial Hamiltonian H_i, to end up in the corresponding state of a final Hamiltonian H_f which amounts logically to an encoding of a specific logical quantum state. Each Hamiltonian is comprised of the stabiliser set of a different configuration of logical quantum information. The deformation of these codes is studied in the literature as physically being implemented through 'adiabatic dragging' [82, 85, 86] between the initial and final Hamiltonians of each particular procedure (see [82]).

There are four major operations that can be implemented in order to create defects

in the surface code, encode logical qubits within them, and manipulate their location or grow them in size to give the encoded qubits further protection.

4.2.1 Defect creation

Described here is the creation of a smooth (Z-type) defect and a logical $|\bar{0}\rangle$ state localised on two neighbouring plaquettes in the surface code. The creation of a rough defect is an analogous procedure, with the roles of X and Z interactions reversed. Labelling of spins throughout the work will follow a convention of numbering sites from rows going top to bottom and from left to right within each row, such as that which is shown in Fig. 4.1.

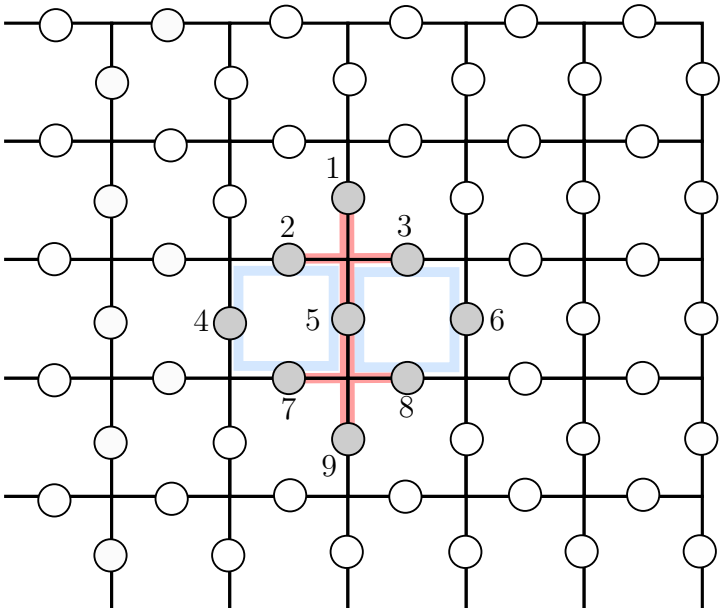

Figure 4.1: Depiction of the spin acted on during defect creation. Only nine spins are affected. The two plaquettes $B_{p_1} = Z_{2,4,5,7}$ and $B_{p_2} = Z_{3,5,6,8}$ are removed from the Hamiltonian and turn from stabilisers into logical gates ($\bar{Z}$) on the encoded qubits. The upper vertex v_1 consists of qubits 1,2,3 and 5 while the lower vertex v_2 corresponds to qubits 5,7,8 and 9.

The procedure consists of starting with the Hamiltonian described in (4.3) as an initial Hamiltonian and transforming it into a final Hamiltonian where specific stabilisers are removed. Given that all of the vertex and plaquette stabilisers which are not involved in the defect creation commute with all the terms in the initial and final Hamiltonian, the Hilbert space of the dynamics of interest reduces to 2^9 and thus it suffices to consider the

initial and final Hamiltonians

$$H_i = -\frac{\Delta}{2}(X_{1,2,3,5} + X_{5,7,8,9} + Z_{2,4,5,7} + Z_{3,5,6,8}) \tag{4.5}$$

$$H_f = -\frac{\Delta}{2}(X_{1,2,3} + X_{7,8,9}) - \frac{\Delta}{2}X_5 \tag{4.6}$$

where the spectral gap Δ remains unaltered despite the system size reduction.

Qualitatively, this amounts to turning off the plaquette stabilisers $Z_{2,4,5,7}$ and $Z_{3,5,6,8}$ from the Hamiltonian, and proceeding to define the product of these operators as the *logical gate* $\bar{Z}$ of the logical qubit encoded in the ground state of the final Hamiltonian. When the two plaquette stabilisers are removed, in addition the overlapping vertex stabilisers $X_{1,2,3,5}$ and $X_{5,7,8,9}$ are modified from four-body operators to three-body ones. For a smooth defect, a logical gate $\bar{X}$ is then simply a string of Pauli X operators defined on a string traversing the geometrically dual lattice starting from the defect and ending at a smooth edge. These two possible $\bar{X}$ gate strings can be made to overlap on just a single spin, namely spin 5 as labelled in Fig. 4.1, and this accounts for the why the single X_5 term is required in the final Hamiltonian, as it can be considered as a stabiliser itself. The ground state of the final Hamiltonian can then be labelled the logical state $|\bar{0}\rangle$ defined, up to normalisation, by

$$|\bar{0}\rangle = (\mathbf{1} + A_{v_1})(\mathbf{1} + A_{v_2}) \dots (\mathbf{1} + X_{1,2,3})(1 + X_{7,8,9})(1 + X_5) \, |0\rangle^{\otimes N} \tag{4.7}$$

where the A_{v_n} operators are the four-body vertex stabilisers that remain unmodified throughout. The logical $|\bar{1}\rangle$ is then defined as

$$|\bar{1}\rangle = X_{\text{string}} \, |\bar{0}\rangle = X_5 X_{\text{string}} \, |\bar{0}\rangle \tag{4.8}$$

where X_{string} is any string of Pauli X operators acting on spins from the defect to a smooth edge. This uses the fact that $X_5(\mathbf{1} + X_5) = (\mathbf{1} + X_5)$.

To summarise, in defect creation the system begins in the unique ground state of H_0 and ends up in the logical state $|\bar{0}\rangle$ encoded in the defect that has been created on a pair

of plaquettes. The logical qubit has a corresponding $\bar{Z}$ gate defined as the product of the two plaquette stabilisers which have been removed, as well as a $\bar{X}$ gate defined as a string of Pauli X operators from the defect to a smooth edge.

4.2.2 Deformation of defects

While logical qubits can be encoded onto defects, these defects need to be moved around on the lattice in order to implement logical gates. A typical example is the CNOT gate which is implemented by the braiding of one defect around another. It is also desirable for the defect to be grown so that the defect spans multiple plaquettes (or vertices) which gives greater protection against unwanted logical gate errors. The deformation of defects can involve four possible scenarios depending on the number of interior spins, from 1 to 4, within a defect that need to be acted on.

Each scenario differs slightly from the others and we describe the first scenario here as a concrete example. This scenario is illustrated in Fig. 4.2.

This operation only involves interaction with 7 qubits with the aim of growing a smooth defect such that it transforms from being localised on a two-by-two square of plaquettes to a defect covering five plaquettes. The initial Hamiltonian would be

$$H_i = -\frac{\Delta}{2}(Z_{3,5,6,7} + X_{2,3,5} + X_{1,3,4,6}) \tag{4.9}$$

with the final Hamiltonian

$$H_f = -\frac{\Delta}{2}(X_3 + X_{2,5} + X_{1,4,6}). \tag{4.10}$$

The other three scenarios are conceptually similar except that they act on eight, eight and four spins respectively.

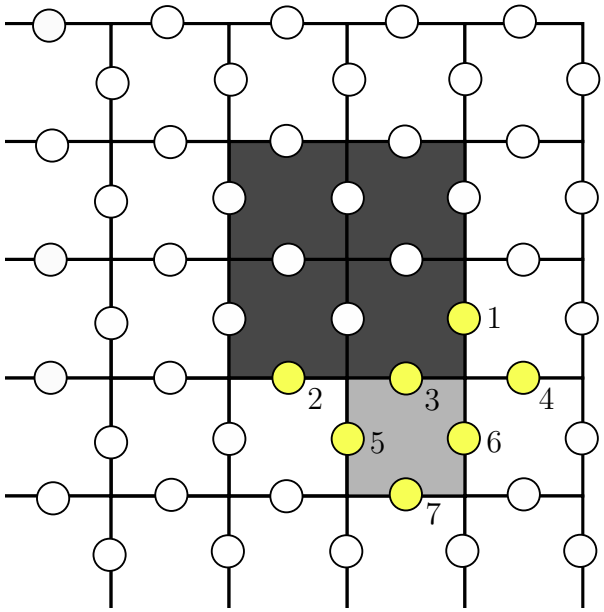

Figure 4.2: Surface code lattice with a defect covering four plaquettes, where the defect is to be deformed so as to cover a fifth plaquette defined on spins 3,5,6 and 7. The spins affected by the operation are numbered and shown in yellow. The current plaquettes containing the localised defect are in dark grey while the proposed fifth plaquette is in light grey.

4.2.3 Detachment of surface code regions

Multi-step operations such as state injection (described below) require detachment and attachment of surface code areas containing defects. Looking at the example of detachment, the removal of an area is shown in Fig. 4.3; this amounts to the removal of a plaquette stabiliser operator on the plaquette connecting the two regions.

Explicitly this corresponds to starting with an initial Hamiltonian

$$H_i = -\frac{\Delta}{2}(X_{1,3,4,6} + X_{2,4,5,7} + X_{6,8,9,11} + X_{7,9,10,12} + X_{4,9} + Z_{4,6,7,9}) \tag{4.11}$$

and ending with a final Hamiltonian

$$H_f = -\frac{\Delta}{2}(X_{1,3,6} + X_{2,5,7} + X_{6,8,11} + X_{7,10,12} + X_4 + X_9) \tag{4.12}$$

Here the initial Hamiltonian H_i is the negative sum of the four-body terms, one of which

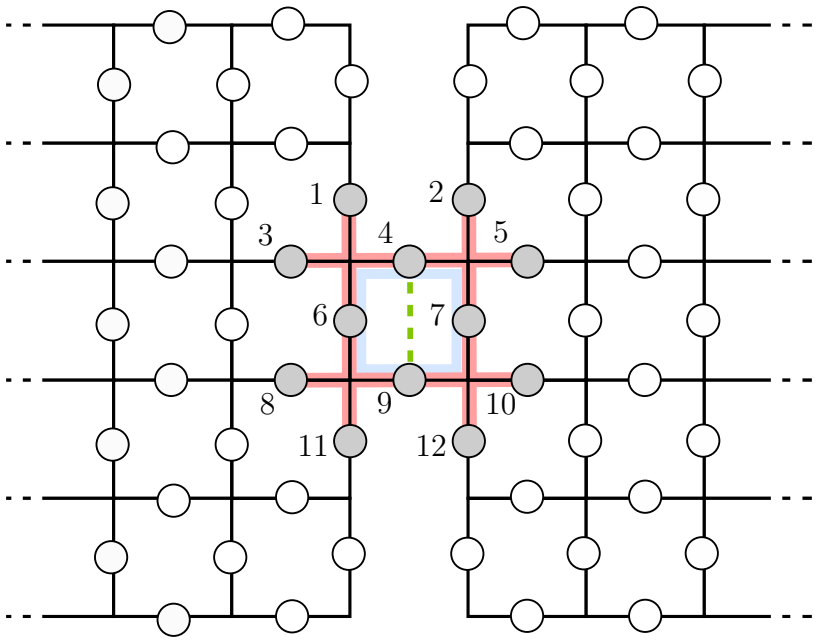

Figure 4.3: The two areas shown are to be separated through the removal of the stabiliser connecting them. The four surrounding four-body vertex operators then become three-body terms.

is the plaquette stabiliser that is to be turned off, as well as a two-body check term X_4X_9. The final Hamiltonian H_f is then comprised of each four body stabiliser turned into a three-body stabiliser, the plaquette stabiliser removed, and the two-body check term replaced by two single body terms.

This operation requires all overlapping vertex stabiliser operators, of which there are four, to be modified from four-body terms into three-body terms, such that if we wish to remove the plaquette operator and modify the vertex operators in one go, this would affect twelve spins and so the Hilbert space size where the dynamics are implemented is large compared with the other operations.

4.2.4 State injection

This scenario involves turning the logical states that have been encoded upon the defects, whether $|\bar{0}\rangle$ or $|\bar{+}\rangle$, into various fiducial states such as the canonical example of $\bar{T}|\bar{+}\rangle$ where T is the phase gate such that $T^4 = Z$.

This comprises several steps, including: i) Creating a pair of rough defects in an

eigenstate of X; this procedure is analagous to that of creating smooth defects described previously. ii) Ensuring that the defect is in a region which is smoothly detached from the rest of the surface code. This involves the detachment procedure described in the detachment/attachment section. iii) Adiabatically or otherwise 'injecting' the desired logical state onto the spin qubit located between the pair of defects. This simply means evolving the state of the spin qubit from $|\psi\rangle$ to $TX|\psi\rangle$. iv) Deforming the pair of defects from rough to smooth by turning off the two adjoining (three-body) plaquette stabilisers and turning on the vertex stabilisers.

Out of these, the first procedure which is distinct from the other three operations is the actual state injection which is carried out on a single qubit in the interior of a pair of rough defects. The second such procedure consists of turning on the adjoining vertex operators and turning off the overlapping three-body plaquette operators. Hence we can define initial and final Hamiltonians

$$H_i = -\frac{\Delta}{2}\left(Z_{1,2,3} + Z_{7,8,9}\right) \tag{4.13}$$

$$H_f = -\frac{\Delta}{2}\left(X_{2,4,5,7} + X_{3,5,6,8}\right) \tag{4.14}$$

respectively. This procedure is illustrated in Fig. 4.4.

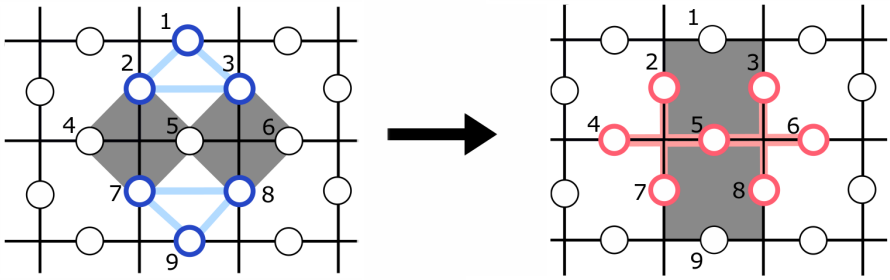

Figure 4.4: Illustration of how defects are transformed and stabilisers are removed and re-introduced for the state injection procedure. Three-body plaquette operators $Z_{1,2,3}$ and $Z_{7,8,9}$ are turned off while four-body vertex operators $X_{2,4,5,7}$ and $X_{3,5,6,8}$ are turned on. A total of nine qubits are acted on during this operation.

Solving the dynamics of this second procedure is more numerically challenging than for the first procedure as the latter takes place within a 2^9-dimensional Hilbert space.

4.3 Quantum optimal control

4.3.1 Defining the control problem

Considering the implementation of these operations as quantum control problems involves reformulating the initial and final Hamiltonians into a more general time-dependent Hamiltonian with a control $f(t)$. Typically in a control problem there is a time-independent part known as the drift Hamiltonian and a time-dependent part known as the control Hamiltonian which is coupled to the control function. Analogously, two Hamiltonians are chosen

$$H_1 = H_i \tag{4.15}$$

$$H_2 = H_f - \tilde{H}_i \tag{4.16}$$

so that we have the control problem defined as

$$H(t) = H_1 + f(t)H_2. \tag{4.17}$$

In the adiabatic regime $f(t)$ may simply be a linear ramp with a very small slope such that $f(0) = 0$ and $f(T) = 1$ for T being a long timescale, thereby ensuring adiabatic dynamics. We call such a pulse a linear ramp $f_{\text{ad}}(t)$.

We define an initial state $|g_1\rangle$ being a ground state of H_1 and this in turn defines a target state $|g_{\text{targ}}\rangle$ by

$$|g_{\text{targ}}\rangle = U(f_{\text{ad}}(T))\,|g_1\rangle \tag{4.18}$$

where adiabaticity ensures that $|g_{\text{targ}}\rangle$ is a ground state of the final Hamiltonian $H_1 + H_2$. This allows for the definition of a target fidelity, as a function of the control pulse

$$\mathcal{F}(U(f,t)) = |\langle g_{\text{targ}}|\,U(f(t))\,|g_1\rangle|^2\,. \tag{4.19}$$

The closely associated target infidelity $\mathcal{I} = 1 - \mathcal{F}$ is the figure of merit which is often sought to be minimised.

For some other operations, where the goal is to implement desired full dynamics rather than specific state transfer, we may look at a similar unitary *gate fidelity* defined as

$$\mathcal{F}(U) = \frac{1}{d}\left|\mathrm{Tr}\left(U_{\mathrm{targ}}^{\dagger}U\right)\right|. \tag{4.20}$$

In order to optimise for infidelities, we use a gradient ascent pulse engineering algorithm (GRAPE) [35, 36]. This procedure uses piecewise constant control pulses where, after an initial random control is picked, the parameters such as pulse magnitude are varied in order for infidelity to go down in the control space until acceptable minima are found. The direction of descent in control space is determined by second derivatives of the infidelity which are calculated using the limited memory version of the Broyden–Fletcher–Goldfarb–Shanno method (BFGS) [87, 88, 89, 90, 91]. This method uses an estimate of the Hessian matrix of second derivatives of the figure of merit and allows for a parabola to be used for approximating the control space and descending towards local minima (for more information, see Appendix A).

GRAPE is used to find appropriate piecewise constant control pulses and choose the best fidelity for a given time period. Numerous parameters may be varied such as initial pulse guess and number of pulse time steps.

4.3.2 Non-adiabatic optimisation

The result of our optimisations on three of the four major surface code operations, presented in Fig. 4.6 and Table 4.1, indicate that quantum optimal control can indeed allow for an improvement of multiple orders of magnitude in timescale required for achieving the appropriate target states of the operations.

In Fig. 4.5 are presented the state infidelities between the ideal target state, which corresponds to defect pair creation on the surface code, and the state achieved by using a linear control that goes from 0 to 1 in time T. Here as with elsewhere in this work

timescales are understood to be in units of Δ^{-1} where Δ is the spectral gap in the initial Hamiltonian H_1. The logarithmic plot displays the improving fidelity that is achieved with linear ramps of longer timescales. In particular, when $T < 1$ there is a comparatively high infidelity that stays effectively constant whereas for timescales longer than this, the infidelity improves steadily. Considering an infidelity of 10^{-7} as a standard for sufficiently good infidelity we see that this is achieved for timescales of $T \gtrsim 1000$. This is indeed consistent with the spectral gap of 1 in the units of Δ^{-1} as an effectively perfect fidelity is expected when adiabaticity is achieved which can only occur according to the adiabatic theorem when the timescale is much longer than the inverse of the spectral gap [92].

In Fig. 4.6 are presented the results of using optimisation of state infidelity to find non-linear controls that can achieve high fidelities for defect creation. Good fidelities (shown in orange) were achieved with only two time steps in the optimised pulses. Each data point corresponds to the minimum of 1000 optimisation attempts with random initial pulse guess. The results show that successfully creating the defect pair state, that is, to achieve a good infidelity of 10^{-7} as mentioned previously, can be achieved at a timescale of $T \approx 1.15$. The earliest timescale at which effectively perfect fidelity is achieved hereafter is referred to as *drop time*. Furthermore we see the comparison between use of non-optimised linear control ramps and the optimised pulses when comparing fidelities (plotted in blue and orange respectively) as there is a marked improvement, particularly after the drop time where infidelities are shown to improve by over 10 orders of magnitude.

The results of carrying out the same optimisation procedure for defect creation and for two other operations, namely defect deformation and state injection, are qualitatively similar and are presented in Table. 4.1. The results show that there is a variance of the drop time but all operations achieve effectively perfect fidelity at times much smaller than the adiabatic timescale. An appropriate measure of this is comparison between optimised infidelity at drop time with the infidelity using a linear control pulse with same duration. Quantum control optimisation methods can be seen therefore to give an infidelity improvement generally on the order of 10 orders of magnitude.

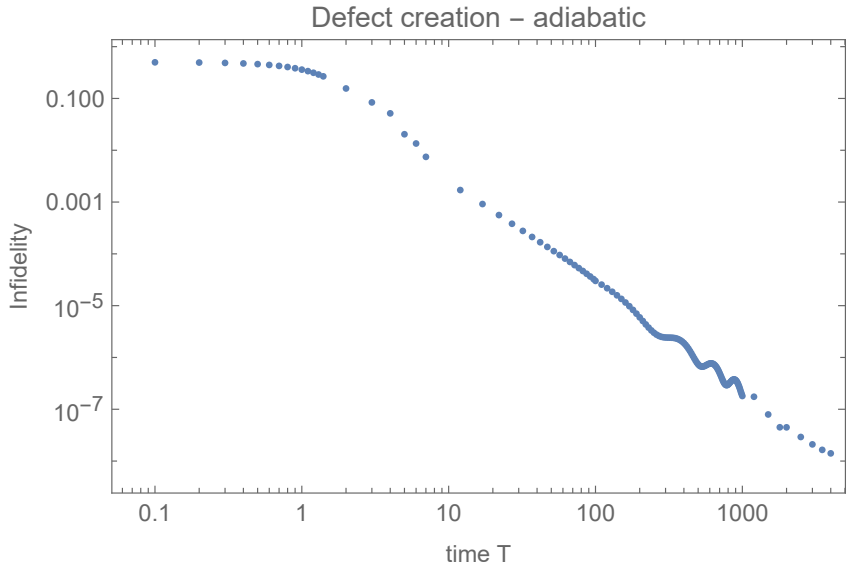

Figure 4.5: Fidelity of defect creation with linear ramps as control functions. Fidelity when using linear ramps only becomes good at long timescales T, where adiabaticity is achieved. Time units are Δ^{-1}.

Operation	spins	T_d	N_τ	$\mathcal{I}$ linear	$\mathcal{I}$ optimised
Creation	9	1.15	2	0.3251	5.13e-13
Deformation 1	7	2.0	4	0.323	5.50e-12
Deformation 2	8	3.2	4	0.379	8.11e-13
Deformation 3	8	10.0	12	0.166	2.41e-11
Deformation 4	4	5.0	10	0.927	3.32e-12
State injection pt.1	1	2.4	4	0.177	4.37e-14
State injection pt.2	9	1.3	15	0.358	2.23e-12

Table 4.1: Results of quantum control optimisation on three surface code operations, namely defect creation, defect deformation and state injection. Shown in the table are: number of spins acted on in the operation, drop time T_d, minimum required number of time steps in optimised pulses N_τ, infidelity $\mathcal{I}$ with linear pulse at time T_d and optimised infidelity.

4.4 Surface code detachment and dynamical Lie algebra mapping

The operation of detachment and attachment of surface code regions is sufficiently distinct from the other three operations that it requires an alternative approach if we wish to use quantum control to implement it without resorting to adiabaticity. Two spins within the lattice require removal to implement code detachment. It is therefore necessary for all overlapping vertex stabiliser operators (of which there are four; see Fig. 4.3) to be

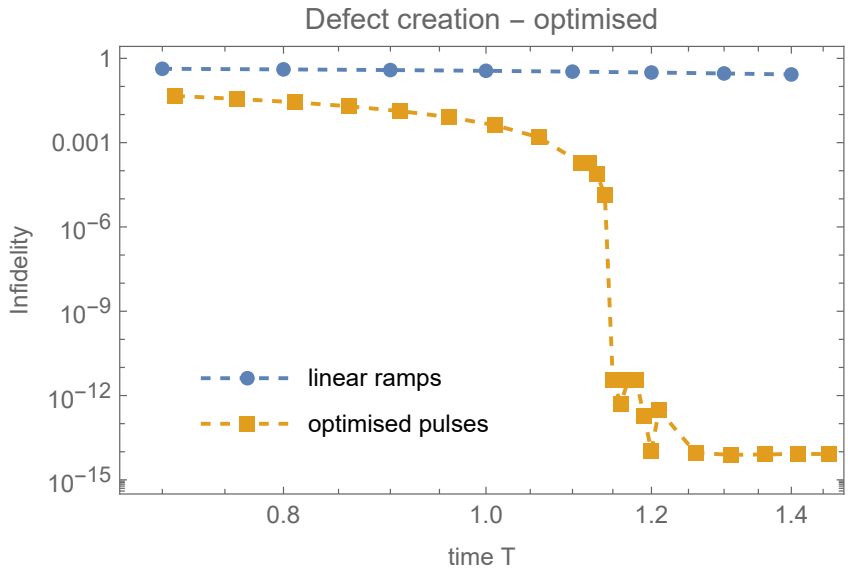

Figure 4.6: Defect creation with optimised non-linear control pulses. The timescale for defect creation with high fidelity is around $T = 1.15$. Time units are Δ^{-1}. The optimised fidelities are shown in orange as compared with the infidelity for a linear ramp at the corresponding time, shown in blue. This is an orders of magnitude improvement compared with using linear adiabatic pulses.

modified from four-body terms into three-body terms, and so in order to remove the plaquette operator and modify the vertex operators, 12 spins must be affected. The effective Hilbert space size of this operation therefore is much larger than for any of the other operations. Moreover, as the primary goal here is to find controls that mimic the behaviour of adiabatic dynamics no matter the initial state, unitary gate fidelity must be optimised rather than the simpler case of state fidelity.

Attempting to solve the dynamics in such a Hilbert space is more challenging than in previous examples and, as optimisation must be carried out many times, this therefore requires large computational resources. It is therefore of interest to find a new approach which could allow for consideration of a simpler but equivalent system. Our method consists of mapping the dynamical Lie algebra of the operation to a smaller dimensional problem and carrying out optimisation in the smaller space. It is also motivated by previous work that uses mapping of a time-dependent many-body Hamiltonian into a free fermion model as a method of solving the dynamics of a system which is of interest for encoding topologically protected qubits [44] (see Chapter 3).

This method allows us to achieve a similar result as with the other operations, where

high fidelities are achieved without resorting to long timescales or scaling of the Hamiltonian with large amplitude control pulses. We achieved a timescale improvement of two orders of magnitude using pulses whose amplitudes are of the order of Δ. Further improvement in timescale is possible to achieve at the cost of higher amplitude pulses.

4.4.1 Mapping between dynamics of two spaces

Presented here in detail is the method of mapping between dynamical Lie algebras, considering the most general case for which the method is applicable and, later, we apply this to the specific control problem corresponding to the surface code detachment operation.

All possible dynamics of a given quantum system with a time-dependent Hamiltonian can be represented by a Lie group of unitary operators $e^{\mathcal{L}}$, whose corresponding, anti-Hermitian, Lie algebra $\mathcal{L}$ is known as the dynamical Lie algebra [15, 93, 94]. The Lie algebra can be considered as an infinitesimal algebra whose basis generates elements of the Lie group. As the Lie group representing the dynamics must be unitary so the dynamical Lie algebra must have anti-Hermitian matrices as a basis. The commutators of all basis elements of the dynamical Lie algebra define structure constants λ_{jk}^{l} from the relation

$$[O_j, O_k] = \lambda_{jk}^{l} O_l \tag{4.21}$$

where the Einstein summation convention is used for repeated indices. These structure constants effectively define a particular representation of the Lie algebra as all Lie bracket relations can be found using them [95].

What we require is a mapping Φ between unitaries U_j in a large dimensional Hilbert space and unitaries u_j in an ideally much smaller dimensional space. This amounts to the mapping

$$U_j = \exp\left(\sum_j \alpha_j O_j\right) \mapsto \exp\left(\sum_j \alpha_j K_j\right) = u_j \tag{4.22}$$

such that there is an isomorphism ϕ, that is, an invertible mapping where structure constants are preserved, between Lie algebras $\mathcal{L} = \text{span}\{O_j\}$ and $\mathcal{M} = \text{span}\{K_j\}$ where

$$\phi\left(\sum_j \alpha_j O_j\right) = \sum_j \alpha_j K_j. \tag{4.23}$$

For simplicity we refer to two different Lie groups as the 'large space' and the 'small space' but we take care to note that this refers only to the dimensions of the particular matrix representations of their Lie algebras. Such a mapping Φ would allow for optimisation of the small unitary u_j by fidelity defined as in (4.20) compared with a target unitary u_T where both small unitaries have well defined counterparts in the larger space.

4.4.2 Construction of a dynamical Lie algebra and the adjoint representation

We determine the dynamical Lie algebra of a general system whose time-dependence means that at any time the Hamiltonian is some linear combination of H_1 and H_2. Initially we define their anti-Hermitian counterparts $A_1 = iH_1$ and $A_2 = iH_2$ respectively. The dynamical Lie algebra is then the list of all linearly independent operators found from nested commutators $[A_j, ... [A_j, A_k]]$ where $j \in \{1, 2\}$. The largest linearly independent set is a basis for the dynamical Lie algebra defined by these matrices as the generators $\mathcal{L} = \text{span}\{A_1, A_2, ...\}$.

In fact, the structure constants themselves give the matrix elements of the adjoint representation of this dynamical Lie algebra through the defining relation

$$[T_j]_{kl} = -\lambda^l_{jk}. \tag{4.24}$$

The proof of this is found below. If there is a small number of basis elements as compared with the dimensions of the matrices themselves then the matrices of the adjoint representation are much more manageable for the purposes of numerical optimisation.

4.4.3 Proof that structure constants define a Lie isomorphism

We claim that for a Lie algebra $\mathcal{L}$ which is spanned by a finite number of basis elements A_j, such that these basis elements are related by the commutation relations

$$[A_j, A_k] = \lambda_{jk}^l A_l \tag{4.25}$$

where λ_{jk}^l are the defining structure constants of the chosen basis, then defining another set of matrices T_j by

$$[T_j]_{kl} = -\lambda_{jk}^l \tag{4.26}$$

gives the relation

$$[T_j, T_k] = \lambda_{jk}^l T_l. \tag{4.27}$$

As a consequence we have a Lie algebra isomorphism between $\mathcal{L}$ and $\mathcal{M} = \text{span}\{T_j\}$ if the T_j matrices are all linearly independent. The proof is well known and is given as follows: define the set of matrices T_j as given in Eq. (4.26). By definition the basis of any Lie algebra such as $\mathcal{L}$ satisfies the Jacobi identity under commutation, thus

$$[A_j, [A_k, A_l]] + [A_k, [A_l, A_j]] + [A_l, [A_j, A_k]] = 0. \tag{4.28}$$

Through Eq. (4.25) this becomes

$$\lambda_{kl}^m [A_j, A_m] + \lambda_{lj}^m [A_k, A_m] + \lambda_{jk}^m [A_l, A_m] = 0 \tag{4.29}$$

$$= (\lambda_{kl}^m \lambda_{jm}^n + \lambda_{lj}^m \lambda_{km}^n + \lambda_{jk}^m \lambda_{lm}^n) A_n. \tag{4.30}$$

Thus the Jacobi identity is here equivalent to the relation

$$\lambda_{kl}^m \lambda_{jm}^n + \lambda_{lj}^m \lambda_{km}^n + \lambda_{jk}^m \lambda_{lm}^n = 0. \tag{4.31}$$

Therefore checking the commutation relations of the matrices T_j one finds that

$$[T_j, T_k]_{ln} = [T_j]_{lm}[T_k]_{mn} - [T_k]_{lm}[T_j]_{mn} \tag{4.32}$$

$$= \lambda^m_{jl}\lambda^n_{km} - \lambda^m_{kl}\lambda^n_{jm} \tag{4.33}$$

$$= -\lambda^m_{lj}\lambda^n_{km} - \lambda^m_{kl}\lambda^n_{jm} \tag{4.34}$$

$$= \lambda^m_{jk}\lambda^n_{lm} \tag{4.35}$$

$$= -\lambda^m_{jk}\lambda^n_{ml} \tag{4.36}$$

$$= \lambda^m_{jk}[T_m]_{ln} \tag{4.37}$$

and hence we have Eq. (4.27) which is now proven.

4.4.4 Proof of a sufficient condition for totally antisymmetric structure constants

In order for dynamics to be unitary there is a preference for the adjoint representation basis matrices to be anti-Hermitian. This is the case only when the structure constants are totally antisymmetric in all three indices, which is not the case in general.

We consider the well-known Hilbert-Schmidt inner product acting on anti-Hermitian matrices

$$I(A_j, A_k) := \mathrm{Tr}\Big(A_j^\dagger A_k\Big) = -\mathrm{Tr}(A_j A_k). \tag{4.38}$$

Orthogonalising the original basis of $\mathcal{L}$ with respect to this inner product leaves a basis whose structure constants, which we call γ^l_{jk} *are* totally antisymmetric. The proof of this is well-known [96] and is presented here. For a finite set of linearly independent matrices O_j such that

$$[O_j, O_k] = \gamma^l_{jk} O_l \tag{4.39}$$

then the rank 3 tensor γ^l_{jk} refers to the structure constants. We assume the set of matrices

has been orthogonalised with respect to the inner product

$$I(O_j, O_k) = -\operatorname{Tr}(O_j O_k) \tag{4.40}$$

so that

$$I(O_j, O_k) = \delta_{jk}. \tag{4.41}$$

It is clear by definition that due to the antisymmetry of the commutator we have

$$\gamma^l_{jk} = -\gamma^l_{kj}. \tag{4.42}$$

Using the summation convention on repeated indices, take

$$\begin{aligned}
\operatorname{Tr}(O_l[O_j, O_k]) &= \gamma^i_{jk} \operatorname{Tr}(O_l O_i) && (4.43)\\
&= \gamma^i_{jk}(-\delta_{li}) && (4.44)\\
&= -\gamma^l_{jk}. && (4.45)
\end{aligned}$$

At the same time we have

$$\begin{aligned}
\operatorname{Tr}(O_l[O_j, O_k]) &= \operatorname{Tr}(O_l O_j O_k) - \operatorname{Tr}(O_l O_k O_j) && (4.46)\\
&= \operatorname{Tr}(O_l O_j O_k) - \operatorname{Tr}(O_j O_l O_k) && (4.47)\\
&= \operatorname{Tr}([O_l, O_j] O_k) && (4.48)\\
&= \operatorname{Tr}\big(\gamma^m_{lj} O_m O_k\big) && (4.49)\\
&= \gamma^m_{lj}(-\delta_{mk}) && (4.50)\\
&= -\gamma^k_{lj}. && (4.51)
\end{aligned}$$

Thus as $\gamma^l_{jk} = -\gamma^l_{kj}$ and $\gamma^l_{jk} = \gamma^k_{lj}$, immediately it follows that the structure constants are indeed totally antisymmetric in all three indices.

From this the matrices K_j may be defined such that

$$[K_j]_{kl} = -\gamma^l_{jk} \tag{4.52}$$

where the matrix elements γ^l_{jk} are also the totally antisymmetric structure constants of the orthonormal set of matrices O_j.

4.4.5 Ensuring a Lie algebra isomorphism

In order for the mapping to be invertible, the adjoint representation of $\mathcal{L}$ is required to be a faithful representation. This will fail if there exists a non-trivial centre [97]. The centre is defined as a subalgebra $\mathcal{C}$ in $\mathcal{L}$ such that

$$\forall O_j \in \mathcal{L} \text{ and } \forall C \in \mathcal{C} \tag{4.53}$$

we have

$$[O_j, C] = 0. \tag{4.54}$$

We need only consider the case where there exists a one-dimensional centre. This is due to the fact that a two dimensional centre

$$C = \lambda O_1 + \mu O_2, \quad \lambda, \mu \notin \mathbb{R} \tag{4.55}$$

would imply

$$\begin{aligned} [O_1, C] &= 0 \\ &= [O_1, \lambda O_1 + \mu O_2] \\ &= \mu [O_1, O_2] \end{aligned} \tag{4.56}$$

Thus a two-dimensional centre would imply that O_1 and O_2 commute which is assumed

not to be the case as this would imply that the control problem was trivial.

In order to find a faithful $|\mathcal{L}|$-dimensional Lie algebra which is isomorphic to $\mathcal{L}$ we require a set of $|\mathcal{L}|$ linearly independent matrices that have the same structure constants as $\mathcal{L}$. Choosing a set

$$\{O_1, \ldots, O_{|\mathcal{L}|-1}, O_{|\mathcal{L}|} = C\} \tag{4.57}$$

where C is in the centre and all elements are orthogonalised with respect to the inner product defined in Eq. (4.38), then defining

$$K_j = T_j \oplus 0, \quad j < |\mathcal{L}| \tag{4.58}$$

and

$$K_{|\mathcal{L}|} = 0 \oplus ia\mathbf{1}, \quad a \in \mathbb{R} \tag{4.59}$$

gives the required set. The factor of i in the identity guarantees anti-Hermiticity for all K_j. An alternative solution that guarantees reality of matrices K_j involves, rather than $K_{\mathcal{L}}$ being defined via a direct sum with $ia\mathbf{1}$, instead

$$K_{|\mathcal{L}|} = 0 \oplus \begin{pmatrix} 0 & a \\ -a & 0 \end{pmatrix} \tag{4.60}$$

where a is a real multiple of an identity matrix of any dimension. This will be useful in certain circumstances where it is desired that unitary dynamics are given by real matrices. As discussed later, this will be helpful in the concrete example of surface code detachment.

We therefore obtain two dynamical Lie algebras

$$\mathcal{L} = \text{span}\{O_1, ..., O_{\mathcal{L}}\} \tag{4.61}$$

$$\mathcal{M} = \text{span}\{K_1, ..., K_{\mathcal{L}}\} \tag{4.62}$$

whose representations preserve structure constants and thus are isomorphic.

4.4.6 Local isomorphism and mapping of dynamics

Isomorphism on the level of Lie algebras does not necessarily imply such an invertible mapping on the space of Lie groups, as evidenced by the famous two-to-one correspondence between $SU(2)$ and $SO(3)$ [98]. This is to say that, while there *is* an invertible mapping between the traceless anti-Hermitian matrices of $\mathfrak{su}(2)$ and the antisymmetric matrices of $\mathfrak{so}(3)$, at the Lie group level both the identity and the negative of the identity in $SU(2)$ would be mapped to the identity in $SO(3)$.

Nevertheless there is a *local* isomorphism around the identity element between Lie groups that have isomorphic Lie algebras and it is precisely this fact which is exploited within our method. Taking a target unitary in the large space U_T one can decompose it into a product of n unitaries

$$U_T = \prod_{j=1}^{n} U_j \tag{4.63}$$

such that each U_j is close to the identity matrix. Here and afterwards we always consider products of unitaries to consist of repeated *left* multiplication. This factorisation is straightforward to calculate when the dynamics are determined by a time-dependent Hamiltonian with a piecewise-constant control function

$$H(t) = H_1 + f_j(t)H_2. \tag{4.64}$$

Such a Hamiltonian is constant during a time-step δt_k

$$H(t_k) = H_1 + f_k H_2 \tag{4.65}$$

$$H(t_k + \delta t_k) = H_1 + f_{k+1} H_2 \tag{4.66}$$

where t_k is a point of discontinuity. Thus each unitary U_j can be chosen to be

$$U_j = \exp(-iH(t_j)\delta t_j). \tag{4.67}$$

When the timeslots are chosen to be small enough then the corresponding unitary U_j is certain to be close to the identity. There can therefore indeed be defined a local isomorphism Φ between unitaries in the large space $U_j \in e^{\mathcal{L}}$ and unitaries in the small space $u_j \in e^{\mathcal{M}}$ such that $\Phi(U_j) = u_j$. Hence an overall target unitary can be defined in the smaller space

$$u_T = \prod_j^n \Phi(U_j) = \prod_j^n u_j. \tag{4.68}$$

While not true in general for arbitrary products of successive unitaries U_j, it is possible for certain products

$$V_j = \prod_{j=k}^{l} U_j = \mathcal{T} \exp\left(-i \int_{t_k}^{t_l} H(t')dt'\right) \tag{4.69}$$

to *themselves* be close to the identity, even for a comparatively long timescale $t_l - t_k$. Such unitaries V_j will also have counterparts in the small space $v_j = \prod_j \Phi(V_j)$ and the target dynamics can be reformulated in terms of these

$$U_T = \prod_j^m V_j \tag{4.70}$$

where some V_j are equal to products of consecutive U_j while others may be identical to a single unitary U_j. In short, as there is no isomorphic mapping between U_T and u_T in general, what is required instead of a single optimisation for infidelity is m different optimisations for each of the v_j. Each V_j can be written as the exponential of some

element of the dynamical Lie algebra $\mathcal{L}$ so that

$$V_j = \exp\left(\sum_k \alpha_k O_k\right) \tag{4.71}$$

while

$$v_j = \exp\left(\sum_k \beta_k K_k\right) \tag{4.72}$$

where the coefficients α_k and β_k are approximately equal, with the approximation becoming better the closer the unitaries are to the identity.

4.4.7 Optimal control in a smaller dimensional space

When a target u_T in the smaller-dimensional Lie group is found using Eq. (4.68), optimisation may be carried out in the smaller picture of $e^{\mathcal{M}}$ for each of the unitaries v_j in its decomposition. This optimisation entails finding piecewise constant control pulses $\tilde{f}$ such that the infidelity

$$\mathcal{I}(v_j, \tilde{v}_j) = 1 - \frac{1}{d}\,\mathrm{Tr}\Big\{v_j^\dagger \tilde{v}_j\Big\} \tag{4.73}$$

is minimised, where $\tilde{v}_j = \tilde{v}_j(\tilde{f}_j)$. For a sufficiently low infidelity, this optimised unitary in $e^{\mathcal{M}}$ can define a corresponding unitary in $e^{\mathcal{L}}$ via the optimised pulse

$$\tilde{V}_j = \Phi^{-1}(\tilde{v}_j(\tilde{f}_j)). \tag{4.74}$$

Of course what is ultimately sought after is minimisation of the infidelity between unitaries in the large space. It is hoped that if $\mathcal{I}(v_j, \tilde{v}_j)$ is small then this implies that $\mathcal{I}(V_j, \tilde{V}_j)$ is also small. In Fig. 4.7 we see that this is indeed the case when this optimisation procedure is carried out with the concrete example of the surface code detachment operation. Plotted on the abscissa is the square of the Frobenius norm of the difference between two random unitaries u_1 and u_2, scaled by the dimension of the matrix k. This is compared on the

ordinate with the squared normed difference between U_1 and U_2, scaled by its dimension K. These specific unitaries are related by a local Lie group isomorphism such that $\Phi(U_j) = u_j$. For unitaries close to the identity this scaled norm of their difference is closely related to their infidelity [44].

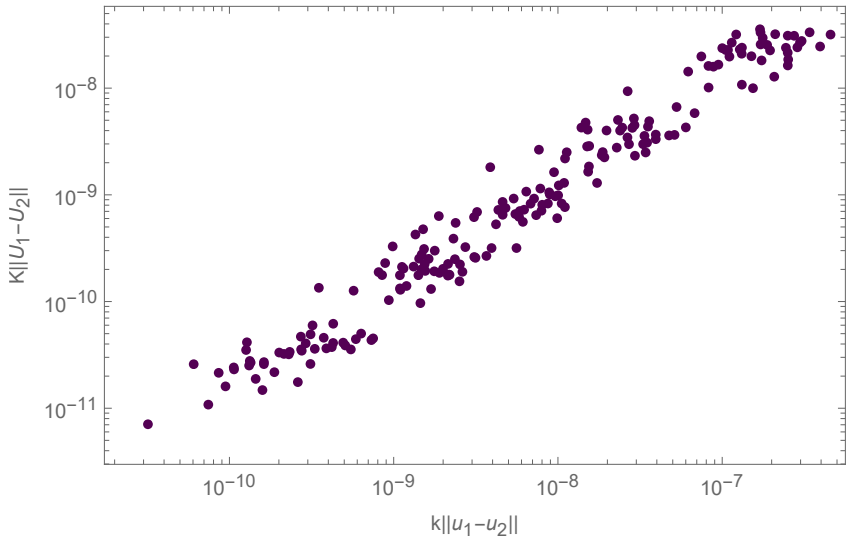

Figure 4.7: Comparison of normed differences between unitaries close to the identity in different Lie group spaces. On the abcissa are plotted $k\|u_1 - u_2\|_F^2$ for unitaries in the smaller space $\mathcal{M}$ while on the ordinate are plotted $K\|U_1 - U_2\|_F^2$ for unitaries in $e^{\mathcal{L}}$ so that $\Phi(U_j) = u_j$.

It remains to discuss the full infidelity overlap $\mathcal{I}(U_T, \tilde{U})$ where $\tilde{U} = \prod_j^m \tilde{V}_j$. This is generally computationally intensive to compute for large unitaries; however we show that this result can be related to the infidelities $\mathcal{I}(V_j, \tilde{V}_j)$.

The gate infidelity overlap between unitary matrices is related to the Frobenius norm via

$$\begin{aligned}\frac{1}{2d}\|U_1 - U_2\|_F^2 &= \frac{1}{2d}\operatorname{Tr}\big((U_1 - U_2)^\dagger(U_1 - U_2)\big) \\ &= \frac{1}{2d}\operatorname{Tr}\Big(2\mathbf{1} - 2\operatorname{Re}\Big\{\operatorname{Tr}\Big(U_1^\dagger U_2\Big)\Big\}\Big) \\ &= 1 - \frac{1}{d}\operatorname{Re}\Big\{\operatorname{Tr}\Big(U_1^\dagger U_2\Big)\Big\} \end{aligned} \tag{4.75}$$

where d is the dimension of the unitaries U_j. This scaled and squared normed difference is identically equal to the trace overlap infidelity $\mathcal{I}(U_1, U_2)$ for real unitary matrices and is a very good approximation for the infidelity when unitaries are close to the identity.

It can also be shown that, through repeated use of the triangle inequality,

$$\|\prod_j^n U_j - \prod_j^n \tilde{U}_j\| \leq \sum_j^n \|U_j - \tilde{U}_j\|. \tag{4.76}$$

This can be proven by taking the following

$$\begin{aligned} \|U_1U_2 - \tilde{U}_1\tilde{U}_2\| =& \|U_1U_2 - \tilde{U}_1U_2 + \tilde{U}_1U_2 - \tilde{U}_1\tilde{U}_2\| && (4.77)\\ \leq& \|U_1U_2 - \tilde{U}_1U_2\| + \|\tilde{U}_1U_2 - \tilde{U}_1\tilde{U}_2\| && (4.78)\\ =& \|U_1 - \tilde{U}_1\| + \|U_2 - \tilde{U}_2\| && (4.79) \end{aligned}$$

where we have used that $\|UM\| = \|M\|$ for any unitary matrix U and arbitrary matrix M. Inductively this can be generalised to the inequality bound (4.76).

The combination of these two relations (4.75) and (4.76) enables finding a bound for the infidelity between the full target unitary $U_T = \prod_j^n U_j = \prod_j^m V_j$ and the product of the chopped optimised unitaries $\prod_j^m \tilde{V}_j$.

4.5 Results of optimisation for the detachment operation

We formulate the surface detachment operation as a control problem and so we have Hamiltonians H_1 defined as H_i and $H_2 = H_f - H_i$, where the final and initial Hamiltonian are defined in equations (4.11) and (4.12) and are of dimension 2^{12}-by-2^{12}. Anti-Hermitian counterparts $A_1 = iH_1$ and $A_2 = iH_2$ are respectively defined.

A target unitary is defined in the large space by the dynamics of $H(t) = H_1 + f_{\text{ad}}(t)H_2$ from $t = 0$ to $t = T$ where f_{ad} is a piecewise constant function that goes from 0 to 1 in time $T = 1000$ and in n time steps. The timescale is chosen so that $T \gg \Delta^{-1}$ where Δ is the spectral gap. Thus the target unitary U_T effects adiabatic dynamics.

The dynamical Lie algebra $\mathcal{L}$ is defined via nested commutators of A_1 and A_2. In this example there is a basis of dimension 10, the last element of which is gained from a

commutator of depth 6. We now describe explicitly how this basis was found.

4.5.1 Generation of the dynamical Lie algebra

There are numerous different ways to generate a dynamical Lie algebra from an initial set of generators [15, 99]. A standard method involves repeatedly taking Lie brackets (here commutators) of a linearly independent set of generators until no further linearly independent matrices are found. The algorithm must take at most N^2 steps for matrix generators of dimension N-by-N.

This allows us to define the dynamical Lie algebra for the surface code detachment operation, as generated by $A_1 = iH_i$ and $A_2 = i(H_f - H_i)$ as defined by equations (4.11) and (4.12) respectively

$$A_3 = [A_1, A_2] \tag{4.80}$$

$$A_4 = [A_2, [A_1, A_2]] \tag{4.81}$$

$$A_5 = [A_2, [A_2, [A_1, A_2]]] \tag{4.82}$$

$$A_6 = [A_1, [A_2, [A_2, [A_1, A_2]]]] \tag{4.83}$$

$$A_7 = [A_2, [A_2, [A_2, [A_1, A_2]]]] \tag{4.84}$$

$$A_8 = [A_2, [A_2, [A_2, [A_2, [A_1, A_2]]]]] \tag{4.85}$$

$$A_9 = [A_1, [A_2, [A_2, [A_2, [A_2, [A_1, A_2]]]]]] \tag{4.86}$$

$$A_{10} = [A_2, [A_2, [A_2, [A_2, [A_2, [A_1, A_2]]]]]]. \tag{4.87}$$

When this dynamical Lie algebra is orthogonalised with respect to the negative real Hilbert-Schmidt inner product, this gives another Lie algebra whose structure constants are totally antisymmetric in all three indices. The basis elements O_j of this Lie algebra are given explicitly by the relation

$$\mathbf{O}_j = M\mathbf{A}_j \tag{4.88}$$

where M is the matrix

$$\begin{pmatrix}
-\frac{841}{18432\sqrt{11}} & -\frac{841}{18432\sqrt{11}} & 0 & \frac{841}{18432\sqrt{11}} & 0 & \frac{29}{9216\sqrt{11}} & \frac{29}{9216\sqrt{11}} & 0 & \frac{1}{18432\sqrt{11}} & \frac{1}{18432\sqrt{11}} \\
\frac{1}{32\sqrt{6}} & \frac{1}{32\sqrt{6}} & 0 & 0 & 0 & 0 & 0 & 0 & 0 & 0 \\
0 & 0 & \frac{1}{32\sqrt{6}} & 0 & 0 & 0 & 0 & 0 & 0 & 0 \\
\frac{577}{3072\sqrt{330}} & \frac{577}{3072\sqrt{330}} & 0 & -\frac{577}{3072\sqrt{330}} & 0 & -\frac{29}{1536\sqrt{330}} & -\frac{29}{1536\sqrt{330}} & 0 & -\frac{1}{3072\sqrt{330}} & -\frac{1}{3072\sqrt{330}} \\
0 & 0 & \frac{17}{384\sqrt{5}} & 0 & \frac{1}{384\sqrt{5}} & 0 & 0 & 0 & 0 & 0 \\
-\frac{17}{384\sqrt{5}} & -\frac{17}{384\sqrt{5}} & 0 & 0 & 0 & \frac{1}{384\sqrt{5}} & 0 & 0 & 0 & 0 \\
\frac{61}{3072\sqrt{6}} & \frac{61}{3072\sqrt{6}} & 0 & -\frac{61}{3072\sqrt{6}} & 0 & -\frac{7}{2560\sqrt{6}} & -\frac{7}{2560\sqrt{6}} & 0 & -\frac{1}{15360\sqrt{6}} & -\frac{1}{15360\sqrt{6}} \\
0 & 0 & \frac{61}{768\sqrt{6}} & 0 & \frac{7}{640\sqrt{6}} & 0 & 0 & \frac{1}{3840\sqrt{6}} & 0 & 0 \\
-\frac{61}{768\sqrt{6}} & -\frac{61}{768\sqrt{6}} & 0 & 0 & 0 & \frac{7}{640\sqrt{6}} & 0 & 0 & \frac{1}{3840\sqrt{6}} & 0 \\
-\frac{37\sqrt{85}}{18432} & -\frac{841}{18432\sqrt{85}} & 0 & \frac{841}{18432\sqrt{85}} & 0 & \frac{29}{9216\sqrt{85}} & \frac{29}{9216\sqrt{85}} & 0 & \frac{1}{18432\sqrt{85}} & \frac{1}{18432\sqrt{85}}
\end{pmatrix}. \tag{4.89}$$

As $|\mathcal{L}| = 10$ this means the adjoint representation will comprise of ten matrices of size 10-by-10 meaning that there is a homomorphism, a not necessarily invertible mapping preserving algebra, between the dynamical Lie algebra $\mathcal{L}$ and the adjoint representation which is of much smaller size.

As there exists a one dimensional centre

$$\mathcal{C} = \text{span}\{(3145, 841, 0, -841, 0, -58, -58, 0, -1, -1).\mathbf{A}\}, \tag{4.90}$$

where $\mathbf{A}$ is the vector of basis elements of $\mathcal{L}$

$$\mathbf{A} = (A_1, \ldots, A_{10})^{\mathrm{T}}, \tag{4.91}$$

this means that for a faithful representation with a basis comprised of anti-Hermitian matrices we follow the procedure outlined in Section 4.4.5. This gives two isomorphic Lie algebra representations $\mathcal{L}$ and $\mathcal{M}$ with identical structure constants γ_{jk}^{l}, where the basis of $\mathcal{M}$ consists of ten 12-by-12 real anti-Hermitian matrices.

The only non-zero structure constants of these newly defined Lie algebras are shown

in Table 4.2 where there is antisymmetry in all permutations of the indices.

j	k	l	γ^l_{jk}	j	k	l	γ^l_{jk}
1	2	3	$\frac{1}{8\sqrt{11}}$	3	7	9	$\frac{1}{8\sqrt{6}}$
1	5	6	$\frac{1}{8\sqrt{11}}$	4	5	6	$\frac{7\sqrt{\frac{3}{110}}}{16}$
1	8	9	$\frac{1}{8\sqrt{11}}$	4	5	9	$-\frac{\sqrt{11}}{64}$
2	3	4	$\frac{\sqrt{\frac{5}{66}}}{8}$	4	6	8	$\frac{\sqrt{11}}{64}$
2	4	5	$\frac{\sqrt{11}}{64}$	4	8	9	$\frac{\sqrt{\frac{5}{66}}}{8}$
2	5	7	$\frac{\sqrt{5}}{64}$	5	6	7	$-\frac{\sqrt{\frac{3}{2}}}{16}$
2	7	8	$\frac{1}{8\sqrt{6}}$	5	7	9	$-\frac{\sqrt{5}}{64}$
3	4	6	$\frac{\sqrt{11}}{64}$	6	7	8	$\frac{\sqrt{5}}{64}$
3	6	7	$\frac{\sqrt{5}}{64}$				

Table 4.2: The non-vanishing structure constants γ^l_{jk} of the orthogonalised basis of the dynamical Lie algebra $\mathcal{L}$. This takes into account total antisymmetry in all three indices.

4.5.2 Numerical optimisation

For our specific example, the target unitary is decomposed into $n = 2 \times 10^5$ unitaries U_j. As stated previously, optimisation must be carried out on m different optimisations for each of the v_j. Each individual $v_j = v_j(t_j - t_{j-1})$ corresponds to a time evolution interval of $\tau = t_j - t_{j-1}$ and we find an optimised $\tilde{v}_j = \tilde{v}_j(\tilde{f}(t))$ such that $\mathcal{I}(v_j, \tilde{v}_j)$ is as small as possible and yet $\tilde{v}_j$ consists of a time evolution less than τ. In the operation described, only $k = 72 < m$ such unitaries $v_j = v_j(t_j - t_{j-1})$ were equal to a concatenation of multiple unitaries u_j such that the time-interval $(t_j - t_{j-1})$ is comparatively long. As a result, optimisation was only successfully carried out on each of v_1 to v_k. However as these unitaries represent a cumulative time evolution that comprises 98.716% of the total time evolution of the target unitary u_T, and as optimisation was successful in reducing the required timescale for achieving these target dynamics v_1 to v_k by two orders of magnitude, optimisation was successful overall.

In Fig. 4.8 is shown the infidelity between unitary $v(t, 0)$ and the identity (blue), as well as between the unitary $V(t, 0)$ and the identity, where $v(t, 0) = \Phi(V(t, 0))$. We see that when a unitary v_j is close to the identity in the small picture its counterpart V_j is

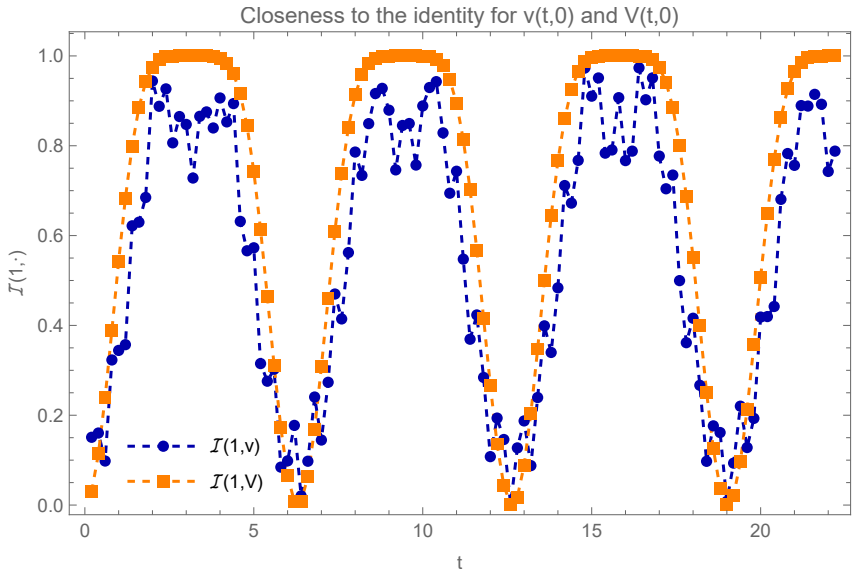

Figure 4.8: Closeness to the identity quantified and compared for unitaries in $e^{\mathcal{L}}$ and $e^{\mathcal{M}}$. The infidelity $\mathcal{I}(\mathbf{1}, v)$ is plotted for concatenated unitary $v(t, 0)$ (blue) as well as the infidelity for the corresponding unitary in the large picture $V(t, 0)$ ($\mathcal{I}(\mathbf{1}, V)$ shown in orange) for $t = 0$ to $t = 22$.

indeed close to the identity in the larger picture. The graph of $\|\mathbf{1} - V\|$ against $\|\mathbf{1} - v\|$ is qualitatively similar but with scale depending on the chosen norm. We see in Fig. 4.9 the results of the optimisation carried out for v_1 which is defined ultimately from concatenated unitaries corresponding to time $t = 0$ to $t = 19.1$. For this unitary, in the small space and large space respectively we have

$$\mathcal{I}(\mathbf{1}, v_1) = 0.00195988 \tag{4.92}$$

$$\mathcal{I}(\mathbf{1}, V_1) = 0.000649426 \tag{4.93}$$

meaning that unitaries in both spaces are indeed close to the identity and so they are well defined as counterparts due to the local isomorphism. Fig. 4.9 shows the infidelity between v_1 and the optimised $\tilde{v}_1$ and shows that we can get effectively perfect fidelities after a drop time of $t \approx 0.1$. Also shown is the repeat of this procedure with a differing number of time steps. Optimisation is marginally more successful in terms of achieving low infidelity at a shorter timescale when 200 time steps are used as compared with 100 time steps.

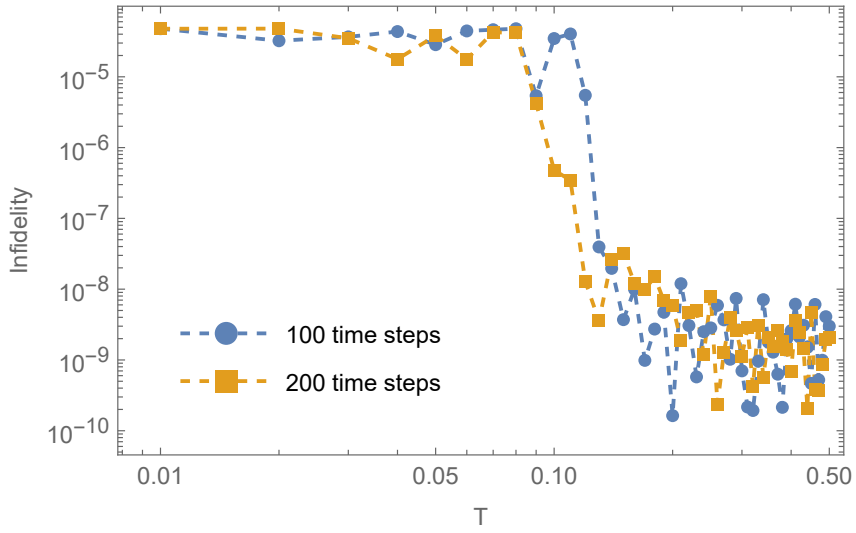

Figure 4.9: Optimised pulse durations for target unitary $v_1 = v(19.1 - 0)$. Increased number of time steps demonstrates an improvement in infidelity and a drop time at $t \approx 0.1$ showing an improvement of two orders of magnitude.

From the successfully optimised pulses we developed, we achieved high fidelities at timescales two orders of magnitude faster compared with the target dynamics, as indicated by Fig. 4.9 for a particular target v_1. It is also possible to optimise for quicker times at the cost of very large pulse amplitudes which are on the order of more than 3 orders of magnitude larger than the spectral gap.

It is computationally intensive to calculate infidelities between target unitaries V_j and optimised unitaries $\tilde{V}_j = \Phi^{-1}(v_j)$ in the larger picture. However, as seen in Fig. 4.7, there is a linear relationship between them that can be used to determine infidelities in the larger space. The relationship can be given approximately as

$$\|v_j - \tilde{v}_j\|_F \sim 10\|V_j - \tilde{V}_j\|_F. \tag{4.94}$$

Due to the fact that the Lie algebra representation that generates the unitaries v_j can be chosen to be real, the unitaries themselves must also be real and so a low infidelity $\mathcal{I}(v_j, \tilde{v}_j)$ can be related to a small normed difference by using Equation (4.75) so that

$$\|v_j - \tilde{v}_j\|_F = \sqrt{2d\mathcal{I}(v_j, \tilde{v}_j)}. \tag{4.95}$$

With this as well as relation (4.94) the normed difference between the larger unitaries $\|V_j - \tilde{V}_j\|_F$ can be approximated. The sum of the normed differences for all optimised unitaries V_j can then be summed to provide a bound, via the inequality (4.76), for the infidelity between the full target unitary in the larger space U_T and the product of all optimised unitaries . When calculated explicitly, the bound for the infidelity is given as

$$\mathcal{I}(U_T, \tilde{U}) = 1 - \frac{1}{d}\left|\mathrm{Tr}\left(U_T^\dagger \prod_j^m \tilde{V}_j\right)\right| \leq 5.184 \times 10^{-6}. \tag{4.96}$$

4.6 Conclusion

It has been shown that using quantum optimal control methods, one can replicate the results of using adiabatic dragging protocols within the surface code that allow for the encoding and processing of quantum information. Our methods have allowed for this to be achieved without resorting to the long timescales required by adiabaticity. Additionally we have seen how the use of dynamical Lie algebras and their representations allows us to use these quantum control techniques even for control problems which require control of many spins within a lattice system. This method can be useful for other control problems where we wish to control the entire dynamics and where the dimension of another representation of the dynamical Lie algebra is much smaller than the size of the matrices within the original representation. Additionally, we have shown that good infidelities for unitary gates in a smaller dimensional representation are suitably bounded by analogously good infidelities for unitaries in a larger dimensional representation, as long as there is an isomorphism on the level of Lie algebras. This indicates that overall optimisation is successful when favourable results are achieved in the smaller dimensional space, as they indeed were for our control problem.

Chapter 5

Conclusion

5.1 Summary and outlook

In this thesis we have demonstrated that quantum control can be successfully utilised to implement creation of anyons and defects in topological lattice models. This will allow for successful encoding of quantum information in a manner that preserves the protection afforded by quantum systems with topological order. Previous work has focused on using adiabatic dynamics when looking at time-dependence in Hamiltonians of systems with topological order in order to preserve any encoded logical quantum information, and not allow unwanted errors to be created which over time could become logical errors. We have seen that using quantum control is an effective method of implementing the desired anyonic states in a spin lattice without requiring long timescales and without causing more vulnerability to the system in terms of potential errors.

In Chapter 2, we have shown that in the toric code, a relatively simply defined system that nevertheless demonstrates topological order, abelian anyons may be created using time-dependent pulses which are bounded in both time and pulse amplitude. The protocol developed is shown to grow linearly in the length of the spin lattice ensuring scalability. The robustness in the face of small errors both in pulse implementation as well as due to intrinsic errors in the Hamiltonian has been demonstrated. We have shown the benefits that large spin lattices present in terms of offering better protection against logical errors

while acknowledging the effect to which the anyon creation and logical gate implementation protocols we developed are affected in their effectiveness in terms of the magnitude of errors that are tolerable. Use of quantum control can be considered for potential experimental implementations of the toric code that have been proposed [51, 80, 100].

In Chapter 3, we have presented a method for using quantum control for implementing non-abelian anyon creation in the form of vortices in the Kitaev honeycomb model. The method developed is scalable as it grows in difficulty of numerical implementation only linearly with the lattice size. Previous restrictions of the model where adiabatic dynamics are used were overcome by extending the known fermionisation of the static Kitaev honeycomb model and extending this to the time-dependent case.

In Chapter 4, we have shown that in the surface code, a system allowing for encoding of topologically protected qubits as well as for implementation of Clifford gates useful for quantum algorithms, quantum control can be used to implement the dynamics that hitherto had been demonstrated using adiabatic protocols that required long timescales. In the process, we developed a method of mapping a quantum system's unitary dynamics that could be useful for other control problems of a similar type where numerical optimisation of target fidelities are computationally intensive due to system size. Experimental work suggesting the use of surface codes as successful topological qubits are currently known [80, 81, 101, 102] and so the quantum control methods described are a potential aid to the implementation of encoding of quantum information in such systems in timescales that are comparatively short which is useful in the face of possible decoherence.

Given the results shown in the successful use of quantum control within three well-known topological quantum systems, there is scope for future progress to be made in this realm. As an example, the hitherto discussed systems which display non-abelian anyonic behaviour exhibit Ising anyon fusion rules which, while useful, are not complete for universal quantum computation. It has been suggested that fractional quantum Hall states display Fibonacci anyonic behaviour [21, 103, 104] and an investigation of using quantum control in these systems would be of interest.

Additionally, there is potential for future work on the interplay between quantum con-

trol and topological systems [105, 106], including measurement-based quantum control. It may be beneficial to look at incorporating measurement of spins in lattices more seamlessly with quantum control, as part of the overall process of implementing an algorithm in, for example, the surface code. There are thus many prospective avenues that are suitable for further investigation.

Bibliography

[1] Peter W. Shor. Polynomial-Time Algorithms for Prime Factorization and Discrete Logarithms on a Quantum Computer. *SIAM Journal on Computing*, 26(5):1484–1509, 10 1997.

[2] Lov K. Grover. A fast quantum mechanical algorithm for database search. In *Proceedings of the twenty-eighth annual ACM symposium on Theory of computing - STOC '96*, pages 212–219, New York, New York, USA, 1996. ACM Press.

[3] Lijun Ma, Xiao Tang, and Oliver Slattery. Optical quantum memory applications in quantum communication. In Keith S. Deacon, editor, *Quantum Communications and Quantum Imaging XVII*, page 1. SPIE, 9 2019.

[4] Tudor D. Stanescu. *Introduction to topological quantum matter and quantum computation*. CRC Press, 2016.

[5] G. J. Milburn. Photons as qubits. *Physica Scripta*, T137:014003, 12 2009.

[6] Roee Ozeri. The trapped-ion qubit tool box. *Contemporary Physics*, 52(6):531–550, 11 2011.

[7] Philipp-Immanuel Schneider and Alejandro Saenz. Quantum computation with ultracold atoms in a driven optical lattice. *Physical Review A*, 85(5):050304, 5 2012.

[8] F. H. L. Koppens, C. Buizert, K. J. Tielrooij, I. T. Vink, K. C. Nowack, T. Meunier, L. P. Kouwenhoven, and L. M. K. Vandersypen. Driven coherent oscillations of a single electron spin in a quantum dot. *Nature*, 442(7104):766–771, 8 2006.

[9] Morten Kjaergaard, Mollie E. Schwartz, Jochen Braumüller, Philip Krantz, Joel I.J. Wang, Simon Gustavsson, and William D. Oliver. Superconducting Qubits: Current State of Play. *Annual Review of Condensed Matter Physics*, 11:369–395, 3 2020.

[10] Jay M. Gambetta, Jerry M. Chow, and Matthias Steffen. Building logical qubits in a superconducting quantum computing system. *npj Quantum Information 2017 3:1*, 3(1):1–7, 1 2017.

[11] Tao Xin, Bi-Xue Wang, Ke-Ren Li, Xiang-Yu Kong, Shi-Jie Wei, Tao Wang, Dong Ruan, and Gui-Lu Long. Nuclear magnetic resonance for quantum computing: Techniques and recent achievements. *Chinese Physics B*, 27(2):020308, 2 2018.

[12] Jiannis K. Pachos. *Introduction to topological quantum computation*. Cambridge University Press, 2012.

[13] S. Das Sarma, Michael Freedman, and Chetan Nayak. Topological quantum computation. *Physics Today*, 59(7):32–38, 2006.

[14] Ville T. Lahtinen and Jiannis K. Pachos. A short introduction to topological quantum computation. *SciPost Physics*, 3(3):021, 9 2017.

[15] Domenico D'Alessandro. *Introduction to Quantum Control and Dynamics*. Routledge, second edition, 2008.

[16] Hideo Mabuchi and Navin Khaneja. Principles and applications of control in quantum systems. *International Journal of Robust and Nonlinear Control*, 15(15):647–667, 10 2005.

[17] Herschel Rabitz. Focus on Quantum Control. *New Journal of Physics*, 11(10):105030, 10 2009.

[18] D. Dong and I. R. Petersen. Quantum control theory and applications: A survey. *IET Control Theory and Applications*, 4(12):2651–2671, 12 2010.

[19] Binbin Chen, Jing Wang, and Yunsen Zhou. Quantum Control and Its Application: A Brief Introduction. *Journal of Physics: Conference Series*, 1802(2):022068, 3 2021.

[20] Frank Wilczek. Quantum mechanics of fractional-spin particles. *Physical Review Letters*, 49(14):957–959, 10 1982.

[21] Ady Stern. Anyons and the quantum Hall effect—A pedagogical review. *Annals of Physics*, 323(1):204–249, 1 2008.

[22] H. Bartolomei, M. Kumar, R. Bisognin, A. Marguerite, J. M. Berroir, E. Bocquillon, B. Plaçais, A. Cavanna, Q. Dong, U. Gennser, Y. Jin, and G. Fève. Fractional statistics in anyon collisions. *Science*, 368(6487):173–177, 4 2020.

[23] Chetan Nayak, Steven H. Simon, Ady Stern, Michael Freedman, and Sankar Das Sarma. Non-Abelian anyons and topological quantum computation. *Reviews of Modern Physics*, 80(3):1083–1159, 2008.

[24] Y. Aharonov and D. Bohm. Significance of Electromagnetic Potentials in the Quantum Theory. *Physical Review*, 115(3):485–491, 8 1959.

[25] D. H. Kobe. Berry phase, Aharonov-Bohm effect and topology. *Journal of Physics A: Mathematical and General*, 24(15):3551, 8 1991.

[26] E. C. Rowell. An Invitation to the Mathematics of Topological Quantum Computation. *Journal of Physics: Conference Series*, 698(1):012012, 3 2016.

[27] H. Bombin. Topological Order with a Twist: Ising Anyons from an Abelian Model. *Physical Review Letters*, 105(3):030403, 7 2010.

[28] Simon Trebst, Matthias Troyer, Zhenghan Wang, and Andreas W. W. Ludwig. A Short Introduction to Fibonacci Anyon Models. *Progress of Theoretical Physics Supplement*, 176:384–407, 6 2008.

[29] Sankar Das Sarma, Michael Freedman, and Chetan Nayak. Majorana zero modes and topological quantum computation. *npj Quantum Information 2015 1:1*, 1(1):1–13, 10 2015.

[30] Roman M. Lutchyn, Jay D. Sau, and S. Das Sarma. Majorana fermions and a topological phase transition in semiconductor-superconductor heterostructures. *Physical Review Letters*, 105(7):077001, 8 2010.

[31] Kebiao Xu, Tianyu Xie, Fazhan Shi, Zhen Yu Wang, Xiangkun Xu, Pengfei Wang, Ya Wang, Martin B. Plenio, and Jiangfeng Du. Breaking the quantum adiabatic speed limit by jumping along geodesics. *Science Advances*, 5(6), 2019.

[32] Emil Génetay Johansen and Tapio Simula. Fibonacci Anyons Versus Majorana Fermions: A Monte Carlo Approach to the Compilation of Braid Circuits in SU(2) k Anyon Models. *PRX Quantum*, 2(1):10334, 3 2021.

[33] Ahmet Tuna Bolukbasi and Jiri Vala. Rigorous calculations of non-Abelian statistics in the Kitaev honeycomb model. *New Journal of Physics*, 14(4):045007, 4 2012.

[34] J. J. Sakurai and Jim Napolitano. *Modern Quantum Mechanics*. Cambridge University Press, 9 2017.

[35] Navin Khaneja, Timo Reiss, Cindie Kehlet, Thomas Schulte-Herbrüggen, and Steffen J. Glaser. Optimal control of coupled spin dynamics: Design of NMR pulse sequences by gradient ascent algorithms. *Journal of Magnetic Resonance*, 172(2):296–305, 2 2005.

[36] Benjamin Rowland and Jonathan A. Jones. Implementing quantum logic gates with gradient ascent pulse engineering: principles and practicalities. *Philosophical Transactions of the Royal Society A: Mathematical, Physical and Engineering Sciences*, 370(1976):4636–4650, 10 2012.

[37] G. Dirr, U. Helmke, I. Kurniawan, and T. Schulte-Herbrüggen. Lie-semigroup structures for reachability and control of open quantum systems: kossakowski-lindblad

generators form lie wedge to markovian channels. *Reports on Mathematical Physics*, 64(1-2):93–121, 8 2009.

[38] Christian Arenz, Benjamin Russell, Daniel Burgarth, and Herschel Rabitz. The roles of drift and control field constraints upon quantum control speed limits. *New Journal of Physics*, 19(10):103015, 10 2017.

[39] Shuang He, Shi Lei Su, Dong Yang Wang, Wen Mei Sun, Cheng Hua Bai, Ai Dong Zhu, Hong Fu Wang, and Shou Zhang. Efficient shortcuts to adiabatic passage for three-dimensional entanglement generation via transitionless quantum driving. *Scientific Reports*, 6(1):1–11, 8 2016.

[40] Brian B. Zhou, Alexandre Baksic, Hugo Ribeiro, Christopher G. Yale, F. Joseph Heremans, Paul C. Jerger, Adrian Auer, Guido Burkard, Aashish A. Clerk, and David D. Awschalom. Accelerated quantum control using superadiabatic dynamics in a solid-state lambda system. *Nature Physics*, 13(4):330–334, 4 2017.

[41] W. Wang, S. C. Hou, and X. X. Yi. Adiabatic evolution under quantum control. *Annals of Physics*, 327(5):1293–1303, 5 2012.

[42] Selwyn Simsek and Florian Mintert. Quantum control with a multi-dimensional Gaussian quantum invariant. *Quantum*, 5:409, 3 2021.

[43] A. Yu. Kitaev. Anyons in an exactly solved model and beyond. *Annals of Physics*, 321(1):2–111, 2006.

[44] Omar Raii, Florian Mintert, and Daniel Burgarth. Scalable quantum control and non-Abelian anyon creation in the Kitaev honeycomb model. *Physical Review A*, 106(6):062401, 12 2022.

[45] A. Yu. Kitaev. Fault-tolerant quantum computation by anyons. *Annals of Physics*, 303(1):2–30, 1 2003.

[46] X. G. Wen and Q. Niu. Ground-state degeneracy of the fractional quantum Hall states in the presence of a random potential and on high-genus Riemann surfaces. *Physical Review B*, 41(13):9377–9396, 5 1990.

[47] Beat Röthlisberger, James R. Wootton, Robert M. Heath, Jiannis K. Pachos, and Daniel Loss. Incoherent dynamics in the toric code subject to disorder. *Physical Review A - Atomic, Molecular, and Optical Physics*, 85(2):022313, 2 2012.

[48] R. Alicki, M. Fannes, and M. Horodecki. On thermalization in Kitaev's 2D model. *Journal of Physics A: Mathematical and Theoretical*, 42(6):065303, 1 2009.

[49] Stefano Chesi, Beat Röthlisberger, and Daniel Loss. Self-correcting quantum memory in a thermal environment. *Physical Review A - Atomic, Molecular, and Optical Physics*, 82(2):022305, 8 2010.

[50] Adrian Hutter, James R. Wootton, Beat Röthlisberger, and Daniel Loss. Self-correcting quantum memory with a boundary. *Physical Review A - Atomic, Molecular, and Optical Physics*, 86(5):052340, 11 2012.

[51] Mahdi Sameti, Anton Potočnik, Dan E. Browne, Andreas Wallraff, and Michael J. Hartmann. Superconducting quantum simulator for topological order and the toric code. *Physical Review A*, 95(4):042330, 4 2017.

[52] R M Wilcox. Parameter Differentiation of Exponential Operators and the Baker-Campbell-Hausdorff Formula. *Journal of Mathematical Physics*, 8(4):2090, 1967.

[53] M. Hermanns, I. Kimchi, and J. Knolle. Physics of the Kitaev Model: Fractionalization, Dynamic Correlations, and Material Connections. *https://doi.org/10.1146/annurev-conmatphys-033117-053934*, 9:17–33, 3 2018.

[54] J. Knolle and R. Moessner. A Field Guide to Spin Liquids. *Annual Review of Condensed Matter Physics*, 10(1):451–472, 3 2019.

[55] Hidenori Takagi, Tomohiro Takayama, George Jackeli, Giniyat Khaliullin, and Stephen E. Nagler. Concept and realization of Kitaev quantum spin liquids. *Nature Reviews Physics 2019 1:4*, 1(4):264–280, 3 2019.

[56] Ville Lahtinen. Interacting non-Abelian anyons as Majorana fermions in the honeycomb lattice model. *New Journal of Physics*, 13(7):075009, 7 2011.

[57] Meng Cheng, Victor Galitski, and S. Das Sarma. Nonadiabatic effects in the braiding of non-Abelian anyons in topological superconductors. *Physical Review B*, 84(10):104529, 9 2011.

[58] David Aasen, Zhenghan Wang, and Matthew B. Hastings. Adiabatic paths of Hamiltonians, symmetries of topological order, and automorphism codes. *Physical Review B*, 106(8):085122, 8 2022.

[59] Hon Lam Lai and Wei Min Zhang. Decoherence dynamics of Majorana qubits under braiding operations. *Physical Review B*, 101(19):195428, 5 2020.

[60] Johannes Knolle. *Dynamics of a Quantum Spin Liquid*. Springer Theses. Springer International Publishing, Cham, 2016.

[61] Xiao Yong Feng, Guang Ming Zhang, and Tao Xiang. Topological characterization of quantum phase transitions in a spin-1/2 model. *Physical Review Letters*, 98(8):087204, 2 2007.

[62] G. Kells, J. K. Slingerland, and J. Vala. Description of Kitaev's honeycomb model with toric-code stabilizers. *Physical Review B - Condensed Matter and Materials Physics*, 80(12):125415, 9 2009.

[63] John Brennan and Jirí Vala. The Kitaev honeycomb model on surfaces of genus g greater than or equal to 2. *New Journal of Physics*, 20(5):053023, 5 2018.

[64] Elliott H. Lieb. Flux Phase of the Half-Filled Band. *Physical Review Letters*, 73(16):2158–2161, 10 1994.

[65] Jean-Paul Blaizot and Georges Ripka. *Quantum theory of finite systems*. MIT Press, Cambridge Mass., 1986.

[66] I. C. Fulga, M. Maksymenko, M. T. Rieder, N. H. Lindner, and E. Berg. Topology and localization of a periodically driven Kitaev model. *Physical Review B*, 99(23):235408, 6 2019.

[67] Paolo Molignini, Albert Gasull Celades, R. Chitra, and Wei Chen. Crossdimensional universality classes in static and periodically driven Kitaev models. *Physical Review B*, 103(18):184507, 5 2021.

[68] Albert Verdeny, Joaquim Puig, and Florian Mintert. Quasi-periodically driven quantum systems. *Zeitschrift fur Naturforschung - Section A Journal of Physical Sciences*, 71(10):897–907, 10 2016.

[69] Joji Nasu and Yukitoshi Motome. Nonequilibrium Majorana dynamics by quenching a magnetic field in Kitaev spin liquids. *Physical Review Research*, 1(3):033007, 10 2019.

[70] Giuliano Benenti and Giuliano Strini. Computing the distance between quantum channels: Usefulness of the Fano representation. *Journal of Physics B: Atomic, Molecular and Optical Physics*, 43(21):215508, 11 2010.

[71] Gene H. Golub and Charles F. Van Loan. *Matrix computations*. The Johns Hopkins University Press, 3 edition, 1996.

[72] Michał Oszmaniec, Ninnat Dangniam, Mauro E.S. Morales, and Zoltán Zimborás. Fermion Sampling: A Robust Quantum Computational Advantage Scheme Using Fermionic Linear Optics and Magic Input States. *PRX Quantum*, 3(2):020328, 5 2022.

[73] Michał Oszmaniec, Adam Sawicki, and Michał Horodecki. Epsilon-Nets, Unitary Designs, and Random Quantum Circuits. *IEEE Transactions on Information Theory*, 68(2):989–1015, 2 2022.

[74] Nathaniel Johnston, David W. Kribs, and Vern I. Paulsen. Computing stabilized norms for quantum operations via the theory of completely bounded maps. *Quantum Information & Computation*, 1 2009.

[75] J. R. Johansson, P. D. Nation, and Franco Nori. QuTiP 2: A Python framework for the dynamics of open quantum systems. *Computer Physics Communications*, 184(4):1234–1240, 4 2013.

[76] Wim Van Dam, Michele Mosca, and Umesh Vazirani. How powerful is adiabatic quantum computation? *Annual Symposium on Foundations of Computer Science - Proceedings*, pages 279–287, 2001.

[77] Daniel Burgarth, Jeff Borggaard, and Zoltán Zimborás. Quantum distance to uncontrollability and quantum speed limits. *Physical Review A*, 105(4):042402, 4 2022.

[78] Sebastian Deffner and Steve Campbell. Quantum speed limits: from Heisenberg's uncertainty principle to optimal quantum control. *Journal of Physics A: Mathematical and Theoretical*, 50(45):453001, 10 2017.

[79] A. Micheli, G. K. Brennen, and P. Zoller. A toolbox for lattice-spin models with polar molecules. *Nature Physics 2006 2:5*, 2(5):341–347, 4 2006.

[80] Ruben Verresen, Mikhail D. Lukin, and Ashvin Vishwanath. Prediction of Toric Code Topological Order from Rydberg Blockade. *Physical Review X*, 11(3):031005, 9 2021.

[81] G. Semeghini, H. Levine, A. Keesling, S. Ebadi, T. T. Wang, D. Bluvstein, R. Verresen, H. Pichler, M. Kalinowski, R. Samajdar, A. Omran, S. Sachdev, A. Vishwanath, M. Greiner, V. Vuletić, and M. D. Lukin. Probing topological spin liquids on a programmable quantum simulator. *Science*, 374(6572):1242–1247, 12 2021.

[82] Chris Cesare, Andrew J. Landahl, Dave Bacon, Steven T. Flammia, and Alice Neels. Adiabatic topological quantum computing. *Physical Review A - Atomic, Molecular, and Optical Physics*, 92(1):012336, 7 2015.

[83] Benjamin J. Brown, Katharina Laubscher, Markus S. Kesselring, and James R. Wootton. Poking holes and cutting corners to achieve clifford gates with the surface code. *Physical Review X*, 7(2):021029, 5 2017.

[84] Daniel Gottesman. *Stabilizer Codes and Quantum Error Correction*. PhD thesis, California Institute of Technology, Pasadena, California, 5 1997.

[85] Dave Bacon and Steven T. Flammia. Adiabatic Gate Teleportation. *Physical Review Letters*, 103(12):120504, 9 2009.

[86] Dave Bacon and Steven T. Flammia. Adiabatic cluster-state quantum computing. *Physical Review A*, 82(3):030303, 9 2010.

[87] C. G. Broyden. The Convergence of a Class of Double-rank Minimization Algorithms 1. General Considerations. *IMA Journal of Applied Mathematics*, 6(1):76–90, 3 1970.

[88] Roger Fletcher. A new approach to variable metric algorithms. *The Computer Journal*, 13(3):317–322, 1 1970.

[89] Donald Goldfarb. A family of variable-metric methods derived by variational means. *Mathematics of Computation*, 24(109):23–26, 1970.

[90] D. F. Shanno. Conditioning of quasi-Newton methods for function minimization. *Mathematics of Computation*, 24(111):647–656, 1970.

[91] Dong C. Liu and Jorge Nocedal. On the limited memory BFGS method for large scale optimization. *Mathematical Programming 1989 45:1*, 45(1):503–528, 8 1989.

[92] J. E. Avron, R. Seiler, and L. G. Yaffe. Adiabatic theorems and applications to the quantum hall effect. *Communications in Mathematical Physics*, 110(1):33–49, 3 1987.

[93] A Barut and R Raczka. Quantum Dynamical Applications of Lie Algebra Representations. *Theory of Group Representations and Applications*, pages 378–391, 11 1986.

[94] Christianne Quesne. Symmetry and Dynamical Lie Algebras in Classical and Quantum Mechanics. *Symmetries in Physics*, pages 325–348, 1992.

[95] Jeremy Butterfield. On Symplectic Reduction in Classical Mechanics. *Philosophy of Physics*, pages 1–131, 1 2007.

[96] Zhong Qi Ma. Group theory for physicists. *Group Theory for Physicists*, pages 1–491, 1 2007.

[97] Howard Georgi. Lie Algebras In Particle Physics : from Isospin To Unified Theories. *Lie Algebras in Particle Physics*, 5 2018.

[98] Yvette Kosmann-Schwarzbach. *Groups and Symmetries*. Springer New York, 2010.

[99] David Elliott. *Bilinear Control Systems*. Springer Dordrecht, 2009.

[100] K. J. Satzinger, Y. J. Liu, A. Smith, C. Knapp, M. Newman, C. Jones, Z. Chen, C. Quintana, X. Mi, A. Dunsworth, C. Gidney, I. Aleiner, F. Arute, K. Arya, J. Atalaya, R. Babbush, J. C. Bardin, R. Barends, J. Basso, A. Bengtsson, A. Bilmes, M. Broughton, B. B. Buckley, D. A. Buell, B. Burkett, N. Bushnell, B. Chiaro, R. Collins, W. Courtney, S. Demura, A. R. Derk, D. Eppens, C. Erickson, L. Faoro, E. Farhi, A. G. Fowler, B. Foxen, M. Giustina, A. Greene, J. A. Gross, M. P. Harrigan, S. D. Harrington, J. Hilton, S. Hong, T. Huang, W. J. Huggins, L. B. Ioffe, S. V. Isakov, E. Jeffrey, Z. Jiang, D. Kafri, K. Kechedzhi, T. Khattar, S. Kim, P. V. Klimov, A. N. Korotkov, F. Kostritsa, D. Landhuis, P. Laptev, A. Locharla, E. Lucero, O. Martin, J. R. McClean, M. McEwen, K. C. Miao, M. Mohseni, S. Montazeri, W. Mruczkiewicz, J. Mutus, O. Naaman, M. Neeley, C. Neill, M. Y. Niu, T. E. O'Brien, A. Opremcak, B. Pató, A. Petukhov, N. C. Rubin, D. Sank, V. Shvarts, D. Strain, M. Szalay, B. Villalonga, T. C. White, Z. Yao, P. Yeh, J. Yoo, A. Zalcman, H. Neven, S. Boixo, A. Megrant, Y. Chen, J. Kelly, V. Smelyanskiy, A. Kitaev, M. Knap, F. Pollmann, and P. Roushan. Realizing topologically ordered states on a quantum processor. *Science*, 374(6572):1237–1241, 12 2021.

[101] Shibo Xu, Zheng-Zhi Sun, Ke Wang, Liang Xiang, Zehang Bao, Zitian Zhu, Fanhao Shen, Zixuan Song, Pengfei Zhang, Wenhui Ren, Xu Zhang, Hang Dong, Jinfeng Deng, Jiachen Chen, Yaozu Wu, Ziqi Tan, Yu Gao, Feitong Jin, Xuhao Zhu, Chuanyu Zhang, Ning Wang, Yiren Zou, Jiarun Zhong, Aosai Zhang, Weikang Li, Wenjie Jiang, Li-Wei Yu, Yunyan Yao, Zhen Wang, Hekang Li, Qiujiang Guo, Chao Song, H. Wang, and Dong-Ling Deng. Digital simulation of non-Abelian anyons with 68 programmable superconducting qubits. *arXiv preprint arXiv:2211.09802*, 11 2022.

[102] Youwei Zhao, Yangsen Ye, He Liang Huang, Yiming Zhang, Dachao Wu, Huijie Guan, Qingling Zhu, Zuolin Wei, Tan He, Sirui Cao, Fusheng Chen, Tung Hsun Chung, Hui Deng, Daojin Fan, Ming Gong, Cheng Guo, Shaojun Guo, Lianchen Han, Na Li, Shaowei Li, Yuan Li, Futian Liang, Jin Lin, Haoran Qian, Hao Rong, Hong Su, Lihua Sun, Shiyu Wang, Yulin Wu, Yu Xu, Chong Ying, Jiale Yu, Chen Zha, Kaili Zhang, Yong Heng Huo, Chao Yang Lu, Cheng Zhi Peng, Xiaobo Zhu, and Jian Wei Pan. Realization of an Error-Correcting Surface Code with Superconducting Qubits. *Physical Review Letters*, 129(3):030501, 7 2022.

[103] Abolhassan Vaezi and Maissam Barkeshli. Fibonacci anyons from Abelian bilayer quantum hall states. *Physical Review Letters*, 113(23):236804, 12 2014.

[104] Roger S.K. Mong, Michael P. Zaletel, Frank Pollmann, and Zlatko Papić. Fibonacci anyons and charge density order in the 12/5 and 13/5 quantum Hall plateaus. *Physical Review B*, 95(11):115136, 3 2017.

[105] Yunzhao Wang, Kyrylo Snizhko, Alessandro Romito, Yuval Gefen, and Kater Murch. Observing a topological transition in weak-measurement-induced geometric phases. *Physical Review Research*, 4(2):023179, 6 2022.

[106] Maryam Abbasi, Weijian Chen, Mahdi Naghiloo, Yogesh N. Joglekar, and Kater W. Murch. Topological Quantum State Control through Exceptional-Point Proximity. *Physical Review Letters*, 128(16):160401, 4 2022.

[107] Michael A. Nielsen and Isaac L. Chuang. *Quantum Computation and Quantum Information*. Cambridge University Press, 6 2012.

[108] Jing Liu, Xiao Ming Lu, Jian Ma, and Xiao Guang Wang. Fidelity and fidelity susceptibility based on Hilbert-Schmidt inner product. *Science China Physics, Mechanics and Astronomy 2012 55:9*, 55(9):1529–1534, 7 2012.

[109] Stephen Boyd and Lieven Vandenberghe. *Convex Optimization*. Cambridge University Press, 3 2004.

[110] Xin-She Yang. Optimization algorithms. *Introduction to Algorithms for Data Mining and Machine Learning*, pages 45–65, 1 2019.

[111] Philip E. Gill, Walter Murray, and Margaret H. Wright. *Practical Optimization*. Academic Press, 1981.

[112] Patrick Rebentrost, Maria Schuld, Leonard Wossnig, Francesco Petruccione, and Seth Lloyd. Quantum gradient descent and Newton's method for constrained polynomial optimization. *New Journal of Physics*, 21(7):073023, 7 2019.

[113] J.E. Dennis Jr. and Jorge J. Moré. Quasi-Newton Methods, Motivation and Theory. *SIAM Review*, 19(1):46–89, 7 2006.

[114] Jorge Nocedal and Stephen J. Wright. Springer Series in Operations Research and Financial Engineering. In *Numerical Optimization*, chapter Quasi-Newton Methods, pages 135–163. Springer Nature, 2 edition, 2006.

[115] Philipp Hennig and Martin Kiefel. Quasi-Newton Methods: A New Direction Martin Kiefel. *Journal of Machine Learning Research*, 14:843–865, 2013.

Appendix A

Gradient ascent pulse engineering

In this appendix we describe in detail the mechanism behind the gradient ascent pulse engineering (GRAPE) algorithm [35, 36] which has been used to find non-linear control pulses that implement desired dynamics in Chapters 3 and 4. We have implemented this algorithm in our work using the QuTiP package [75] which allows for exact calculation of gradients. In our description as with elsewhere in our work we use natural units such that $\hbar = 1$.

A.1 Quantification of target dynamics

We are typically interested in the dynamics of a finite-dimensional quantum system which has some fixed dynamical generator known as the drift Hamiltonian H_d as well as one or more controllable interactions which can be considered to be control Hamiltonians $H_{c,j}$ where $j = 1, \ldots, n$. Each control Hamiltonian is associated with a real-valued time-dependent function $f_j(t)$. For our implementation of this algorithm we will only consider piecewise constant functions, therefore for a system with a total time-dependent Hamiltonian

$$H(t) = H_d + \sum_{j=1}^{n} f_{j,k}(t) H_{c,j}. \tag{A.1}$$

time is discretised into m time slots Δt_k. The solution of the dynamics is therefore

$$|\psi(t + \Delta t_k)\rangle = \exp(-iH(t_k)\Delta t_k)\,|\psi(t)\rangle \tag{A.2}$$

where t_k is the time at a point of discontinuity. In terms of the unitary time-evolution operator the dynamics are given by

$$U_k = \exp(-iH(t_k)\Delta t_k). \tag{A.3}$$

Thus the full dynamics from $t = 0$ to $t = T$, given chosen drift and control Hamiltonians, is given by the time ordered product of all the unitary operators corresponding to each piecewise constant time-interval

$$U(T, 0)[f_{1,1}, \ldots, f_{n,m}] = U_m ... U_1 U_0 \tag{A.4}$$

with the initial condition $U(0) = \mathbf{1}$.

Optimisation is concerned with implementing dynamics that resemble a chosen target dynamics U_{target} as closely as possible. To quantify this requires defining a figure of merit. In the case of state transfer, this is typically the state fidelity between an initial state $|\psi_0\rangle$ and a target state

$$\mathcal{F} = |\langle\psi_{\text{target}}|\psi_0\rangle|^2 \tag{A.5}$$

or, when seeking to minimise rather than maximise, the infidelity $\mathcal{I} = 1 - \mathcal{F}$ which commonly serves as a cost function. A similarly useful figure of merit when wishing to optimise total dynamics, irrespective of particular initial and target states, is the absolute value of the Hilbert-Schmidt inner product [107, 108]

$$\mathcal{F} = \frac{1}{d}\left|\mathrm{Tr}\left(U_{\text{target}}^{\dagger} U\right)\right| \tag{A.6}$$

as well as its correspondingly defined infidelity. The inner product must be scaled by the dimension d of the unitary operators. Both figures of merit are insensitive to global phases and are maximal at a value of 1 when the desired dynamics have been perfectly achieved. Quantum optimal control effectively amounts to optimising this fidelity given certain constraints such as pulse amplitudes, timescale of evolution and number of time steps.

A.2 Implementation of the GRAPE algorithm

In general, numerical optimisation in quantum control is concerned with minimising the infidelity by calculating gradients of the figure of merit and travelling down (descent) in the parameter space. As in many forms of numerical optimisation, it is very common for algorithms to lead to convergence around local minima. In order to avoid this, step sizes, that is, the distance one travels in parameter space, must be chosen to be small. This however comes at the cost of requiring further iterations of the algorithm and therefore more computational resources.

A.2.1 Limited-memory BFGS algorithm

Within each iteration step of the GRAPE algorithm, the exact direction that is chosen for descent in the parameter space is determined by the specified method of descent. Common methods that are chosen are steepest descent [109, 110], which involves numerically calculating the gradient of the figure of merit and descending in the opposite direction when minimising, and Newton-based methods [111, 112] that require calculation of second derivatives in the form of the Hessian matrix.

In essence, Newton-based methods use a parabolic approximation of the curvature of the cost function to choose the direction of descent. For a vector of parameters $\mathbf{v}$ which may include, for example, control amplitudes $f_{j,k}$ and time steps Δt_k, together with an infidelity $\mathcal{I}(\mathbf{v})$ that serves as a cost function to minimise, each successive step is calculated by

$$\mathbf{v}_{n+1} = \mathbf{v}_n - h_{\mathcal{I}}^{-1}(\mathbf{v}_n) \cdot \nabla\mathcal{I}(\mathbf{v}_n) \tag{A.7}$$

where $\nabla\mathcal{I}$ is the gradient of infidelity and $h_{\mathcal{I}}$ is the Hessian matrix of second derivatives of the infidelity.

Quasi-Newton methods [113, 114, 115] are however generally preferred for computationally demanding problems as, in such algorithms, rather than the full Hessian being calculated at each iteration, an approximation of it is made based on previous steps in the algorithm. Starting with an initial guess for this approximation b_n (typically this is the identity), a step $\Delta\mathbf{v}_n$ is calculated

$$\Delta(\mathbf{v}_n) = -b_n^{-1} \cdot \nabla\mathcal{I}(\mathbf{v}_n). \tag{A.8}$$

The next iteration of parameters is then calculated from this

$$\mathbf{v}_{n+1} = \mathbf{v}_n + \Delta\mathbf{v}_n \tag{A.9}$$

which allows for an updated Hessian approximation to be calculated. This is chosen so as to satisfy the so-called secant equation

$$\nabla\mathcal{I}(\mathbf{v}_{n+1}) - \nabla\mathcal{I}(\mathbf{v}_n) = b_{n+1}(\mathbf{v}_{n+1} - \mathbf{v}_n) \tag{A.10}$$

$$= b_{n+1}\Delta\mathbf{v}_n \tag{A.11}$$

and is generally close to the previous Hessian approximation with respect to some matrix norm.

The limited memory version of the BFGS algorithm (L-BFGS) [87, 88, 89, 90, 91] is a quasi-Newton method favoured for our work as it does not compute or store an entire matrix that approximates the Hessian but rather uses vectors such as the gradients and parameters of previous steps to reconstruct a Hessian approximation. In Fig. A.1 is shown an example of an implementation of the GRAPE algorithm after an initial guess is made for a control pulse.

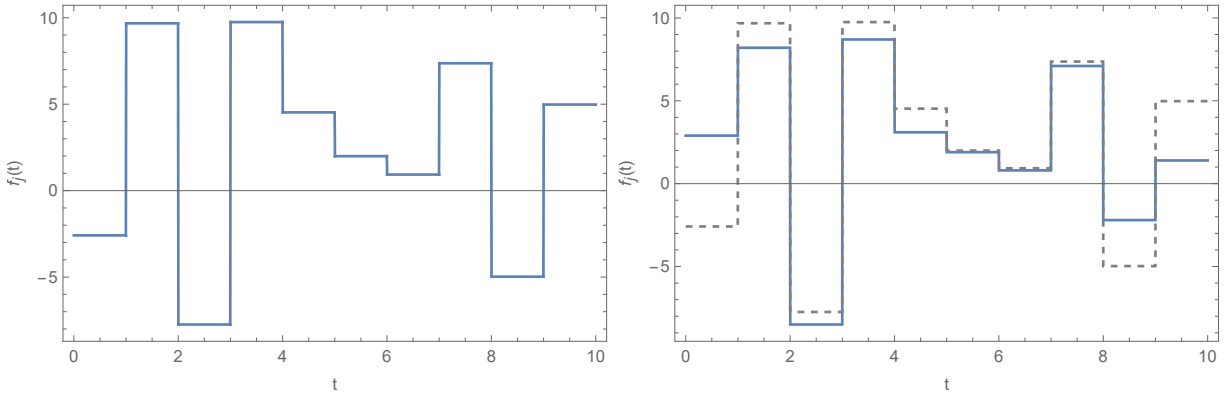

(a) Initial random guess pulse **(b)** Updated pulse after one iteration

Figure A.1: Example of GRAPE algorithm implementation for a short single control pulse $f_j(t)$. On the left is a random pulse used as an initial guess for the algorithm. After using one iteration of the algorithm the pulse is updated to the example on the right. The infidelity $\mathcal{I}$ tends towards a minimum of ideally 0 when this process is repeated. In this example the time slots are all equal and set to $\Delta t = 1$.